Series 01 Aerodynamics 08

Galloping Behaviour of an Aeroelastic Oscillator with Two Degrees of Freedom

B.W. van Oudheusden

Delft University Press

706 332

Galloping Behaviour of an Aeroelastic Oscillator with Two Degrees of Freedom

Bibliotheek TU Delft
C 3021860

2392
348
1

Series 01: Aerodynamics 08

Galloping Behaviour of an Aeroelastic Oscillator with Two Degrees of Freedom

B.W. van Oudheusden

BIBLIOTHEEK TECHNISCHE UNIVERSITEIT
Prometheusplein 1
2628 ZC
DELFT

Delft University Press / 1998

Published and distributed by:

Delft University Press
Mekelweg 4
2628 CD Delft
The Netherlands
Telephone +31 (0)15 278 32 54
Fax +31 (0)15 278 16 61
e-mail: DUP@DUP.TUDelft.NL

by order of:

Faculty of Aerospace Engineering
Delft University of Technology
Kluyverweg 1
P.O. Box 5058
2600 GB Delft
The Netherlands
Telephone +31 (0)15 278 14 55
Fax +31 (0)15 278 18 22
e-mail: Secretariaat@LR.TUDelft.NL
website: http://www.lr.tudelft.nl/

Cover: Aerospace Design Studio, 66.5 x 45.5 cm, by:
Fer Hakkaart, Dullenbakkersteeg 3, 2312 HP Leiden, The Netherlands
Tel. +31 (0)71 512 67 25

90-407-1571-8

Copyright © 1998 by Faculty of Aerospace Engineering

All rights reserved.
No part of the material protected by this copyright notice may be reproduced or utilized in any form or by any means, electronic or mechanical, including photocopying, recording or by any information storage and retrieval system, without written permission from the publisher: Delft University Press.

Printed in The Netherlands

Contents

List of notations

symbol	unit	quantity
b	m	model (cylinder) span
C	deg/s	frictional damping rate
D	s^{-1}	viscous damping rate
F_N	N	normal force
F_T	N	tangential force
f	Hz	frequency
g	m/s^2	gravitational acceleration: $g = 9.81$ m/s^2
h	m	characteristic dimension of the cylinder cross section (for the rectangular models used in the experiments the chord length is taken)
I	$kg.m^2$	moment of inertia
k	N.m	(torsional) spring stiffness
l	m	length
M_{fric}, M	N.m	frictional damping moment (components)
m	kg	mass
N	N.m.s	viscous damping component
q	Pa	dynamic pressure ($\frac{1}{2}\rho U^2$)
R	m	oscillator arm length
S	m^2	model reference area ($b \times h$)
t	s	time
U	m/s	flow velocity, wind speed
V_X, V_Y	m/s	model displacement velocity components
x	m	coordinate in streamwise direction
X	m	horizontal cylinder displacement
y	m	coordinate in normal direction
Y	m	vertical cylinder displacement
α	deg	angle of attack
θ	deg	oscillator angular displacement
ρ	kg/m^3	density
ω	rad/s	radial frequency: $\omega = 2\pi f$

coefficients and dimensionless numbers:

c	C/ω	frictional damping coefficient
c_N	F_N/qhb	normal force coefficient
c_T	F_T/qhb	tangential force coefficient
c_ζ	$2\zeta_{aer}/\mu u$	(sectional) aerodynamic damping coefficient
u	$U/\omega R$	reduced wind speed
μ	$\rho hbR^3/I$	mass parameter
ζ	D/ω	viscous damping coefficient

notation conventions:

$\dot{x}$	(dot)	denotes time derivative of a variable
$\hat{x}$	(hat)	denotes amplitude of a variable

Preface

This report presents the progress of research carried out at the Faculty LR within the framework of an interdepartmental project on aeroelastic oscillations. In the project, which is funded as a 'Commissie Beek' project, the Faculty of Aerospace Engineering (LR) and the Faculty of Mathematics and Informatics (TWI) participate. The TWI group addresses the formal mathematical analysis of the nonlinear differential equations that describe flow-induced vibration phenomena, on the basis of quasi-steady aerodynamic force modelling. The subject of the work at LR is the design and realisation of an experimental set-up, in order to acquire experimental data with which the modelling and theoretical analysis can be verified.

The preceding investigations have been directed towards the analysis of different types of one-degree-of-freedom (1-DOF) galloping, notably that of the rotational galloping behaviour of the type referred to as a 'see-saw oscillator'. In this configuration the model cylinder is rotated around a hinge axis that is parallel to the cylinder axis. As the distance between hinge axis and cylinder is large in comparison to the cross-sectional dimensions of the cylinder, the effect of cross sectional motion can be approximated by the instantaneous rotation angle and a linear displacement velocity, whereas the direct effect of the angular velocity can be neglected. This allows a quasi-steady modelling of the unsteady aerodynamic loads to be performed with much more confidence than in the case of 'pure rotation', where the hinge axis is close to the cylinder.

The theoretical analysis has been the specific subject of a number of previous reports [1-3], while details of the related experimental work, comprising the development of the experimental set-up and extensive measurements, have been reported in [4-5]. Several further publications have been devoted to the combined results [6-9].

In the present report the extension of the oscillator to a two-degrees-of-freedom (2-DOF) configuration is described.

Acknowledgements

With regard to the experimental work the contributions of H.J. Raaymakers, H. Keus and C.W.J. Lemmens in the design of the set-up and its instrumentation are gratefully acknowledged, as well as the assistance of the other members of the technical staff at the Low Speed Wind Tunnel Laboratory, where all experiments were carried out.

1. Introduction

1.1 Background

The object of the experimental part of the research project 'Aeroelastic Oscillations' is the design of an experimental set-up to study flow-induced oscillations in a wind tunnel. The experimental data of the set-up are used for a comparison with analytical models that describe aeroelastic phenomena, in particular galloping. Characteristic aspects are in this respect the nonlinear nature of the oscillations (a damping which is amplitude-dependent), which can give rise to the occurrence of limit-cycles (steady oscillations with finite amplitude).

Galloping can be characterised as being a low-frequency instability phenomenon of an aerodynamic nature. In practice it may occur on slender, lightly damped structures in cross flow, such as ice-covered transmission lines, high towers or bridge decks [10]. The cause of galloping lies in the occurrence of a negative aerodynamic damping: the aerodynamic forces generated by small relative motions of the structure act to amplify these motions, which results in a growing oscillation amplitude. Nonlinear effects provide a limiting effect, so that a stable oscillation with a finite, but often appreciable, amplitude may result.

1.2 The 1-DOF rotational galloping of the 'see-saw oscillator'

The case of one-degree-of-freedom (1-DOF) translational galloping under weakly nonlinear forcing conditions has been considered in detail by G.V. Parkinson [11,12], using a quasi-steady modelling of the aerodynamic forces. This approach entails that the aerodynamic forces at each instant during the oscillation of a structure can be taken equal to the forces that occur in an equivalent steady situation, where the same relative motion between structure and flow exists. This is assumed to be valid when the oscillation frequency is low with respect to the frequency that is characteristic of the flow, such as the vortex-shedding frequency. Static aerodynamic characteristics are derived from wind tunnel measurements on a stationary model.

In the case of *rotational* oscillations, both the angular displacement, which changes the angle of incidence, and the angular velocity are relevant. The dynamic effect of the latter is vital for the description of galloping (as this produces the aerodynamic damping term), but cannot be modelled realistically for pure rotations of the cross section. For the see-saw configuration, where the rotation arm is much larger than the diameter of the cross section, the rotation velocity effect can be approximated with that of a translation velocity [6]. In this way a configuration is obtained that can be regarded as an extension of Parkinson's translation model by adding a rotation that is coupled to the translation.

1.3 Basic characteristics of rotational galloping

Applying the quasi-steady modelling concept the effect of the aerodynamic forces can be interpreted as resulting in combined aerodynamic (nonlinear) damping and stiffness effects, where the latter can be neglected as long as the perturbation of the mechanical system by the aerodynamic forcing remains small (weak-forcing approach).

In the presence of a constant wind field the harmonic oscillatory motion of the cylinder induces a harmonic variation of the effective angle of attack (α) with respect to the oncoming wind. Previous analysis revealed that the aerodynamic damping, when properly scaled, is a function only of the amplitude of α, and applies to both rotational and purely translational motions alike. Hence, in absence of any system damping, limit cycle amplitudes vary with wind speed such as to maintain a constant value of the amplitude of α, and the different galloping behaviour of translating and rotating structures is only due to the different ways in which α is related to the oscillator motion. For translational motions α is equal to the ratio of the translation velocity and the wind speed, so at a constant oscillation frequency the galloping amplitude increases linearly with wind speed. For rotation the situation is more complex as α is determined by a combination of angular displacement and velocity. As a result, the oscillator displays a translational behaviour for small reduced wind speeds with amplitude increasing with wind speed, but possesses a pure torsional regime for large reduced wind speeds with the amplitude remaining essentially constant.

When considering galloping oscillations in the presence of viscous damping, it is possible, owing to the unique dependence of the damping on the amplitude of α, to obtain a normalisation of the galloping curve when considering the 'aerodynamic amplitude' (*i.e.* the amplitude of α) and scaling the wind speed with the damping level. This normalisation, which is similar to that reported earlier for translational galloping [11-12], indicates that the galloping behaviour is essentially similar for different amounts of damping, as e.g. bifurcations and the occurrence of multiple limit cycles with increasing wind speed are concerned [6,7]. This normalisation is affected when a more complex damping behaviour is considered, such as the combination of viscous and frictional damping displayed by the experimental set-up [5,9].

Galloping tests were performed for a large number of configurations, and the limit-cycle amplitudes were found mostly in good agreement with a quasi-steady assumption, in that when properly scaled the results fall on a single curve, which is in reasonable agreement with predictions. Significant deviations occurred for large amplitude oscillations at low values of u (smaller than 5), possibly indicating a violation of the quasi-steady assumption under these conditions due to modulation of the cylinder wake or other unsteady effects.

For increasingly large wind speeds the aerodynamic stiffness effect may become significant, as the aerodynamic forces remain no longer small with respect to elastic and

inertial forces. A strong-forcing approach was developed, where the system is described as a weakly perturbed Hamiltonian system, provided that the leading-order aerodynamic terms, which are of conservative nature, are included in the Hamiltonian [5,8]. Tests at high forcing levels confirmed the predicted behaviour of increased limit-cycle amplitudes and amplitude-dependent oscillation frequency, and in addition the phenomenon of dynamic divergence at sufficiently high wind speeds.

1.4 The 2-DOF oscillator configuration

In the present investigation the galloping behaviour is extended to a 2-DOF configuration in the study of what can be considered a 'double see-saw' oscillator. The construction is depicted schematically in Fig.1, while Fig.2 provides views of the actual set-up. The heavy lines in Fig.1 represent a structure similar to that investigated in the 1-DOF case, consisting of a pendulum-type oscillator with hinge point R_1. Instead of having the model (*i.e.* the cylinder upon which the wind forces are acting) rigidly attached to the structure, it forms part of a second 'see-saw' that is hinged in point R_2. Counter weight C_2 is used to balance the model weight w.r.t. R_2, whereas counter weight C_1 balances the weight of the complete second see-saw w.r.t. R_1. The structure is described by the two degrees of freedom θ_1 and θ_2, which are the angular displacements of the 'main' and 'model' see-saws, respectively (see also Fig.3). Pendulum-type restoring forces are provided by weights P_1 and P_2. Note that both pendulums hinge (independently) at R_1, while the second pendulum is connected to the model see-saw by means of a push-rod, instead of being directly attached to it. This construction has the large practical advantage that the two rotation angles can now be measured at the stationary point R_1, instead of having to measure θ_2 at the moving point R_2. In addition, the pendulum weight P_2 does not affect the balance of the main see-saw, allowing more freedom in the independent adjustment of the different oscillator properties.

The mode shape of the isolated degrees of freedom (*i.e.* when either θ_1 or θ_2 is zero) are depicted in Fig.1b. This shows that in 'mode 1' ($\theta_2 = 0$) the model see-saw remains horizontal, and the cylinder performs approximately a translational motion only. In 'mode 2' ($\theta_1 = 0$), on the other hand, the cylinder displays a rotational motion identical to that of the 1-DOF see-saw configuration considered in previous investigations. For this reason, modes 1 and 2 are called the 'translation mode' and the 'rotation mode' of the 2-DOF oscillator. As revealed by the oscillator equations of motion for this configuration in the next chapter (linearised for small displacement angles), these two modes correspond exactly to the uncoupled natural modes of the oscillator. In addition, further use will be made of a third mode, *viz.* the rotational 1-DOF configuration which results when both modes are rigidly coupled, such that $\theta_1 \equiv \theta_2$. This 'coupled mode' will be referred to as 'mode 0'.

2. Construction and modelling of the 2-DOF oscillator

2.1 Construction of the oscillator

The actual construction of the 2-DOF oscillator structure is shown in Fig.2. The main see-saw structure is supported by a frame on knife-bearings, while the mode-2 pendulum hinges on the main oscillator frame by means of ball bearings. Also the other hinges (R_2 in Fig.1 and the hinges of the push rod) are equipped with ball bearings. The electromagnetic damper was installed as in the picture, but has not been used in the experiments.

Note that as mentioned in the previous section both motions are recorded at stationary positions, at either side of the main oscillator hinge axis. As angle encoder 1 the same instrument was used as in the previous investigation of the 1-DOF oscillator, which is a Heidehahn ROD426 opto-electric digital angle encoder with a 0.09^{o} resolution (1024 intervals, quadruple mode) [5]. As the ball bearings of the encoder axis had been found to introduce a notable amount of frictional damping in the system, it was decided to select a contactless version for the second encoder with which the motion of the much lighter second mode is recorded. It was found that the original choice of a Heidehahn 1024-interval type was unsuitable in the present construction, for its sensitivity to the exact positioning of the encoder housing with respect to the encoder shaft that is attached to the mode-2 construction. Instead, a readily available 500-interval Hewlett Packard encoder was used, which proved to be more tolerant to this positioning. Operated in the same quadruple mode, this encoder yields a resolution of 0.18^{o}. The timing of the data sampling was carried out using the BIOS-timer of the PC, which allows a sampling interval of (any integer multiple of) 3600/65536 sec = 55 ms, the BIOS clock period. For all dynamic measurements to be reported a single timer period was used, resulting in a sampling frequency of 18.2 Hz.

2.2 Experimental set-up and model configurations

To allow a larger range in the motions of the oscillator a test section with enlarged height was constructed, with a cross section of 0.6 m and 0.4 m (was: 0.4 m × 0.4 m). The length of the test section is 1.4 m, and the oscillator frame was placed at the exit of the test section as can be seen in Fig.2. To accommodate the larger test section height, a new contraction section was designed according to the method of Mikhail [13].

In Table 1 the major dimensions and mechanical properties are given for the different oscillator configurations that have been investigated. These configurations, involving different cylinder models and/or different values of the frequency ratio, are denoted as follows:

	frequency ratio f_2/f_1	model cross section
A	0.98	Rectangular cross section 40 mm × 25 mm (with short side facing the flow)
B	1.27	
C	1.01	Square cross section 30 mm × 30 mm

Configuration A and B both have the same cylinder model, but a different frequency ratio obtained by changing the pendulum weight P_1. Configuration A and C are both in near resonance, but differ in the cylinder model. More details of the construction in general and of the cylinder models in particular, including the aerodynamic characteristics, can be found in a previous report [5]. Note, however, that the configuration codes used there have no relation with these used in the present context.

2.3 Modelling of the 2-DOF oscillator properties

With reference to the structure in Fig.1, the equations of motion for the 2-DOF are derived, neglecting structural damping but including the aerodynamic forces F_N and F_T (see Fig.3), which after linearisation for small angles θ_1 and θ_2, can be written as follows:

$$I_1 \ddot{\theta}_1 + k_1 \theta_1 = R_1 \left\{ F_N + F_T (\theta_1 - \theta_2) \right\} \tag{2.1}$$

$$I_2 \ddot{\theta}_2 + k_2 \theta_2 = R_2 F_N \tag{2.2}$$

For the details of the derivation, see [14]. When the model, counter weights C_1 and C_2 and pendulum weights P_1 and P_2 are regarded as concentrated masses, and the mass of all connection elements is neglected, the inertial moment and restoring force coefficient for the two modes are given by the following expressions:

$$I_1 = (m_M + m_{C_2}) R_1^2 + m_{C_1} l_{C_1}^2 + m_{P_1} l_{P_1}^2 \qquad k_1 = m_{P_1} l_{P_1} g \tag{2.3}$$

$$I_1 = m_M R_2^2 + m_{C_2} l_{C_2}2 + m_{P_2} l_{P_2}^2 \qquad k_2 = m_{P_2} l_{P_2} g \tag{2.4}$$

while it has been assumed that the counter weights have been adjusted such as that both see-saws are in balance, as mentioned in section 1.4, with:

$$(m_M + m_{C_2}) R_1 = m_{C_1} l_{C_1} \qquad m_M R_2 = m_{C_2} l_{C_2} \tag{2.5}$$

Here m indicates the mass of the respective component with subscript M denoting the model, l is the arm length to the corresponding hinge point (*i.e.* R_2 for C_2, and R_1 for C_1, P_1 and P_2) and g is the gravity constant.

The expressions of Eqs.(2.1) and (2.2) show that, because of the absence of cross-coupling inertial terms, mode 1 and mode 2 are the natural uncoupled modes of the linearised mechanical oscillator equations. In addition to the aerodynamic coupling of the modes as expressed by the right hand terms of (2.1) and (2.2), further coupling may be caused by internal friction forces (see section 2.4) and possibly by nonlinear inertial effects.

The equation of motion describing the 1-DOF mode that is obtained by coupling the two modes (mode 0, as discussed in section 1.4) is obtained by adding Eq.(2.1) and (2.2) while putting $\theta_1 = \theta_2 \equiv \theta_0$, whereas the additional coupling forces cancel as being internal to this mode, yielding:

$$I_0 \ddot{\theta}_0 + k_0 \theta_0 = R_0 F_N \tag{2.6}$$

where $I_0 = I_1 + I_2$, $k_0 = k_1 + k_2$ and $R_0 = R_1 + R_2$.

The mechanical oscillator properties for the different single-DOF modes of the oscillator are given in Tab.1, where the restoring force stiffness k_i ($i = 0,1,2$) was determined from static force calibration (Fig.4). The frequency-amplitude characteristics (Fig.5) were derived from free oscillation tests, using a level-crossing algorithm for the oscillation period and a detection of the extremes for the oscillation amplitude. The (linearised) natural frequency f_i was then obtained from a data fit of the theoretical curve for the pendulum oscillator (see [5] for details of the procedures).

Modelling the aerodynamic forces

When the aerodynamic forces are modelled according to a quasi-steady approach, they are assumed to depend on the magnitude and direction of the *instantaneous* relative wind vector, which are derived from Fig.2 as:

$$U_{rel} \cos\alpha = (U + V_X) \cos\theta_2 + V_Y \sin\theta_2 \tag{2.7}$$

$$\tan\alpha = \frac{(U + V_X) \sin\theta_2 - V_Y \cos\theta_2}{(U + V_X) \cos\theta_2 + V_Y \sin\theta_2} \tag{2.8}$$

where V_X and V_Y are the components of the displacement velocity of the model centre, which are given by:

$$\begin{aligned} V_X &= -R_1 \dot{\theta}_1 \sin\theta_1 - R_2 \dot{\theta}_2 \sin\theta_2 \\ V_Y &= R_1 \dot{\theta}_1 \cos\theta_1 + R_2 \dot{\theta}_2 \cos\theta_2 \end{aligned} \tag{2.9}$$

Linearisation of Eqs.(2.7) and (2.8) under the condition of small angles θ_1 and θ_2, and assuming further that V_X and V_Y are small with respect to U, yields:

$$\alpha \approx \theta_2 - \frac{R_1 \dot{\theta}_1 + R_2 \dot{\theta}_2}{U} \qquad U_{rel} \approx U \tag{2.10}$$

2.4 Modelling of the damping properties

As discussed in the previous report [5] the damping properties of the 1-DOF oscillator can be expressed as a combination of viscous and frictional damping, with the former producing an additional moment that is proportional to the angular velocity and the latter a moment of constant value. The frictional damping was mainly caused by the ball bearings of the encoder, whereas the natural damping of the structure itself was predominantly of a viscous nature, due to the low-friction knife bearing supports. Both components can easily be determined from free decay measurements [5]. In the 2-DOF configuration the situation is complicated by the presence of the mechanical interaction of the two modes, but under some simplifying assumptions the damping properties can be derived from observing the decay behaviour of the separate single-DOF modes (the oscillator modes 0, 1 and 2), as explained below.

The wind-off behaviour of a 1-DOF oscillator affected by both viscous and frictional damping can be written as follows:

$$I_i \ddot{\theta}_i + k_i \theta_i = - N_i \dot{\theta}_i - M_i \, sign(\dot{\theta}_i) \tag{2.11}$$

with $i = 0$, 1 or 2. N_i is the coefficient of viscous damping and M_i that of frictional damping. Applying a two-time scale approach by assuming that the free motion is approximately a harmonic oscillation at the undamped natural frequency ω_i with an amplitude changing slowly with respect to the oscillation period, Eq.(2.11) can be written as an amplitude-transient as:

$$\frac{d\hat{\theta}_i}{dt} = - D_i \hat{\theta}_i - C_i = - \omega_i \left\{ \zeta_i \hat{\theta}_i + c_i \right\} \tag{2.12}$$

where the damping rate parameters C_i and D_i are derived from the observed amplitude decay (see [5] for details), and which are related to the damping coefficients as:

$$D_i = \zeta_i \omega_i = \frac{N_i}{2I_i} \qquad C_i = c_i \omega_i = \frac{2M_i}{\pi I_i \omega_i} \tag{2.13}$$

To describe the damping behaviour of the 2-DOF oscillator it is assumed that each mode is affected by a viscous and a frictional component, each with a part that is due to the direct motion of the mode itself and another part caused by the relative motion between the modes:

$$I_1 \ddot{\theta}_1 + k_1 \theta_1 = - N_{11}\dot{\theta}_1 - N_{12}(\dot{\theta}_1 - \dot{\theta}_2) - M_{11} sign(\dot{\theta}_1) - M_{12} sign(\dot{\theta}_1 - \dot{\theta}_2) \tag{2.14}$$

$$I_2 \ddot{\theta}_2 + k_2 \theta_2 = - N_{22}\dot{\theta}_2 - N_{21}(\dot{\theta}_2 - \dot{\theta}_1) - M_{22} sign(\dot{\theta}_2) - M_{21} sign(\dot{\theta}_2 - \dot{\theta}_1) \tag{2.15}$$

When it can be assumed that the cross-terms are predominantly caused directly by the relative motion between the modes, this interaction must be symmetric, which means that $N_{21} = N_{12}$ and $M_{21} = M_{12}$. Considering the single-DOF modes obtained by either by blocking one of the modes, or by coupling them, the oscillation behaviour is for each case given by Eq.(2.11), with the 1-DOF damping parameters N_i and M_i related to the 2-DOF parameters as:

mode 0	$\theta_1 \equiv \theta_2 \equiv \theta_0$	$N_0 = N_{11} + N_{22}$ $M_0 = M_{11} + M_{22}$
mode 1	$\theta_2 \equiv 0$	$N_1 = N_{11} + N_{12}$ $M_1 = M_{11} + M_{12}$
mode 2	$\theta_1 \equiv 0$	$N_2 = N_{22} + N_{12}$ $M_2 = M_{22} + M_{12}$

From the experimentally determined damping parameters of the different 1-DOF modes the damping parameters N_{ij} and M_{ij} of the 2-DOF motion can now be derived as:

$$2\,N_{12} = N_1 + N_2 - N_0 \qquad 2\,M_{12} = M_1 + M_2 - M_0$$
$$2\,N_{11} = N_0 + N_1 - N_2 \qquad 2\,M_{11} = M_0 + M_1 - M_2$$
$$2\,N_{22} = N_0 + N_2 - N_1 \qquad 2\,M_{22} = M_0 + M_2 - M_1$$

The results of the experimental determination of the damping properties for the different oscillator configurations are given in Tab.2. The inaccuracy of the damping rate parameters is estimated to be of the order of 5%, giving an error in N_{ij} of 0.0001 Nms and in M_{ij} of 0.0002 Nm. As configuration B is nearly identical to configuration A no mode-0 analysis was performed for the latter, while the results for the modes 1 and 2 confirm that the damping properties are indeed quite similar. Further, although the values found for configurations A and C are not identical the ratio of corresponding parameters is comparable.

Further scrutiny of the values reveals that for mode 1 the damping effect of the direct motion is approximately three times that of the relative motion, for both the viscous and the frictional component. For mode 2 the direct motion effect is approximately half the magnitude of that due to the relative motion for the viscous component. For the frictional component only that due the relative motion is relevant, the value of M_{22} being effectively zero within experimental accuracy. The results for the frictional parameters are quite plausible regarding the construction of the oscillator, with M_{11} corresponding to the friction in the bearing of angle encoder 1 and M_{12} to the friction in the bearings R_1 and R_2 and the hinges of the connection rod, while M_{22} is virtually zero as encoder 2 is contactless.

The damping character of all terms is clearly revealed by observing the decay of the total oscillator energy, which is obtained from multiplying Eqs.(2.14) and (2.15) by $\dot{\theta}_1$ and $\dot{\theta}_2$, respectively, and which after adding yields:

$$\frac{d}{dt}\frac{I_1\dot{\theta}_1^2 + k_1\theta_1^2 + I_2\dot{\theta}^2 + k_2\theta_2^2}{2} = \tag{2.16}$$

$$- N_{11}\dot{\theta}_1^2 - N_{12}(\dot{\theta}_1-\dot{\theta}_2)^2 - N_{22}\dot{\theta}_2^2 - M_{11}|\dot{\theta}_1| - M_{12}|\dot{\theta}_1-\dot{\theta}_2| - M_{22}|\dot{\theta}_2|$$

where all terms are seen to be dissipative.

2.5 Phase-space characterisation of the oscillator motion

Regarding the equations of motion, Eqs.(2.1 and 2.2), and employing the quasi-steady aerodynamic assumption discussed in section 2.3 as expressed by the effective aerodynamic angle of attack α according to Eq.(2.10), the dynamics of the oscillator for a given construction (mechanical and damping properties) and under constant experimental conditions (wind speed, air density), may be expressed as follows:

$$\dot{s} = \boldsymbol{F}(s), \qquad s = (\theta_1, \theta_2, \dot{\theta}_1, \dot{\theta}_2) \tag{2.17}$$

Here $\boldsymbol{F}$ is a (in general, nonlinear) function of the state vector s, thus describing the oscillator motion in a four-dimensional parameter space. Upon decomposition of $\boldsymbol{F}$ into a linear and a nonlinear part, where in accordance with the discussion of section 2.3 (see also [14]) the former includes only inertial and structural stiffness effects, while in the latter the aerodynamic aspects and all remaining higher-order (nonlinear) structural aspects are represented:

$$\dot{s} = \mathbf{F}_{lin}\, s + \boldsymbol{F}_{nlin}(s) \tag{2.18}$$

Note that the viscous damping components can be included in the linear term, whereas the frictional damping terms must be considered in general as nonlinear effects. If the nonlinear term is small, the system can be treated with the method of two time scales, where the oscillator motion is considered to be composed of the natural modes of the oscillation, with amplitudes changing on a time scale that is large with respect to the oscillation period. As in the present system the isolated single-DOF modes ('modes 1 and 2') correspond to the uncoupled eigenmotions of the linear part of Eq.(2.18), the motion can be written as:

$$\theta_1(t) = \hat{\theta}_1 \sin\phi_1(t) = \hat{\theta}_1 \sin(\omega_1 t) \tag{2.19}$$

$$\theta_2(t) = \hat{\theta}_2 \sin\phi_2(t) = \hat{\theta}_2 \sin(\omega_2 t + \phi_0) \tag{2.20}$$

where hatted variables denote the mode amplitude, and $\phi_0 = \phi_2(0)-\phi_1(0)$ is the initial phase difference between the modes. At any time t the instantaneous oscillation behaviour is described by the values of the mode amplitudes $(\hat{\theta}_1, \hat{\theta}_2)$, frequencies (ω_1, ω_2) and phase difference $\Delta\phi(t) = \phi_2(t)-\phi_1(t)$. For a linear system the natural frequencies ω_1 and ω_2 are constants and follow from the solution of the equations of motion. For weakly nonlinear systems the mode-shapes may remain approximately harmonic, so that the expressions (2.19 and 2.20) can still be used, but with frequencies becoming dependent on the mode amplitude. Hence, the oscillation can be characterised in the three-dimensional parameter space $(\hat{\theta}_1, \hat{\theta}_2, \Delta\phi)$ with initial conditions $(\hat{\theta}_1(0), \hat{\theta}_2(0), \phi_0)$. As the phase difference $\Delta\phi$ changes over a time scale proportional to $|\omega_1 - \omega_2|^{-1}$, its effect may be averaged out for non-resonant, weakly nonlinear forcing cases, for which the oscillation can then be characterised in the $(\hat{\theta}_1, \hat{\theta}_2)$-plane.

2.6 Free motions of the 2-DOF oscillator

A number of tests under no-wind conditions are considered to illustrate the free oscillation behaviour of the 2-DOF oscillator for the different configurations. For each test run the figures([1]) present the oscillation data as separate plots of both θ_1 and θ_2 time records, and in the form of a Lissajous figure. In addition, the oscillation records have been analysed so as to extract the variation in time of the amplitudes and frequencies of the two modes, and the phase difference between them, the latter plotted as $(\phi_2-\phi_1)/2\pi$. For each configuration different initial conditions have been considered.

Configuration A

Fig.A0a shows how a situation where initially only mode 1 is present, the coupling forces induce mode 2 to be initiated. When both modes possess nearly the same amplitude, the modes become approximately locked, as reflected by the nearly zero value of the phase difference, while the frequency of mode 2 jumps to that of mode 1. Both the excitation of the mode-2 motion and the friction locking are possible because the two natural frequencies of the independent modes are close together. As Fig.A0b reveals the inverse phenomenon is not observed: a purely mode-2 motion does not induce a mode-1 motion, which can be explained from the values of the damping parameters in Tab.2, which show in particular that the M_{12} friction term is too small to overcome the M_{11} term. Fig.A0c shows the situation where initially both modes are present but in counter-phase. During the gradual decay of both modes the phase difference decreases, and the modes become approximately locked, after which a combined decay occurs, very similar to what happens in Fig.A0a.

Configuration B

Configuration B differs from A in that now the two natural frequencies are significantly different. As a result an isolated mode 1 motion does not induce a mode 2 motion, for lack of phase correspondence (Fig.B0a). Also an isolated mode 2 motion persists at its own natural frequency (Fig.B0b). Fig.B0c shows the result when both modes are initiated with approximately the same amplitude. Both modes displays on average the undisturbed frequency, but for mode 2 the coupling forces result in a modulation of both the frequency and the amplitude decay, which follows the phase difference between the modes.

---

[1] The figures of oscillation test data are collected in the Appendix, where also the index to the figure and run codes is given.

Configuration C

Similar tests, with initially only mode 1, mode 2 or both modes in counter-phase, were carried out for configuration C as well (see Figs. C0a, C0b and C0c). Also for this configuration the natural frequencies of the modes are nearly equal, resulting in a behaviour roughly comparable to that of configuration A. However, the exact details are quite different as reflected by the Lissajous patterns. Also, the frictional lock-in is not observed in Fig.C0a as it is in Fig.A0a. Partly responsible for this may be the larger initial mode 1 amplitude in the case of Fig.C0a, so that at the point where both amplitudes are equal the frictional forces are apparently insufficient to effectuate the coupling. This is illustrated in Fig.C0g, where due to a smaller initial amplitude of mode 1, the coupling is indeed observed to occur.

Note that as under these conditions of free oscilllations, in the absence of aerodynamic forces, the viscous and frictional damping forces are the only forces that provide the coupling between the two oscillation modes, whilst simultaneously providing the only mechanism of energy dissipation. Hence, these forces are responsible for both the amplitude transient and the mode coupling, and the ratio of the different components strongly determines the combined transient 2-DOF behaviour, even when the forces are small in absolute sense in which case a similar behaviour can persist but on a larger time scale. The coupling effect they have on the apparant oscillation modes can, however, be assumed to be much less significant when studying the system under wind loading, where the aerodynamic coupling is more important than that due to the small mechanical damping forces.

3. Aeroelastic behaviour

3.1 Effect of the aerodynamic forces on the oscillation modes

The equations of motion governing the dynamics of the 2-DOF oscillator, given by Eqs.(2.1) and (2.2) as presented in section 2.3, are repeated here for convenience:

$$I_1 \ddot{\theta}_1 + k_1 \theta_1 = R_1 \left\{ F_N(\alpha) + F_T(\alpha) (\theta_1 - \theta_2) \right\} \tag{3.1}$$

$$I_2 \ddot{\theta}_2 + k_2 \theta_2 = R_2 F_N(\alpha) \tag{3.2}$$

Adopting the quasi-steady aerodynamic approach the normal force F_N and tangential force F_T are modelled by means of the static aerodynamic force coefficients c_N and c_T as:

$$F_N(\alpha) = qS c_N(\alpha) \qquad F_T(\alpha) = qS c_T(\alpha) \tag{3.3}$$

where $q = \frac{1}{2}\rho U^2$ is the dynamic pressure of the wind flow and $S = hb$ the reference area of the cylinder model, while the instantaneous angle of attack α is given by:

$$\alpha = \theta_2 - \frac{R_1 \dot{\theta}_1 + R_2 \dot{\theta}_2}{U} \tag{3.4}$$

As long as the aerodynamic forces remain small with respect to the inertial and elastic stiffness forces, the former can be regarded as being a weak perturbation of the undisturbed mechanical oscillator system. The theoretical analysis of this weakly nonlinear system can then proceed by investigating the stability of the modes of the linear system, which in the present case is the Hamiltonian (conservative) system given by the left hand side of the equations of motion (3.1) and (3.2). Possible limit-cycles of the nonlinear system and phase-space trajectories in general, can then be approximated by the orbits of the Hamiltonian system [1-3].

For the case of the 1-DOF rotational oscillator the above 'weak-forcing' method has been extended for increased wind speeds [5,8]. As the aerodynamic stiffness terms are of order U^2 and the aerodynamic damping terms of order U, the former represent the leading order effect at increased wind speeds. In the 'strong-forcing' approach the oscillator system is now regarded as a weakly perturbed Hamiltonian system, where in the latter the aerodynamic stiffness is incorporated. The orbits of this new Hamiltonian system then yields an improved approximation of the trajectories or limit-cycles of the perturbed system.

For the 1-DOF system the aerodynamic stiffness effect results in a change of the oscillation frequency and a distortion of the (originally harmonic) mode shape. The influence of the frequency on the limit-cycle behaviour is not very large, while the mode shape distortion depends on the nonlinearity of the aerodynamic forces and becomes significant only at very high wind loads, where it may result for example in divergence of the oscillator

motion. Therefore, for the description of the dynamic behaviour of the 1-DOF system the original 'weak-forcing' approach can be used even up to moderate wind loads.

As in the present 2-DOF system the phase difference between the individual modes, and hence the frequency ratio, plays an important role, it can be expected that aerodynamic stiffness effects may need to be included in the analysis even at low wind loads. As a first identification of the aerodynamic stiffness effect, its influence is investigated on the behaviour of the effective Hamiltonian system that is obtained when aerodynamic damping effects are excluded. In the analysis it may be assumed for convenience that the model cross section is symmetric around α=0, so that $F_N(-\alpha) = -F_N(\alpha)$ and $F_T(-\alpha) = F_T(\alpha)$.

Linearised aerodynamic forcing

With the following linearisation of the aerodynamic force coefficients applied:

$$c_N(\alpha) = a_1\alpha \qquad c_T(\alpha) = b_0 \tag{3.5}$$

the equations of motion become a linear system. Solutions are sought of the following form, employing the complex notation:

$$\theta_1(t) = Q_1 e^{st} \qquad \theta_2(t) = Q_2 e^{st} \tag{3.6}$$

where the s is the complex frequency and Q_1 and Q_2 complex amplitudes, with:

$$s = -D+i\omega \qquad \hat{\theta}_1 = |Q_1| \qquad \hat{\theta}_2 = |Q_2| \qquad \Delta\phi = \arg(Q_2/Q_1) \tag{3.7}$$

Upon substitution the equations of motion can be written in matrix form as:

$$\begin{pmatrix} I_1 s^2+k_1-b_0 qSR_1 & (b_0-a_1)qSR_1 \\ 0 & I_1 s^2+k_2-a_1 qSR_2 \end{pmatrix} \begin{pmatrix} Q_1 \\ Q_2 \end{pmatrix} = -s\frac{a_1 qS}{U} \begin{pmatrix} R_1^2 & R_1R_2 \\ R_1R_2 & R_2^2 \end{pmatrix} \begin{pmatrix} Q_1 \\ Q_2 \end{pmatrix} \tag{3.8}$$

where the left hand side represents the Hamiltonian system of the mechanical oscillator with the aerodynamic stiffness included, while the right hand side represents the aerodynamic damping effects. The natural frequencies and modes of the Hamiltonian system follow from the eigenvalues of the matrix on the left, which allows the following two modes to be identified:

mode 1: $$\omega_1^2 = \frac{k_1 - b_0 qSR_1}{I_1} \qquad \frac{Q_2}{Q_1} = 0$$

mode 2: $$\omega_2^2 = \frac{k_2 - a_1 qSR_2}{I_2} \qquad \frac{Q_1}{Q_2} = \frac{(a_1 - b_0)\, qSR_1}{I_1(\omega_1^2 - \omega_2^2)}$$

This shows that mode 1, the 'translation mode', is still a purely θ_1-motion, because the θ_2-equation remains decoupled when the aerodynamic stiffness is included in the Hamiltonian system. As a result the rotation motion is not excited by the translation motion. Due to the

coupling of θ_2 to the θ_1-equation, the second mode includes a combination of rotation and translation. However, as the θ_2-equation is decoupled the frequency of this mode is the same as for the single-DOF rotation motion which would result if the translational freedom were restrained. This mode can hence be regarded as an independent θ_2-motion, which induces a θ_1-motion as if the latter were subjected to a forced excitation. Note that in agreement with this concept the two motions in the second mode may be either in-phase or counter-phase, depending on the frequency ratio ω_2/ω_1 being either smaller or larger than unity, and the sign of $(a_1\text{-}b_0)$. With the coefficients representing the linearisation of the force characteristics around α=0, the configurations under consideration here typically display $a_1<0$ and $b_0>0$. Therefore, the effect of an increase in wind speed (and hence, q) is in this case to decrease ω_1 and increase ω_2, where for the present configuration with $R_2I_1/R_1I_2 \approx 6$, the effect on ω_2 is largest. Note furthermore that when $\omega_2>\omega_1$ both motions are in-phase $(A_1/A_2>0)$.

Nonlinear aerodynamic forcing

The complete aerodynamic stiffness terms are obtained by considering the full system of Eqs.(3.1) and (3.2), but omitting the dynamic effects from the expression for the angle of attack, Eq.(3.4), resulting in:

$$I_1 \ddot{\theta}_1 + k_1 \theta_1 = R_1 \left\{ F_N(\theta_2) + F_T(\theta_2) (\theta_1 - \theta_2) \right\} \tag{3.9}$$

$$I_2 \ddot{\theta}_2 + k_2 \theta_2 = R_2 F_N(\theta_2) \tag{3.10}$$

Although the concept of oscillation modes is not as meaningful for nonlinear systems as it is for linear systems, as without the possibility of superposition it is no longer possible to express a solution as a linear combination of such modes, it is still possible here to identify two different independent modes, which can be regarded as the generalisation of the modes found in the linear analysis. To this end it is observed that the above system can be considered to be of the following general form (where ω_1 and ω_2 should here be interpreted as the mode frequencies of the undisturbed system):

$$\ddot{\theta}_1 + \omega_1^2 \theta_1 = F_1(\theta_1,\theta_2) \tag{3.11}$$

$$\ddot{\theta}_2 + \omega_2^2 \theta_2 = F_2(\theta_2) \tag{3.12}$$

As the second equation is decoupled from the first, it is directly obvious that it is again possible for a pure θ_1-motion to exist, which is recognised as the translation mode, and characterised by the following Hamiltonian expression:

$$\frac{d}{dt}\left(\frac{\dot{\theta}_1^2 + \omega_1^2 \theta_1^2}{2} - \int F_1(\theta_1,0)\, d\theta_1 \right) = 0 \tag{3.13}$$

Note that in the present case F_1 is linear in θ_1, see Eq.(3.9), so that the resulting mode shape is harmonic.

The θ_2-motion is not affected by θ_1 as it is governed independently by the decoupled second equation, which is also of Hamiltonian form:

$$\frac{d}{dt}\left(\frac{\dot{\theta}_2^2 + \omega_2^2 \theta_2^2}{2} - \int F_2(\theta_2) d\theta_2 \right) = 0 \tag{3.14}$$

This motion induces a θ_1-motion as if through a forced excitation. It can be shown that now again an independent mode can be obtained, where both motions coexist in (counter-)phase. In that case it is possible to write:

$$\theta_1 = g(\theta_2) \tag{3.15}$$

with which the θ_1-equation, Eq.(3.11), becomes:

$$\ddot{\theta}_1 + \omega_1^2 \theta_1 = F_1(\theta_1, g^{-1}(\theta_1)) = F_1^*(\theta_1) \tag{3.16}$$

which can again be written in a Hamiltonian form. The specific expression for g is found from the condition that Eqs.(3.11,12 and 15) be satisfied simultaneously. From Eq.(3.15) the following expression is derived by repeated differentiation:

$$\ddot{\theta}_1 = g''(\theta_2)\, \dot{\theta}_2^2 + g'(\theta_2)\, \ddot{\theta}_2 \tag{3.17}$$

in which the prime indicates differentiation with respect to the function argument, θ_2. Also, solution of the decoupled θ_2-equation, Eq.(3.14), directly reveals that:

$$\dot{\theta}_2^2 = f(\theta_2) \tag{3.18}$$

Note that the expression for f depends on ω_2 and F_2. Replacing all θ_1-terms in Eq.(3.11) with the appropriate θ_2-functions, by means of Eqs.(3.17) and (3.15) and substituting Eqs.(3.12) and (3.18), the following equation that determines g is obtained:

$$f(\theta_2)\, g''(\theta_2) + \left[F_2(\theta_2) - \omega_2^2 \theta_2 \right] g'(\theta_2) + \omega_1^2\, g(\theta_2) = F_1(g(\theta_2), \theta_2) \tag{3.19}$$

which relates g to ω_1, ω_2 and the forcing functions F_1 and F_2. The complexity of the above equation prevents an analytic solution for g to be obtained in general, but note that when both F_1 and F_2 are linear functions, it is easily verified from substitution that g is linear in θ_2. As a consequence $\theta_1/\theta_2 = g(\theta_2)/\theta_2$ is a constant, which corresponds to the result of the linear analysis given earlier.

This analysis shows that also for the nonlinear equivalent Hamiltonian system obtained by including the aerodynamic stiffness effect, it is possible to distinguish two independent oscillation modes. The first mode is a purely θ_1-motion (translation), which is moreover harmonic in shape as the aerodynamic forces remain constant. The second mode is a mixed mode of θ_1- and θ_2-motions, taking place at the frequency dictated by the rotation motion, and which induces a θ_1-motion as if through a forced oscillation. As in this mode the two motions are either in-phase or counter-phase, the trajectory in the (θ_1,θ_2) plane follows a single curve for both increasing and decreasing angles.

3.2 Single-DOF galloping tests

Before proceeding to the aeroelastic behaviour of the full 2-DOF oscillator configuration, it is illustrative to consider the galloping behaviour of the configuration in the different 1-DOF configurations that were identified in section 1.4. By restraining either one of the motions the translational 'mode 1' or the rotational 'mode 2' is obtained, while applying a rigid mechanical coupling between the motions results in the rotational 'mode 0'. The equations of motion for these modes, according to the quasi steady approach, are given by:

$$\text{mode 0:} \quad I_0\ddot{\theta}_0 + k_0\theta_0 = R_0 F_N(\alpha) \qquad \alpha = \theta_0 - \frac{R_0\dot{\theta}_0}{U} \tag{3.20}$$

$$\text{mode 1:} \quad I_1\ddot{\theta}_1 + k_1\theta_1 = R_1\left\{F_N(\alpha) + F_T(\alpha)\,\theta_1)\right\} \qquad \alpha = -\frac{R_1\dot{\theta}_1}{U} \tag{3.21}$$

$$\text{mode 2:} \quad I_2\ddot{\theta}_2 + k_2\theta_2 = R_2 F_N(\alpha) \qquad \alpha = \theta_2 - \frac{R_2\dot{\theta}_2}{U} \tag{3.22}$$

Rotational galloping modes

The above equations show that both mode 0 and mode 2 are indeed rotational galloping modes identical to the 1-DOF see-saw oscillator considered in previous investigations, so that the galloping behaviour for these modes should compare directly to the results found there [5]. Including the viscous and frictional damping components, see Eq.(2.11), the motion is described by:

$$I_i\,\ddot{\theta}_i + k_i\,\theta_i = -N_i\,\dot{\theta}_i - M_i\,sign(\dot{\theta}_i) + \tfrac{1}{2}\rho U^2 hbR_i\,c_N(\alpha) \tag{3.23}$$

with $i = 0$ or 2. Applying the averaging approach of the 'weak forcing' method (*cf.* also section 2.4) the following amplitude-transient equation is obtained:

$$\frac{d\hat{\theta}_i}{dt} = -\frac{N_i}{2I_i}\,\hat{\theta}_i - \frac{2}{\pi}\frac{M_i}{I_i\omega_i} - \frac{\mu_i}{2}\frac{U}{R_i}\,c_\zeta(\hat{\alpha})\,\hat{\theta}_i \tag{3.24}$$

where the mass parameter $\mu = \rho hbR_i^3/I_i$, and with the aerodynamic damping coefficient c_ζ defined as:

$$c_\zeta \doteq -\frac{U}{\omega_i^2 R_i}\left[\frac{c_N(\alpha)}{\hat{\theta}_i^2}\dot{\theta}_i\right] = \left[\frac{c_N(\alpha)\,\alpha}{\hat{\alpha}^2}\right] \tag{3.25}$$

where square brackets indicate the averaging operator([1]).

---

[1] For a function periodic in t, with period T, averaging is defined as: $[f(t)] = \frac{1}{T}\int_0^T f(t)\,dt$.

Note that Eq.(3.24) confirms the statement made earlier that for a small change in the frequency has no great influence on the 1-DOF galloping behaviour. The above equation is written in dimensionless form as:

$$\frac{d\hat{\theta}_i}{d\omega_i t} = -\zeta_i\,\hat{\theta}_i - c_i - \frac{\mu_i}{2} u_i\, c_\zeta(\hat{\alpha})\,\hat{\theta}_i \tag{3.26}$$

with the reduced wind speed $u_i = U/(\omega_i R_i)$. For (stable or unstable) limit-cycle oscillations the left hand side vanishes, so that from the observed limit-cycle amplitudes the corresponding value of c_ζ can be calculated as:

$$c_\zeta = -2\,\frac{\zeta_i\,\hat{\theta}_{LC} + c_i}{\mu_i u_i \hat{\theta}_{LC}} \tag{3.27}$$

In Fig.7a the 1-DOF rotational galloping results are given for the cylinder with the rectangular cross section (25 mm × 40 mm) that was applied in configurations A and B, and in Fig.7b for the square cross section (30 mm × 30 mm) of configuration C. In each figure the measured static c_N-curve [5] is shown in the top graph, and the limit-cycle amplitudes as a function of wind speed U in the centre. At the bottom the values of c_ζ derived with Eq.(3.27) are depicted, where according to the quasi-steady theory are plotted against the value of the aerodynamic amplitude, that is given by:

$$\hat{\alpha} = \hat{\theta}\,\sqrt{\frac{1+u^2}{u^2}} \tag{3.28}$$

The curve in the lower graph gives c_ζ as predicted by the quasi-steady theory [5] and based on the static c_N-data. In the case of the rectangular cross section (Fig.7a) the measured values for the different configuration agree well, and correspond to the earlier experiments [5], where the same deviation from the theoretical curve was observed. Although the data for the rectangular cross section (Fig.7b) is rather sparse, a fair agreement is again observed in this case. Note that the data for the smaller amplitudes is based on the amplitude of unstable limit cycles, and may therefore be subject to increased inaccuracy.

Translational galloping mode

Due to the presence of the extra contribution of the tangential force F_T in Eq.(3.21) the motion of mode 1 is not strictly identical to that of one with a purely vertically translating cylinder, but for the low-forcing galloping behaviour this has no effect. This is revealed by the galloping equation, which can be written in the same form as for the rotational mode Eq.(3.24), and with the adapted definition of the aerodynamic damping coefficient c_ζ being:

$$c_\zeta \doteq -\frac{U}{\omega_1^2 R_1}\left[\frac{c_N(\alpha)+c_T(\alpha)\,\theta_1}{\hat{\theta}_i^2}\,\dot{\theta}_1\right]$$
$$= \left[\left\{c_N(\alpha)+\frac{U}{\omega_i^2 R_1}\,c_T(\alpha)\,\dot{\alpha}\right\}\frac{\alpha}{\hat{\alpha}^2}\right] = \left[\frac{c_N(\alpha)\,\alpha}{\hat{\alpha}^2}\right] \tag{3.29}$$

where for any periodic motion the contribution of c_T vanishes identically upon averaging. Although the governing equations for this translational galloping mode is identical to those of the rotational modes, the true structural galloping behaviour is different in that, instead of Eq.(3.27), the structural and aerodynamic amplitudes are now related as:

$$\hat{\alpha} = \frac{\hat{\theta}}{u} \tag{3.30}$$

Because of this linear relationship stable limit-cycle amplitudes are predicted to occur at much larger values of the oscillator amplitude than in the case of the rotational modes. For the configuration under consideration, the predicted amplitudes increase beyond the limits of the test section, and furthermore also beyond the bounds of validity of the theory where relatively small angles are assumed. Therefore, no distinct limit-cycle behaviour of this mode can be recorded, as illustrated in Fig.8, where the theoretical stability boundaries are calculated for the different configurations (using an approximation of the c_ζ-curves of Fig.7). Only the lower branch (of unstable limit-cycle oscillation) is observed in the region of wind speeds and amplitudes of practical interest. Qualitatively, a similar behaviour was indeed observed in practice, where mode 1 oscillations were predominantly damped for all combinations of wind speed and oscillation amplitude investigated, except for configuration C, where a weakly unstable behaviour occurred at a sufficiently high wind speed and initial amplitude.

3.3 2-DOF galloping tests

A number of galloping tests were carried out, for each of the different 2-DOF oscillator configurations, to get an impression of the dynamic behaviour of the system and to try to identify the possible existence of stable limit-cycle oscillations. Note that in the 1-DOF oscillator it is fairly easy to identify unstable limit cycles as well, as the initial condition of the system is characterised by a single parameter (the oscillation amplitude), which allows a systematic investigation of this one-dimensional parameter-space. For the 2-DOF case the initial condition is given in three-dimensional space (two amplitudes and a phase difference), a full investigation of which is quite impractical - even more because an oscillation starting from a static situation is limited to either in-phase or counter-phase.

In the next discussion several oscillation trajectories are followed in the $(\hat{\theta}_1, \hat{\theta}_2)$ amplitude plane (Figs.9-11). Note that as the oscillation is characterised in a three-dimensional $(\hat{\theta}_1, \hat{\theta}_2, \Delta\phi)$ space, the amplitude plane provides a projection of the parameter space, and hence cannot be considered to yield a phase-plane representation. Each run is identified by the configuration code in the upper right corner of the graph, and a letter denoting the individual run given next to the circle that indicates the recorded initial state of the oscillation. The full configuration-run code allows the corresponding oscillation record figure to be retrieved in the Appendix, which presents time records of both oscillation modes as well as derived data, such as instantaneous values of the mode frequencies and amplitudes and the phase difference. Note that abbreviated codes, as explained in the Appendix, are used for reference in the main text and for the figure numbering of the Appendix.

Configuration A: model 25 mm x 40 mm; frequency ratio 0.98

In Fig.9a several runs with different initial conditions are given, with separate graphs for oscillations starting with predominantly mode-1 (top), mode-2 (centre) or in-phase (bottom) motions. This shows that, depending on the initial conditions, either the equilibrium positions is approached (A3h,f,k), or a limit-cycle oscillation results where both modes are present (A3a,b,c,e,i,j), with approximately $(\hat{\theta}_1, \hat{\theta}_2)=(4^o,11^o)$. In this limit cycle both modes are nearly in phase, as can be seen from *e.g.* Figs.A3a,b, with the phase difference $\Delta\phi/2\pi$ in the order of 0.01; the (slightly) positive value indicating that the orbit in the (θ_1,θ_2) plane is traversed clockwise with θ_2 leading θ_1. The θ_2-amplitude is slightly larger than that for the pure mode-2 motion under the same conditions (see Fig.7a), which may result from the effect of the additional θ_1-motion on both the aerodynamic coupling and the damping forces.

The same situation is observed for a slightly increased wind speed (Fig.9b and c), with the limit-cycle properties varying only little. Under the conditions of Fig.9c, however, some records (A2c,d,g) appear to suggest the existence of an additional, significantly different limit cycle, with $(\hat{\theta}_1, \hat{\theta}_2)=(18\text{-}20^o,13^o)$, a distinct negative phase difference and with a frequency on average at a lower level than that of the first limit cycle. Also, a distinct variation in the orbit shape is observed, which is reflected in particular in fluctuations of the amplitude and frequency of the rotational mode (θ_2). However, as witnessed from run A2j, under this condition this oscillation pattern is not entirely stable, as the oscillation is seen to return to the 'first' limit cycle. Note that an oscillation pattern reminiscent of that of the 'second limit-cycle' was encountered in transient at a lower wind speed, cf. Fig.A1d. With a further increase in wind speed, Fig.9d, the situation is reversed, and the 'first limit-cycle' seems to have disappeared while the 'second limit-cycle' has indeed been established. Note that the instability in the oscillation pattern has further increased, as seen in Figs.A4b and f, especially as the properties of the rotation-mode are concerned. This is shown in more detail in Fig.12, which depicts a selected time interval from run A4f.

In general, the galloping behaviour of the θ_2-motion can be related quite well to that of the 1-DOF rotational behaviour. This then provides an excitation mechanism for the θ_1-motion, the amplitude of which would then be expected to probably increase with wind speed. A summary of the properties of the 'approximate' limit-cycle oscillations are given in the table below.

code	U (m/s)	'first type' limit cycle			'second type' limit cycle		
		$(\hat{\theta}_1, \hat{\theta}_2)$	$\Delta\phi/2\pi$	f (Hz)	$(\hat{\theta}_1, \hat{\theta}_2)$	$\Delta\phi/2\pi$	f (Hz)
A3	3.7	$(4^o, 11^o)$	0.01	0.478			
A1	5.1	$(3^o, 11^o)$	0.01	0.490			
A2	7.2	$(4^o, 12^o)$	0.01	0.490	$(18\text{-}20^o, 13^o)$	-0.08	0.450
A4	8.8				$(23\text{-}27^o, 13^o)$	-0.10	0.445

Together with the observation that the phase difference between the modes is nearly zero, the observed 'first type' limit-cycle appears to correspond to the mixed-mode limit cycle discussed previously in section 3.1. Note the clear change of the 'basin of attraction' of the limit-cycle with increased wind speed, as evidenced from comparing motions that start approximately as pure θ_1-motions. At low wind speeds (A3a, A1c) both mode frequencies are nearly the same and the interaction allows the rotational motion to be excited. At higher wind speeds (A2a, A4c), however, the aerodynamic stiffness effects have apparently driven the two frequencies so far apart to prevent this interaction to take sufficient effect.

The 'second type' limit-cycle has a quite distinct character, with a significant phase difference between the modes and a much larger unsteadiness. From the experimental observations, however, it remains unclear if the latter must be contributed to random disturbances of the 'quasi-steady equations of motion' due to the unsteady wind force components discarded in the quasi-steady modelling, or whether it is a fundamental property of the quasi-steady system, resulting in periodic or even chaotic behaviour in the phase-space.

Finally, it can be concluded that due to the fact that the natural frequencies of the two free oscillation modes are close together (near-resonance case), a strong interaction between modes results under the effect of aerodynamic forces. This means that when an analytic analysis of the oscillator dynamics is attempted using perturbation methods, the phase difference must be included as well. Furthermore, the significant variations observed in the occurring frequencies strongly suggest the need to model the aerodynamic stiffness effects.

Configuration B: model 25 mm x 40 mm; frequency ratio 1.27

Configuration B is aerodynamically similar to configuration B, but with the translational mode frequency being significantly lower, it is expected that for due to the absence of internal resonance the interaction of the modes is much reduced. This is indeed confirmed in Fig.10, and only a single limit cycle was observed. As shown in Fig.7a the amplitude of the rotational mode 2 corresponds to that of the 1-DOF motion with the other mode restrained. Therefore, it can be concluded that this behaviour can be understood as the nearly 1-DOF galloping of the unstable rotational mode. This excites the translational motion but due to the large frequency separation the translational amplitude is much smaller than for configuration A. Note also that mode shape, phase difference and frequencies (see also the table below) are comparable to the limit cycle of the 'first type' observed for configuration A.

code	U (m/s)	limit cycle		
		$(\hat{\theta}_1, \hat{\theta}_2)$	$\Delta\phi/2\pi$	f (Hz)
B1	3.7	(0.5°,9.5°)	0.03	0.480
B2	7.2	(1.5°,11°)	0.02	0.495

Configuration C: model 30 mm x 30 mm; frequency ratio 1.01

In this configuration both free oscillation modes are again in near-resonance, so that a strong interaction between the modes can be anticipated. The difference with Configuration A lies in the aerodynamic properties of the cylinder. As revealed from a comparison of Figs.7a and 7b, the cylinder with the rectangular cross section displays under the prevailing damping conditions a hard-galloping behaviour, where instability requires a finite initial oscillation amplitude. As a consequence, the equilibrium position $(\theta_1,\theta_2)=(0,0)$ remained stable under all conditions considered. For the square cross section instability of the equilibrium position occurred at a sufficient wind speed for the 1-DOF rotational modes (Fig.7b). Hence the 2-DOF system will become unstable as well, where the excitation of the translational motion by the θ_2-mode can become significant due to the near resonance in frequency.

Figure 11 confirms that indeed for sufficiently high wind speeds the equilibrium position becomes unstable (C3a, C4a), and that a sustained oscillation results with both modes present. In addition to the growth of the mode amplitudes with wind speed, the unsteadiness of the oscillation pattern is seen to increase as well, but in contrast to the situation for the 'second type' limit cycle for configuration A, it appears that now particularly the translational motion is affected (*cf.* C3a,b,c and C4a,b). Both records of oscillations starting from rest (C3a and C4a) or from a rotation-only mode (C3c) show large modulations of the amplitude of the

translational motion. Records C3b, C3d and C4b show details of sustained oscillations, where this modulating oscillation pattern is clearly illustrated. Note that the growth and decay of the translation amplitude is accompanied by, respectively, negative and positive values of the phase difference between the modes. In the present context it could not be established whether this pattern is only a transient behaviour, where the modulation effect may decrease gradually (but prone to excitation by random disturbances), or that it represents an inherent periodic or chaotic pattern of the system. (In phase-space these possibilities would correspond to, respectively, a singular point, a periodic orbit, or a chaotic attractor).

code	U (m/s)	limit cycle		
		$(\hat{\theta}_1, \hat{\theta}_2)$	$\Delta\phi/2\pi$	f (Hz)
C1	5.0	-	-	-
C2	7.1	(3.5°,13.5°)	0	0.53
C3	8.8	(4.5°,15°)	0	0.53
C4	10.3	(4-8°,15.5°)	0	0.52

4. Discussion and conclusions

In this study the non-linear dynamic behaviour has been considered of a mechanical oscillator with two degrees of freedom under the effect of aerodynamic forces. The present oscillator configuration is an extension of the 1-DOF aeroelastic oscillator investigated previously. Its construction is such that the two independent motions that characterise the free oscillation behaviour (the uncoupled modes) are those where the model cylinder either performs a nearly translational motion (mode 1) or a rotational motion similar to that of the 1-DOF configuration considered previously (mode 2). Free oscillation tests were used to determine the mechanical and damping properties of the construction.

Under aeroelastic conditions the two originally independent modes become coupled by the aerodynamic forces acting on the cylinder. A first impression of the effect of this can be gained by considering the Hamiltonian system that results when the aerodynamic stiffness of the system is included. This is achieved by omitting all dynamic effects on the aerodynamics, and assuming all fluid forces a function only of the instantaneous angle of attack produced by the angular displacement of the cylinder. For the system under consideration the rotation mode is decoupled from the translation mode. Hence, two independent modes can be distinguished, *viz.* one which is purely translational and a second where the rotation motion is present and excites a translational motion in (counter-)phase. These two modes can also be identified in the presence of nonlinear aerodynamic force characteristics, although due the nonlinearity of the system the possibility of other periodic oscillation modes cannot be excluded.

Dynamic tests were performed at various wind speeds and for different oscillator configurations, in order to study in particular the influence of the aerodynamic characteristics and the frequency ratio of the modes. Especially the occurence of self-sustained oscillations were investigated. In contrast to the 1-DOF system studied earlier, the resulting dynamic behaviour is complicated by the interaction of the two oscillation modes, in particular when the mode frequencies are of the same order. Mostly, the galloping behaviour of the 2-DOF system could be understood from the instability of the rotational mode, and with its excitation effect on the translational mode being strongly determined by the frequency ratio of the two modes. In the absence of resonance the translational mode is only slightly excited. For near-resonance the translational mode becomes appreciable, while configuration A displayed the transfer to a different limit cycle type, with a significant phase difference between the motions. Also, under several conditions the oscillation pattern was observed to display significant modulation effects, with mode amplitudes and phase differences changing

periodically. In the present experimental context it could not be established whether such patterns represent only a transient behaviour, where the modulation effect may decrease gradually (but prone to excitation by random disturbances), or that they indicate an inherent periodic or chaotic behaviour of the system.

The observations of strong mode interactions strongly suggest that when attempting to construct an analytical model of the behaviour, the aerodynamic stiffness effects and a phase relation must be included to describe the dynamic behaviour of the 2-DOF system.

References

1. B.W. van Oudheusden, 1992: Investigation of an aeroelastic oscillator: analysis of one-degree-of-freedom galloping with combined translational and torsional effects, *Report LR-707*, TU Delft, Fac. of Aerospace Eng.
2. T.I. Haaker, A.H.P. van der Burgh, 1992: On the dynamics of aeroelastic oscillators with one degree of freedom, *Report TWI 92-96*, TU Delft, Fac. of Techn. Math. & Inf.; also published in: *SIAM J. Appl. Math.*, vol. 54 (1994), pp. 1033-1047.
3. T.I. Haaker, 1994: Dynamical behaviour of simple aeroelastic oscillators with one degree of freedom, *Report TWI 94-63*, TU Delft, Fac. of Techn. Math. & Inf.
4. B.W. van Oudheusden, 1993: Development of an aeroelastic oscillator: design and initial results of an experimental set-up, *Report LR-746*, TU Delft, Fac. of Aerospace Eng.
5. B.W. van Oudheusden, 1995: Investigation of large-amplitude 1-DOF rotational galloping, Report LR-794, TU Delft, Fac. of Aerospace Eng., ISBN 90-5623-023-9.
6. B.W. van Oudheusden, 1995: On the quasi-steady analysis of one-degree-of-freedom galloping with combined translational and rotational effects, *Nonlinear Dynamics*, vol. 8, pp. 435-451
7. A.H.P. van der Burgh, T.I. Haaker, B.W. van Oudheusden, 1995: A new aeroelastic oscillator, theory and experiments, *ASME 15th Biennial Conf. on Mechanical Vibration and Noise*, Boston, 17-21 Sept. 1995, Proc. DE-Vol.84-1, pp. 299-303.
8. T.I. Haaker, B.W. van Oudheusden, 1996: One-degree-of-freedom rotational galloping under strong wind conditions, *Report TWI 96-24*, TU Delft, Fac. of Techn. Math. & Inf., ISSN 0922-5641; to be published in *Int. J. of Nonlinear Mechanics.*
9. B.W. van Oudheusden, 1996: Rotational one-degree-of-freedom galloping in the presence of viscous and frictional damping, *J. Fluids & Structures*, vol 10 (7).
10. R.D. Blevins, 1990: *Flow induced vibrations*, 2nd ed., New York: Van Nostrand Rheinhold Company.
11. G.V. Parkinson, J.D. Smith, 1964: The square prism as an aeroelastic nonlinear oscillator, *Quart. Journ. Mech. & Appl. Math.*, vol. 17, pp. 225-239.
12. G.V. Parkinson, 1989: Phenomenon and modelling of flow-induced vibrations of bluff bodies, *Prog. Aerospace Sci.*, vol. 26, pp. 169-224.
13. M.N. Mikhail, 1979: Optimum design of wind tunnel contractions, *AIAA Journal*, vol. 17, pp. 471-477.
14. T.I. Haaker, 1996: Quasi-steady modelling and asymptotic analysis of aeroelastic oscillators, *Ph.D. Thesis,* TU Delft, Fac. of Techn. Math. & Inf., ISBN 90-9009730-9.

Table 1: Mechanical properties of the different oscillator configurations.
(Values for natural frequency and restoring force stiffness have been determined experimentally, apart from values between brackets which were inferred.)

configuration code:	A	B	C
main dimensions:			
model span b (m):	0.35		0.35
arm R_1 (m):	0.20		0.20
arm R_2 (m):	0.15		0.15
model cross-section:			
width × height	40 mm × 25 mm		30 × 30 mm
natural frequency:			
f_0 (Hz)	0.462	(0.369)	(0.468)
f_1 (Hz)	0.462	0.357	0.468
f_2 (Hz)	0.452	0.452	0.472
frequency ratio: f_2 / f_1	0.978	1.266	1.009
restoring force stiffness:			
k_0 (Nm)	3.008	(1.827)	(3.008)
k_1 (Nm)	2.683	1.507	2.686
k_2 (Nm)	0.320	(0.320)	0.322
moment of inertia:			
I_0 (kg.m^2)	0.357	0.340	0.348
I_1 (kg.m^2)	0.318	0.300	0.311
I_2 (kg.m^2)	0.040	0.040	0.037
inertial moment ratio: I_2 / I_1	0.126	0.133	0.119
mass parameter:			
μ_0	0.00200	0.00208	0.00153
μ_1	0.00041	0.00044	0.00032
μ_2	0.00140	0.00140	0.00113

Table 2: Damping properties of the different oscillator configurations.

Configuration: A	mode 0	mode 1	mode 2	
I_i (kg.m^2)	0.357	0.318	0.040	
k_i (Nm)	3.008	2.683	0.320	
ω_i (rad/s)	2.903	2.903	2.840	
viscous component				
D_i (s^{-1})	0.0028	0.0034	0.0097	N_{11} = 0.00169 (Nm.s)
$\zeta_i = D_i/\omega_i$	0.0010	0.0012	0.0034	N_{22} = 0.00031
$N_i = 2D_i I_i$ (Nm.s)	0.0020	0.0022	0.0008	N_{12} = 0.00047
friction component				
C_i (deg/s)	0.091	0.137	0.322	M_{11} = 0.00253 (Nm)
$c_i = C_i/\omega_i$ (rad)	0.0005	0.0008	0.0020	M_{22} = 0.00005
$M_i = \frac{1}{2}\pi c_i k_i$ (Nm)	0.00259	0.00347	0.00099	M_{12} = 0.00094

Configuration: B	mode 0	mode 1	mode 2	
I_i (kg.m^2)	0.340	0.300	0.040	
k_i (Nm)	1.827	1.507	0.320	
ω_i (rad/s)	1.159	2.243	2.840	
viscous component				
D_i (s^{-1})		0.0034	0.0096	
$\zeta_i = D_i/\omega_i$		0.0015	0.0034	
$N_i = 2D_i I_i$ (Nm.s)		0.0020	0.0008	
friction component				
C_i (deg/s)		0.180	0.355	
$c_i = C_i/\omega_i$ (rad)		0.0014	0.0022	
$M_i = \frac{1}{2}\pi c_i k_i$ (Nm)		0.00332	0.00110	

Table 2 (continued): Damping properties of the different oscillator configurations.

Configuration: C	mode 0	mode 1	mode 2	
I_i (kg.m^2)	0.348	0.311	0.037	
k_i (Nm)	3.008	2.686	0.322	
ω_i (rad/s)	2.941	2.941	2.966	
viscous component				
D_i (s^{-1})	0.0020	0.0026	0.0075	N_{11} = 0.00123 (Nm.s)
$\zeta_i = D_i/\omega_i$	0.0007	0.0009	0.0025	N_{22} = 0.00016
$N_i = 2D_i I_i$ (Nm.s)	0.0014	0.0016	0.0006	N_{12} = 0.00039
friction component				
C_i (deg/s)	0.096	0.140	0.250	M_{11} = 0.00273 (Nm)
$c_i = C_i/\omega_i$ (rad)	0.0006	0.0008	0.0015	M_{22} = -0.00003
$M_i = \frac{1}{2}\pi c_i k_i$ (Nm)	0.00269	0.00351	0.00074	M_{12} = 0.00078

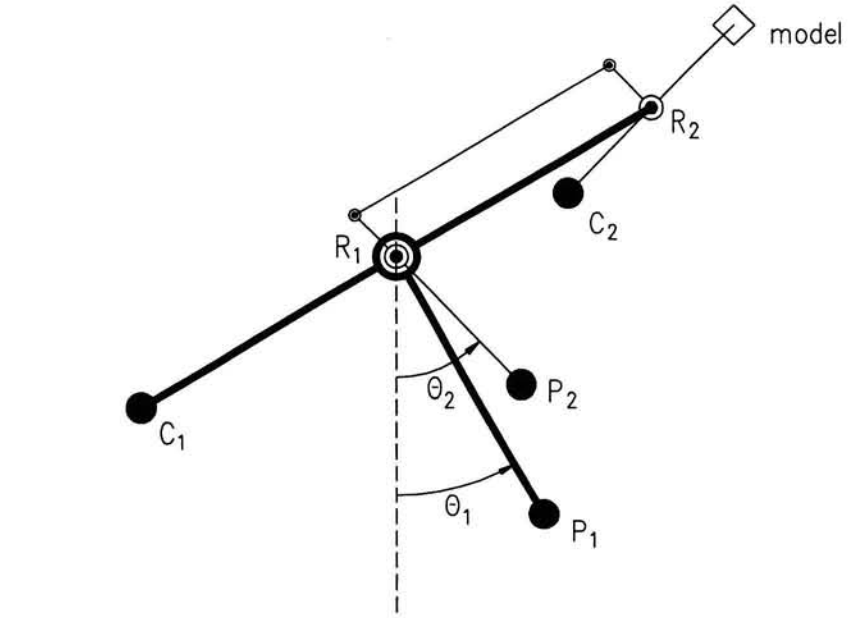

(a) Definition of the geometry.

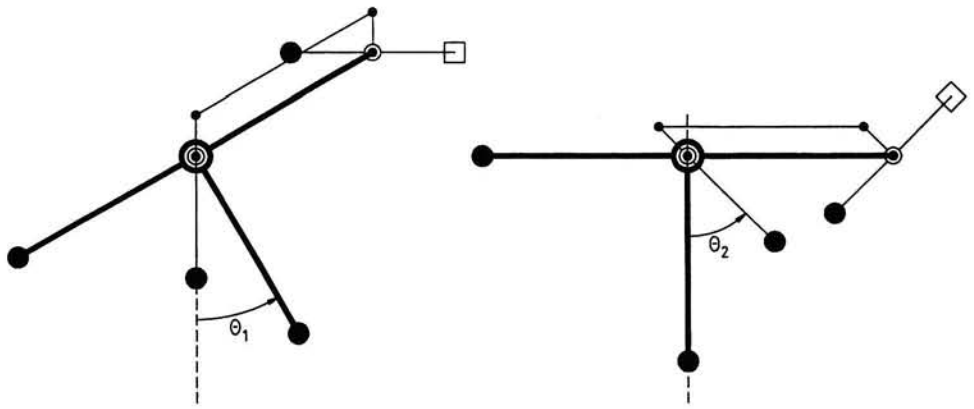

(b) Mode shapes.

Figure 1: Schematic construction of the 2-DOF oscillator configuration.

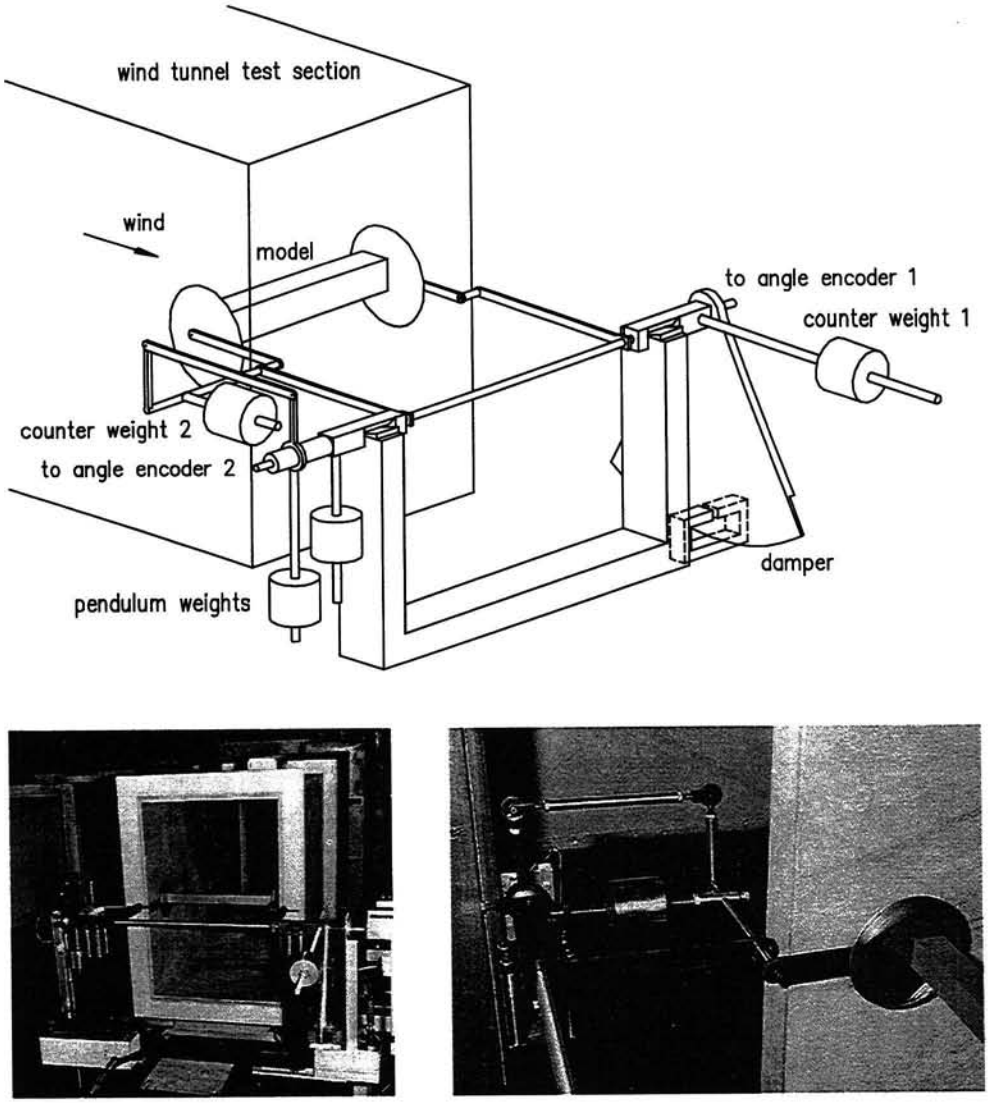

Figure 2: The 2-DOF oscillator set-up.

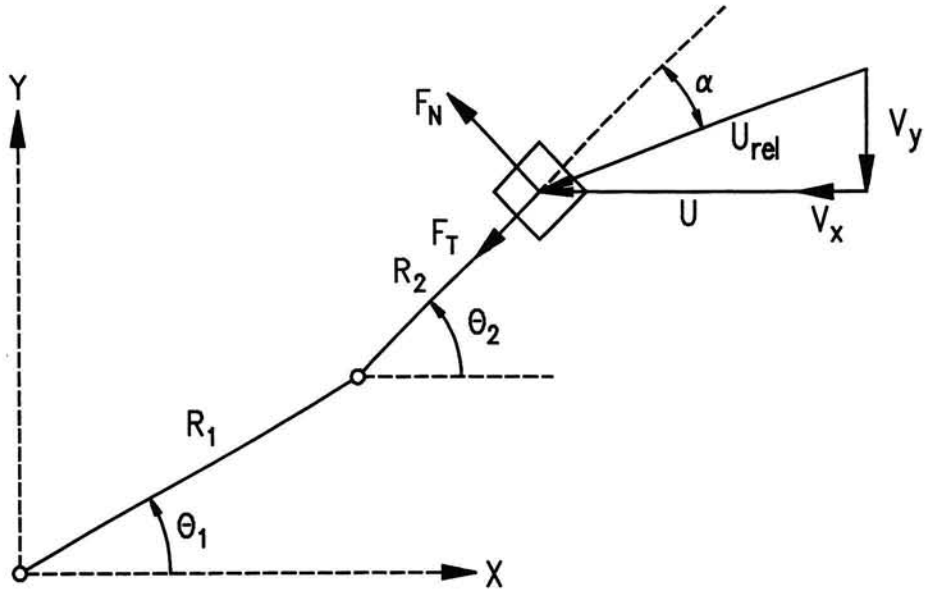

Figure 3: Definition of the aerodynamic configuration.

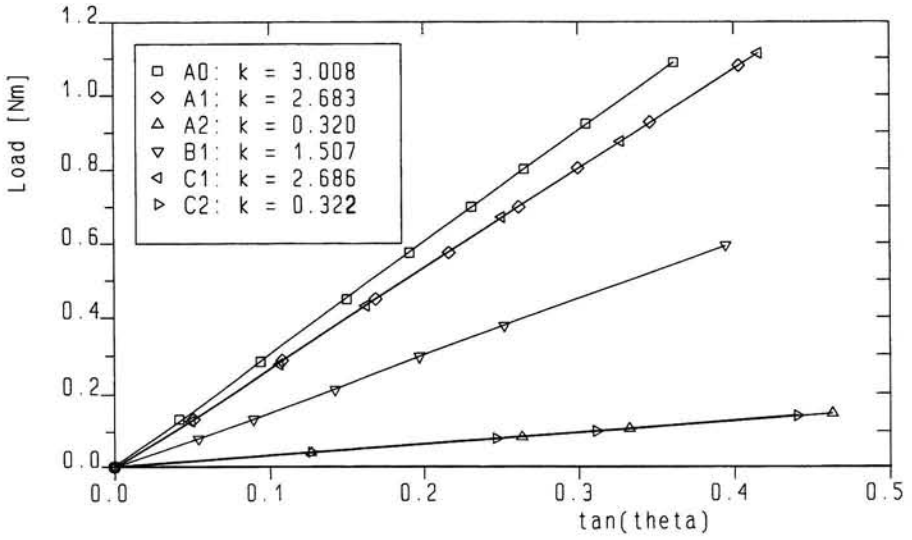

Figure 4: Determination of restoring force stiffness.

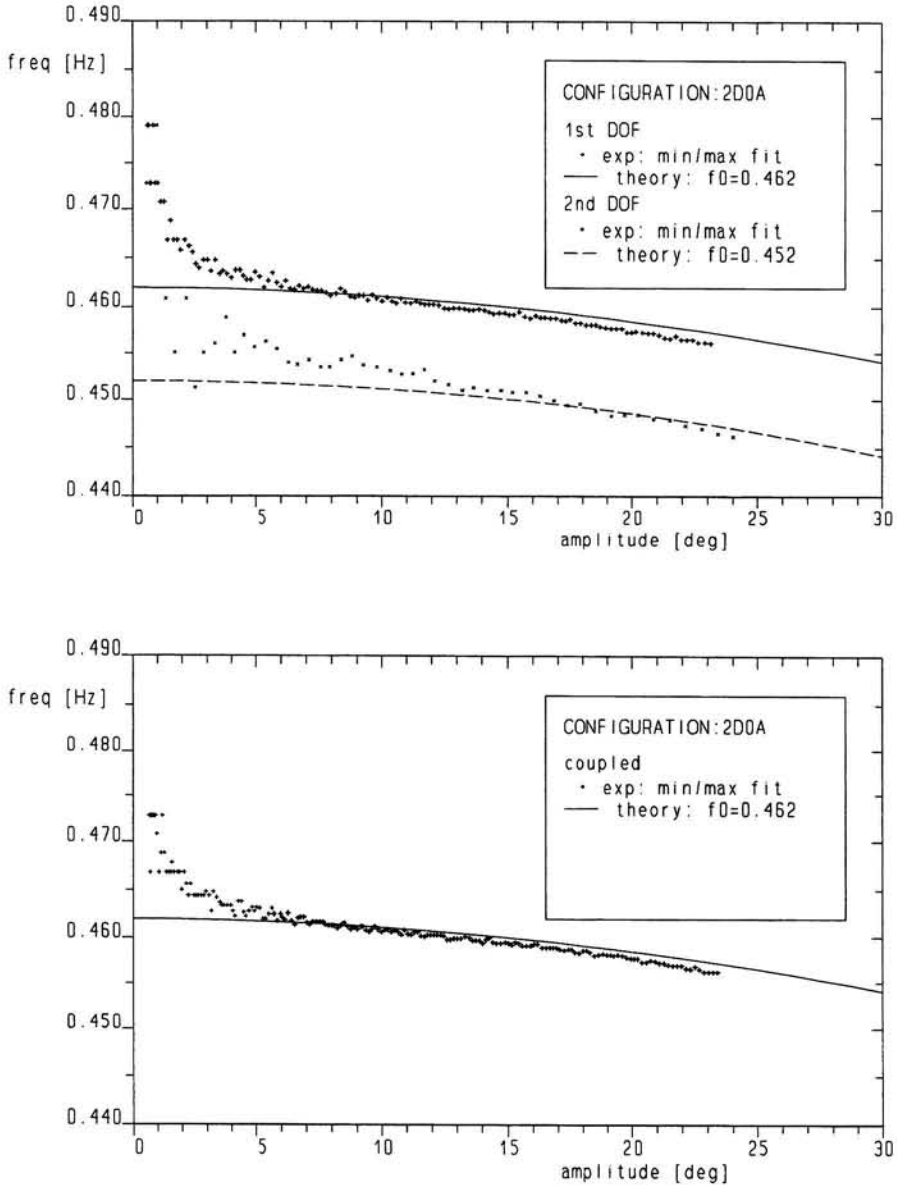

Figure 5a: Free oscillation characteristics (configuration A).

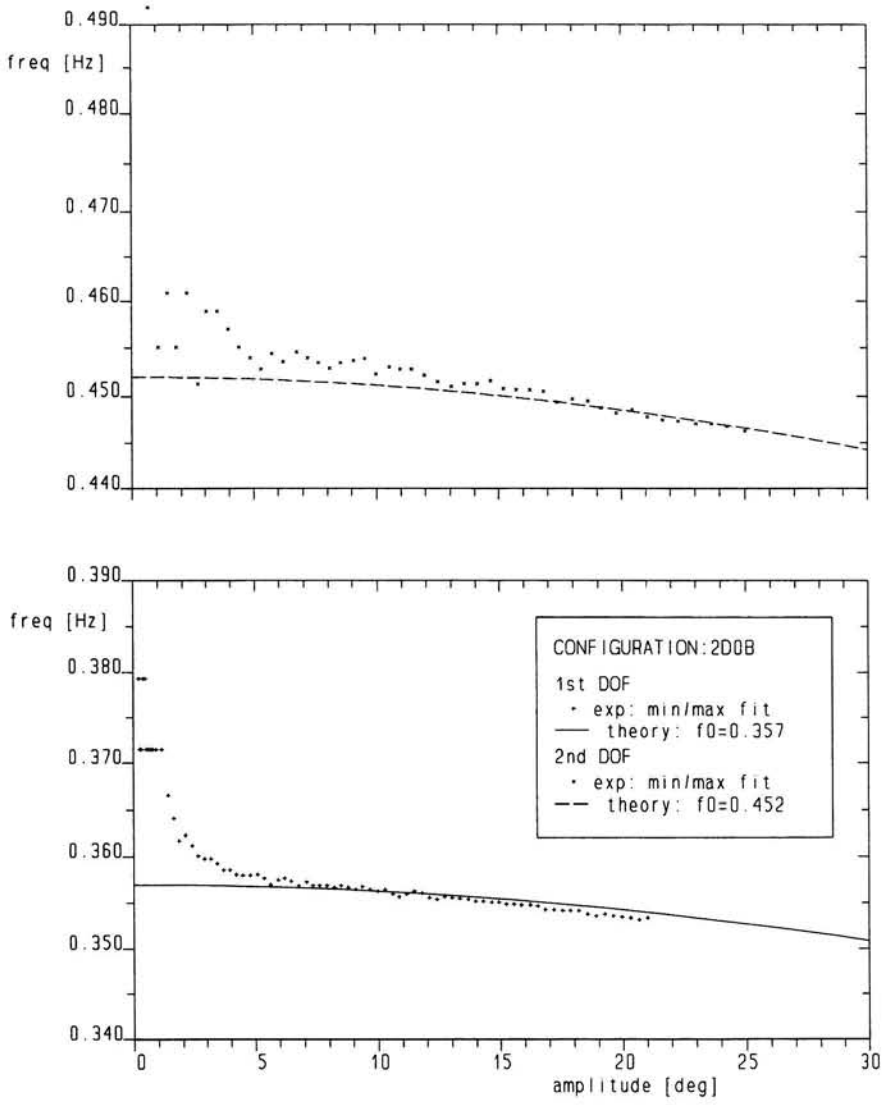

Figure 5b: Free oscillation characteristics (configuration B).

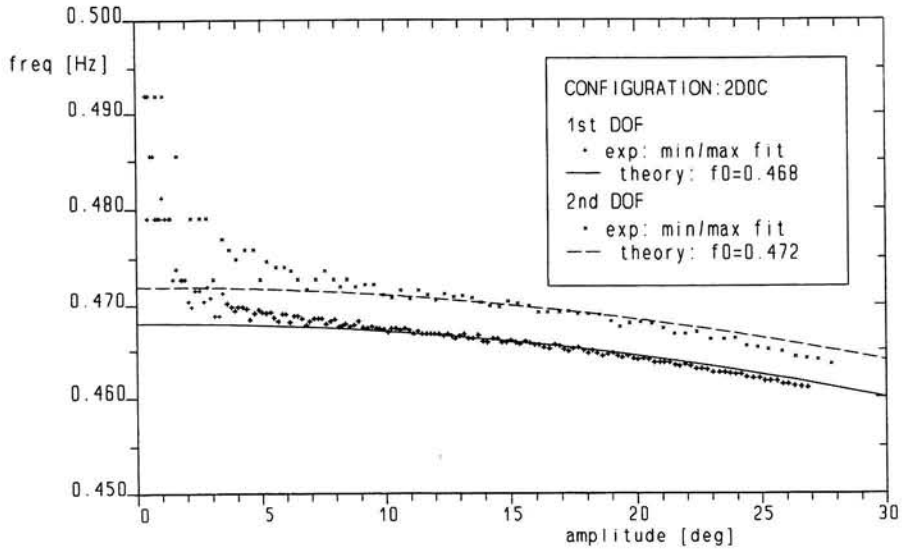

Figure 5c: Free oscillation characteristics (configuration C).

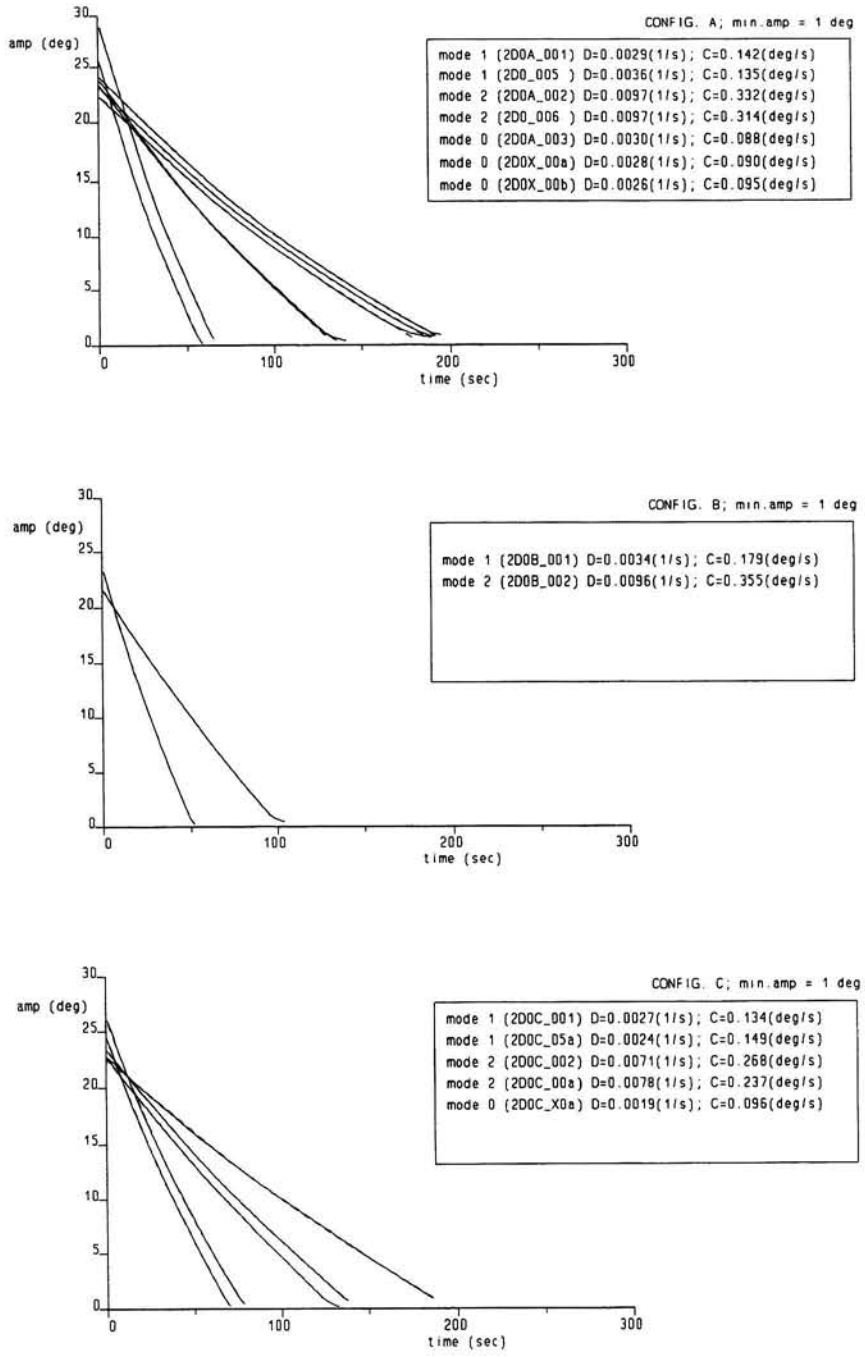

Figure 6: Damping characteristics.

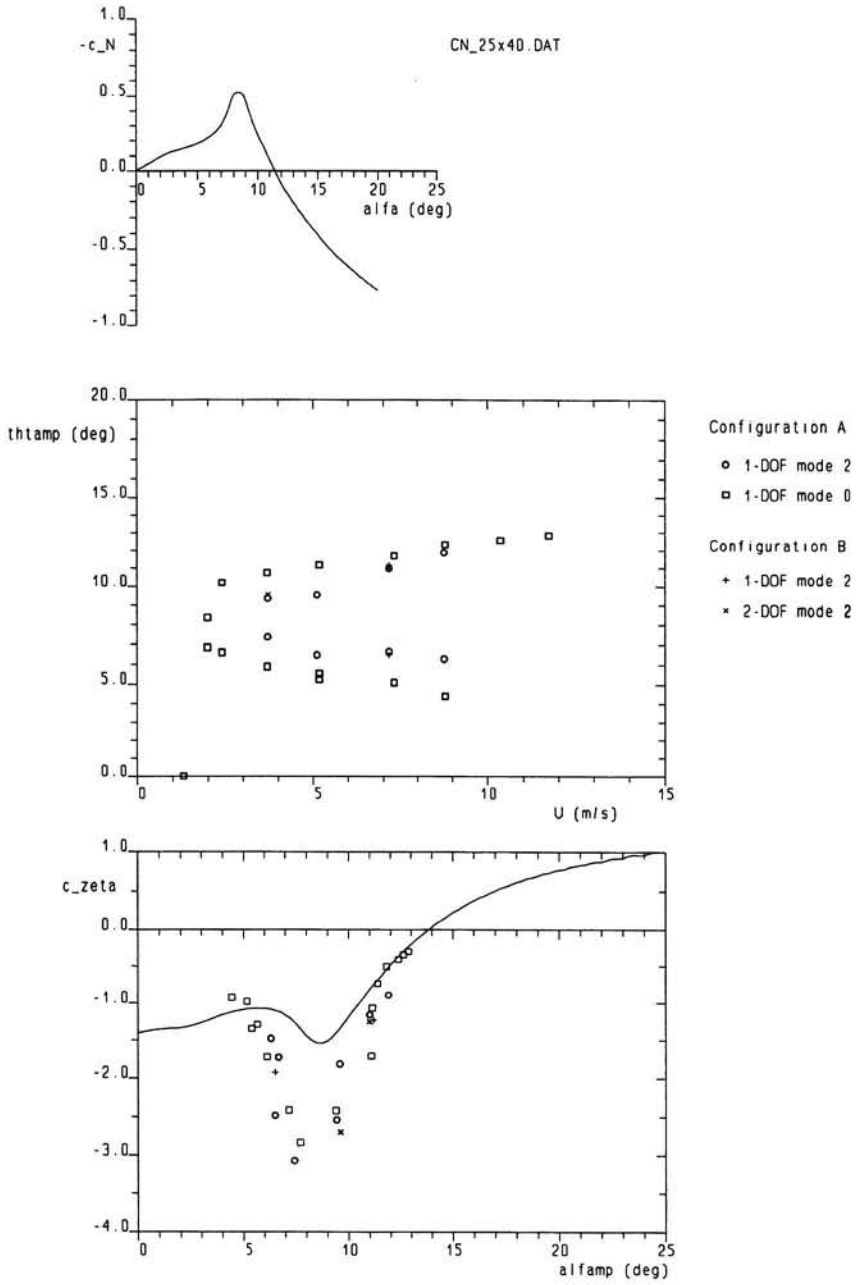

Figure 7a: Single-DOF rotational galloping characteristics for configurations with the 25 mm × 40 mm cross section.

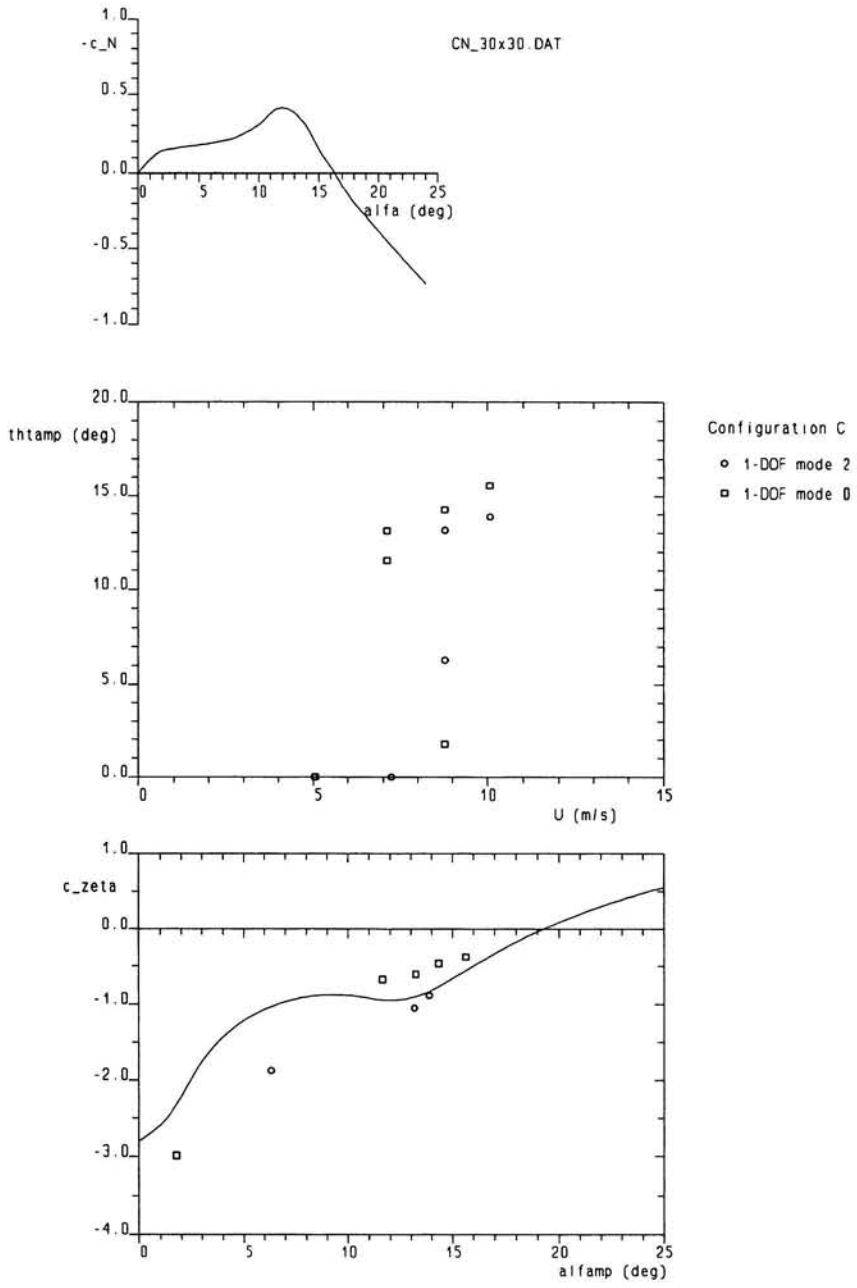

Figure 7b: Single-DOF rotational galloping characteristics for configurations with the 30 mm × 30 mm cross section.

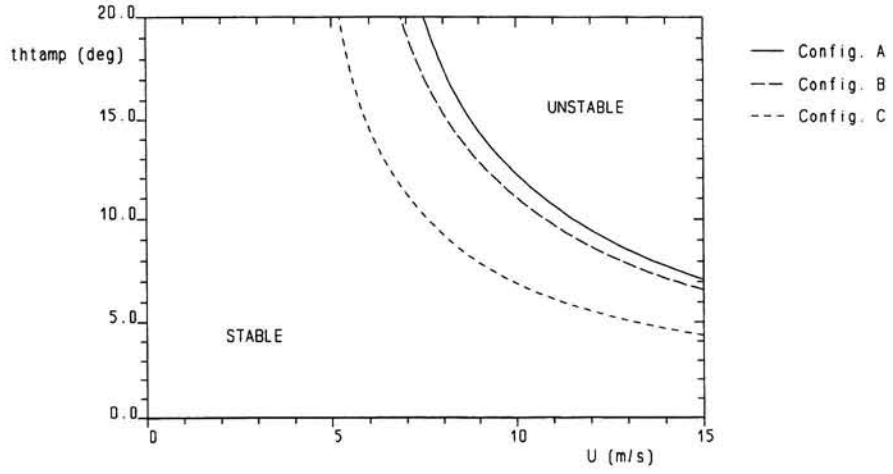

Figure 8: Stability boundaries for single-DOF translational galloping (mode 1).

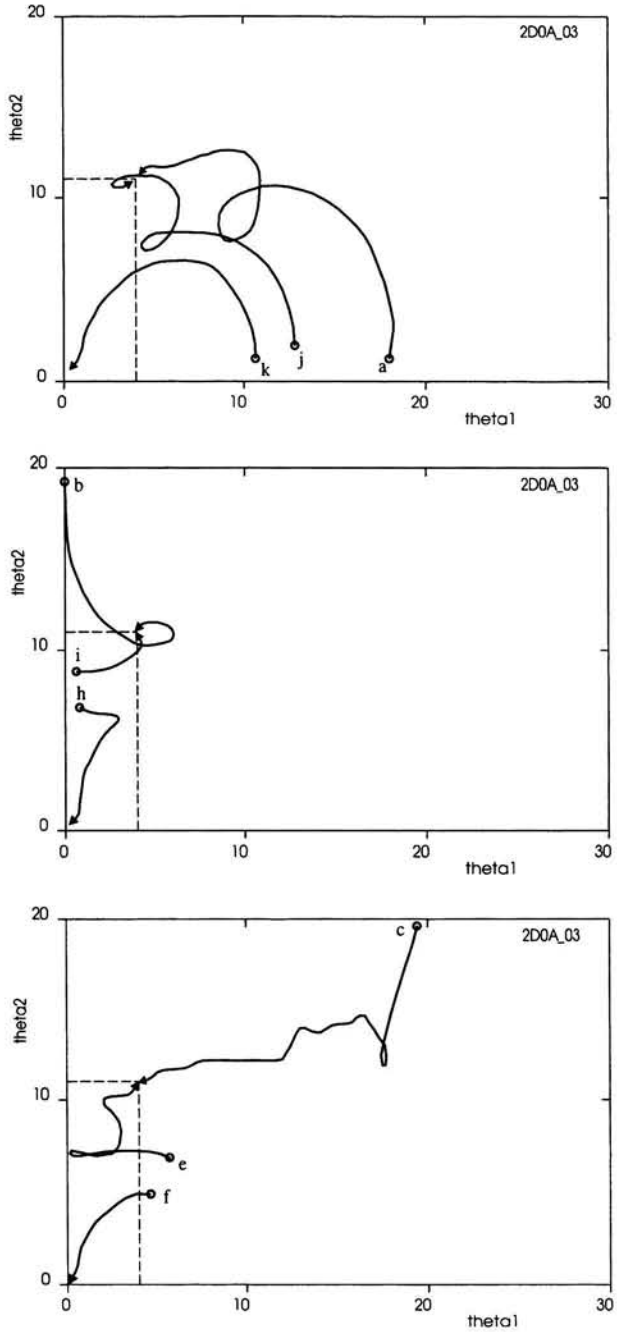

(a) code 2D0A_03: U = 3.7 m/s.

Figure 9: Oscillations in the amplitude-plane (Configuration A).

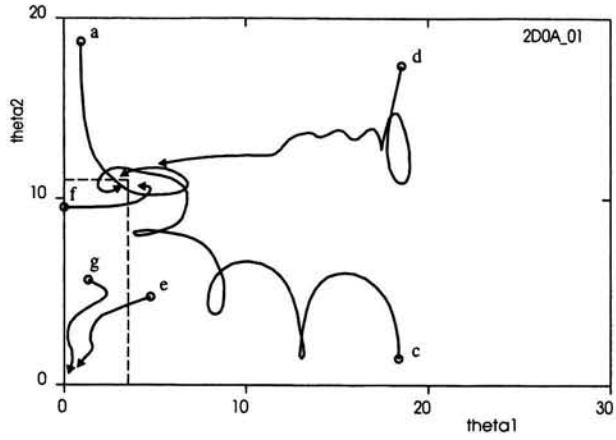

(b) code 2D0A_01: U = 5.1 m/s.

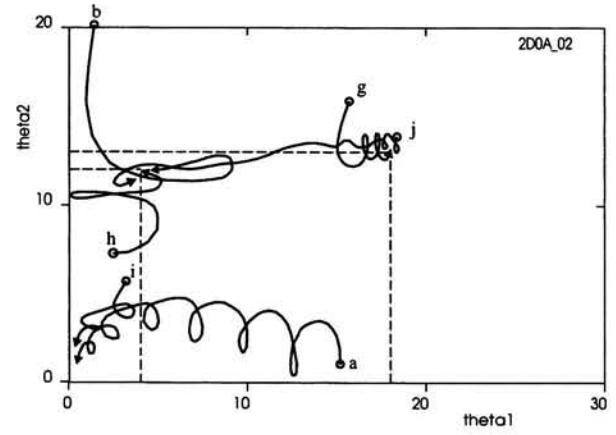

(c) code 2D0A_02: U = 7.2 m/s.

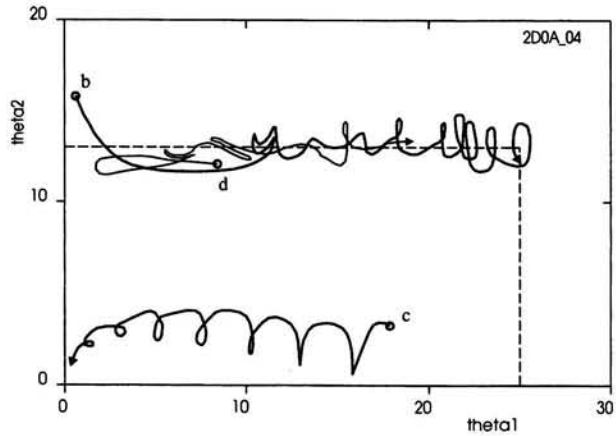

(d) code 2D0A_04: U = 8.8 m/s.

Figure 9 (continued): Oscillations in the amplitude-plane (Configuration A).

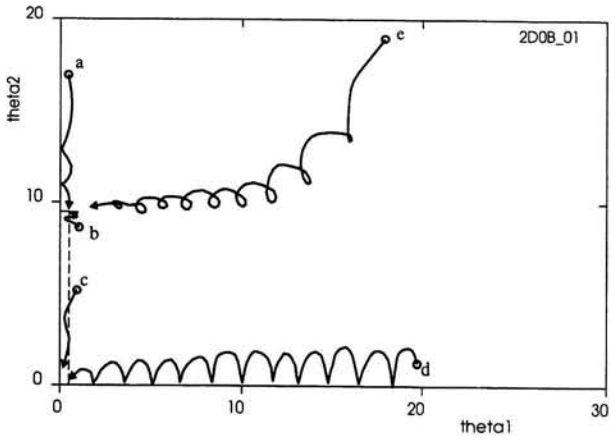

(a) code 2D0B_01: U = 3.7 m/s.

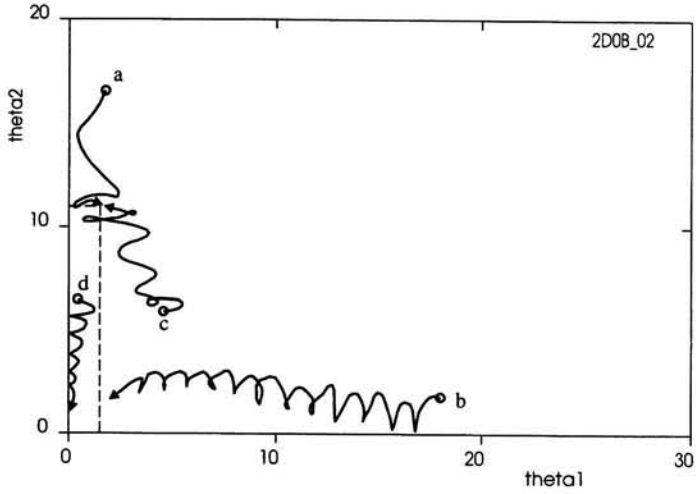

(b) code 2D0B_02: U = 7.2 m/s.

Figure 10: Oscillations in the amplitude-plane (Configuration B).

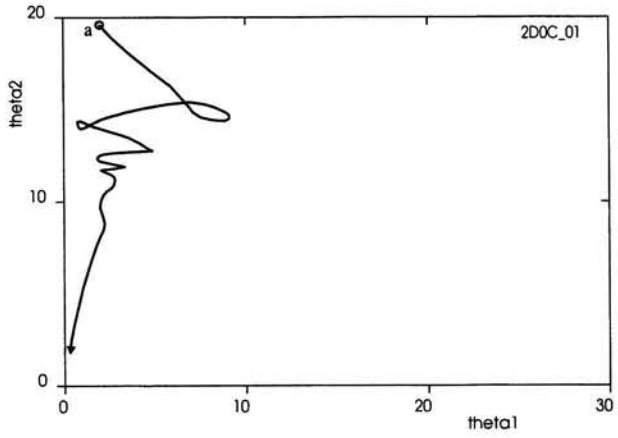

(a) code 2D0C_01: U = 5.0 m/s.

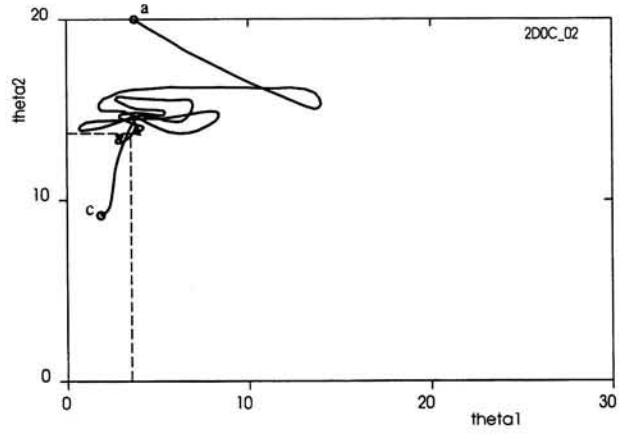

(b) code 2D0C_02: U = 7.1 m/s.

Figure 11: Oscillations in the amplitude-plane (Configuration C).

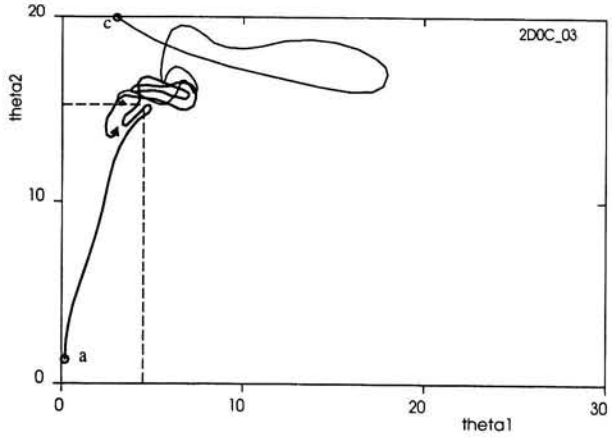

(c) code 2D0C_03: U = 8.8 m/s.

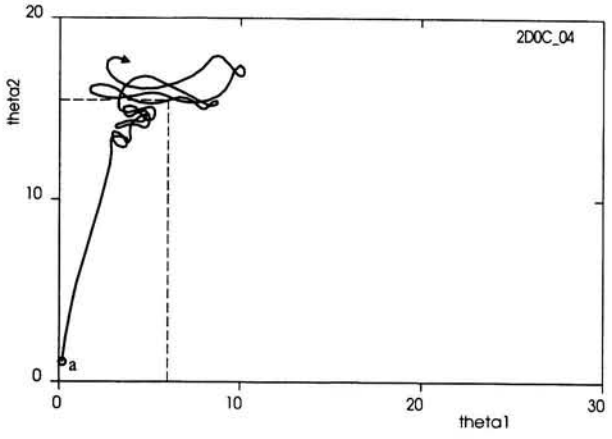

(d) code 2D0C_04: U = 10.3 m/s.

Figure 11 (continued): Oscillations in the amplitude-plane (Configuration C).

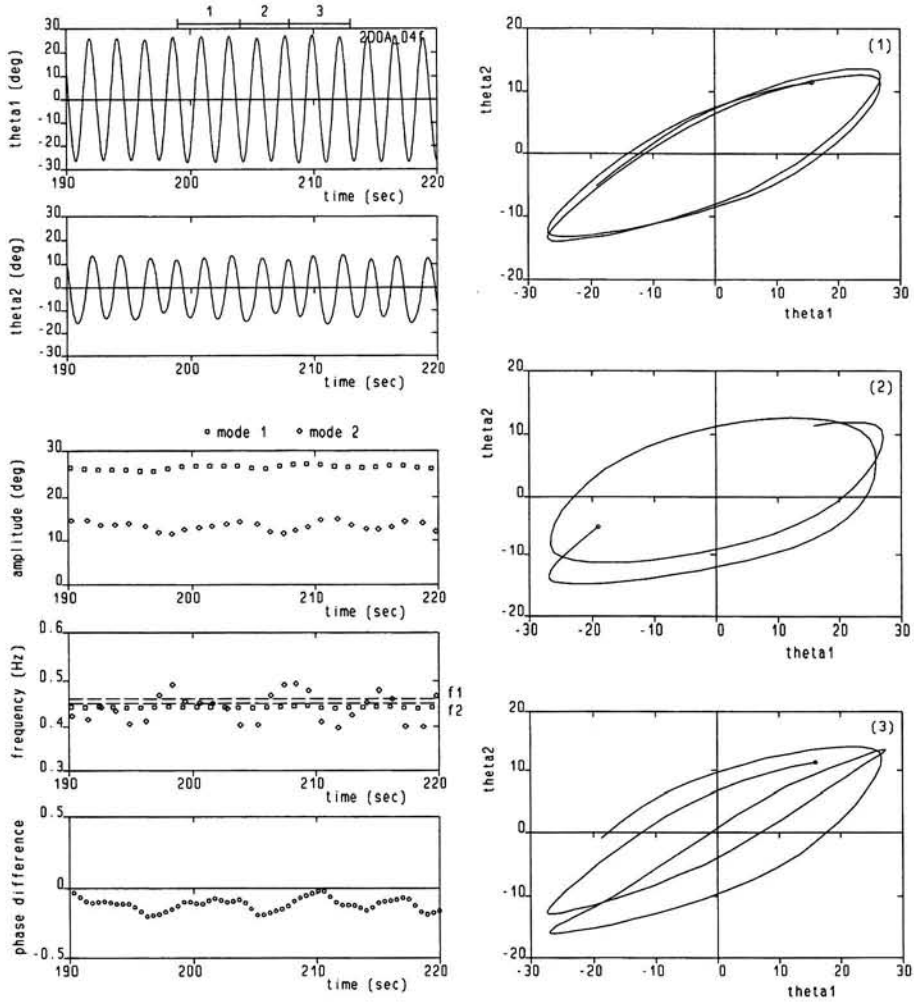

Figure 12: Oscillation record (detail) showing unsteadiness of limit cycle.

Appendix. Oscillation records

This Appendix contains an extensive description of the individual oscillation tests, both free and under wind load conditions, in the form of a set of figures that present time records of both oscillation modes, as well as derived data such as instantaneous values of the mode frequencies and amplitudes and the phase difference, the latter given as $(\phi_2-\phi_1)/2\pi$ on the interval (-0.5,0.5). In addition to the separate time records of both modes, the oscillation is further represented in the form of Lissajous graphs on the right hand side of the figure, with the start of the run indicated by a small circle. For the free oscillation tests a single Lissajous graph is given that depicts the entire time record. For clarity for the tests with wind loading only selected intervals are considered, where the number in brackets in the top right corner of each Lissajous plot corresponds to the time interval indicated at the top of the first time record. At the upper right corner of this record the run code is given, which identifies the configuration and experimental conditions according to the index given below:

prefix	configuration	series	runs	wind speed (m/s)	air density (kg/m^3)
2D0	A	00	a-c	0	
		01	a-h	5.10	1.179
		02	a-j	7.16	1.179
		03	a-k	3.72	1.174
		04	a-f	8.78	1.175
	B	00	a-c	0	
		01	a-f	3.72	1.174
		02	a-h	7.17	1.174
	C	00	a-h	0	
		01	a	5.04	1.166
		02	a-c	7.13	1.166
		03	a-d	8.81	1.166
		04	a-b	10.29	1.166

The 0 in the prefix was used to indicate, in correspondence with the notation used in previous experiments [5], that no additional (inductive) system damping was applied([1]). For reference purpose in the main text to test conditions and individual runs, and for the figure numbering in this Appendix, use is made of abbreviated codes for convenience: for example, A1b corresponds to the full run code 2D0A_**01b**.

[1] Note, however, that the configuration codes A, B and C used here have no relation to those of the 1-DOF configurations [5].

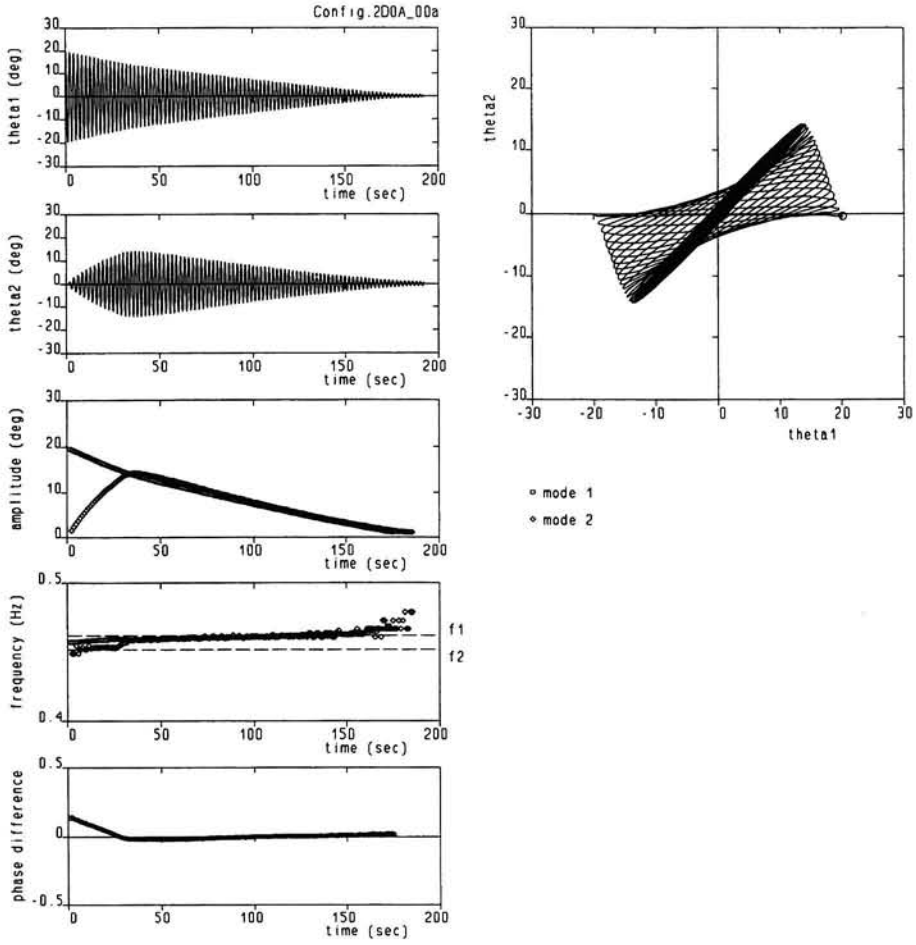
Config.2D0A_00a
theta1 (deg)
theta2 (deg)
amplitude (deg)
frequency (Hz)
f1
f2
phase difference
time (sec)
theta2
theta1
mode 1
mode 2

Figure A0a.

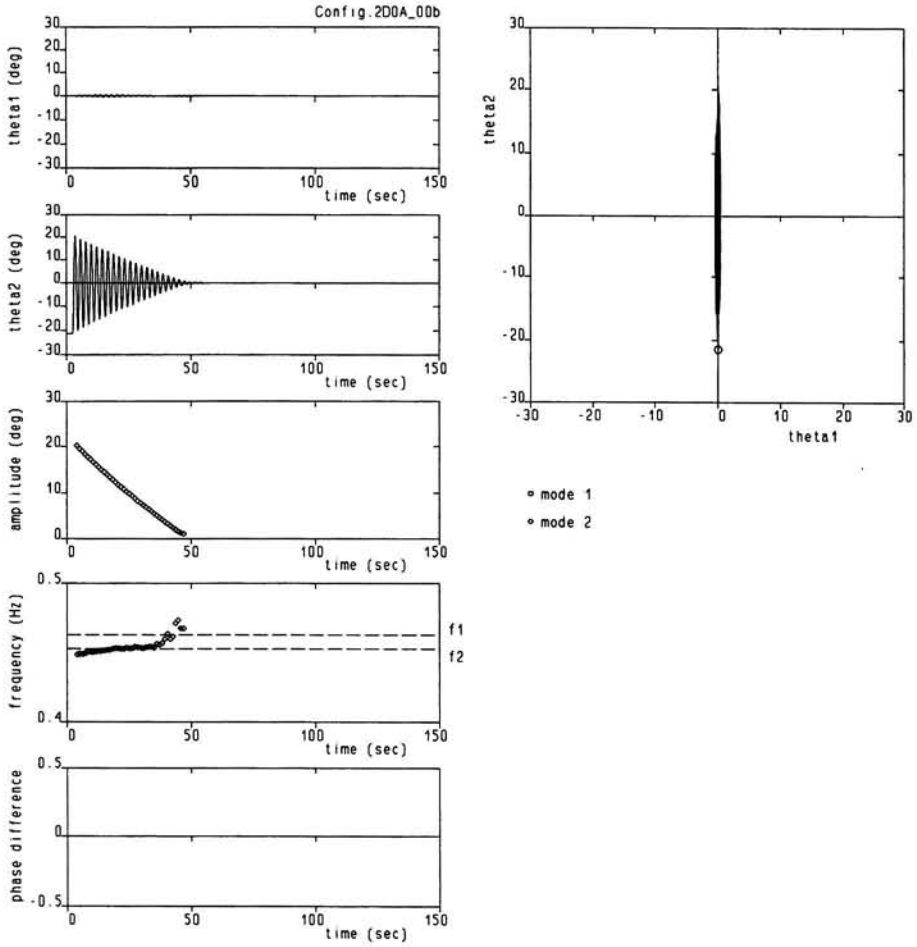
Config.2D0A_00b
theta1 (deg)
theta2 (deg)
amplitude (deg)
frequency (Hz)
phase difference
time (sec)
f1
f2
theta2
theta1
mode 1
mode 2

Figure A0b.

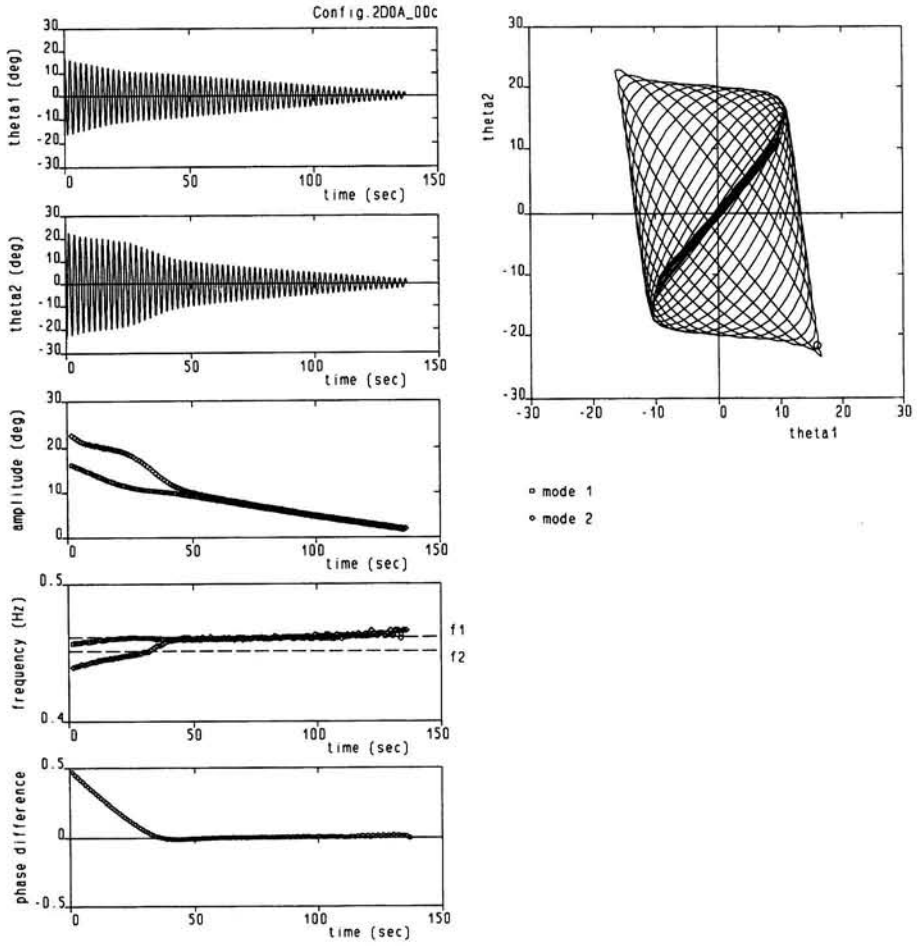
Config.2D0A_00c
theta1 (deg)
theta2 (deg)
amplitude (deg)
frequency (Hz)
f1
f2
phase difference
time (sec)
theta2
theta1
mode 1
mode 2

Figure A0c.

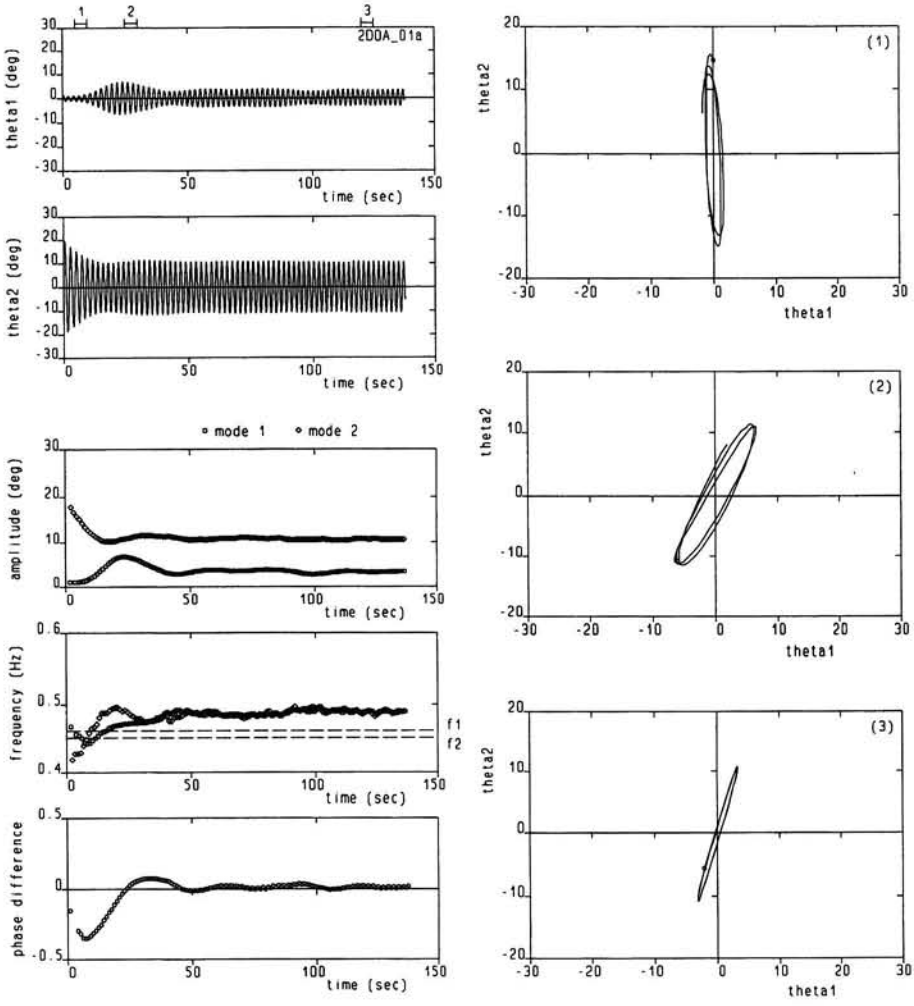
1
2
3
2DOA_01a
theta1 (deg)
theta2 (deg)
time (sec)
mode 1
mode 2
amplitude (deg)
frequency (Hz)
f1
f2
phase difference
theta2
theta1
(1)
(2)
(3)

Figure A1a.

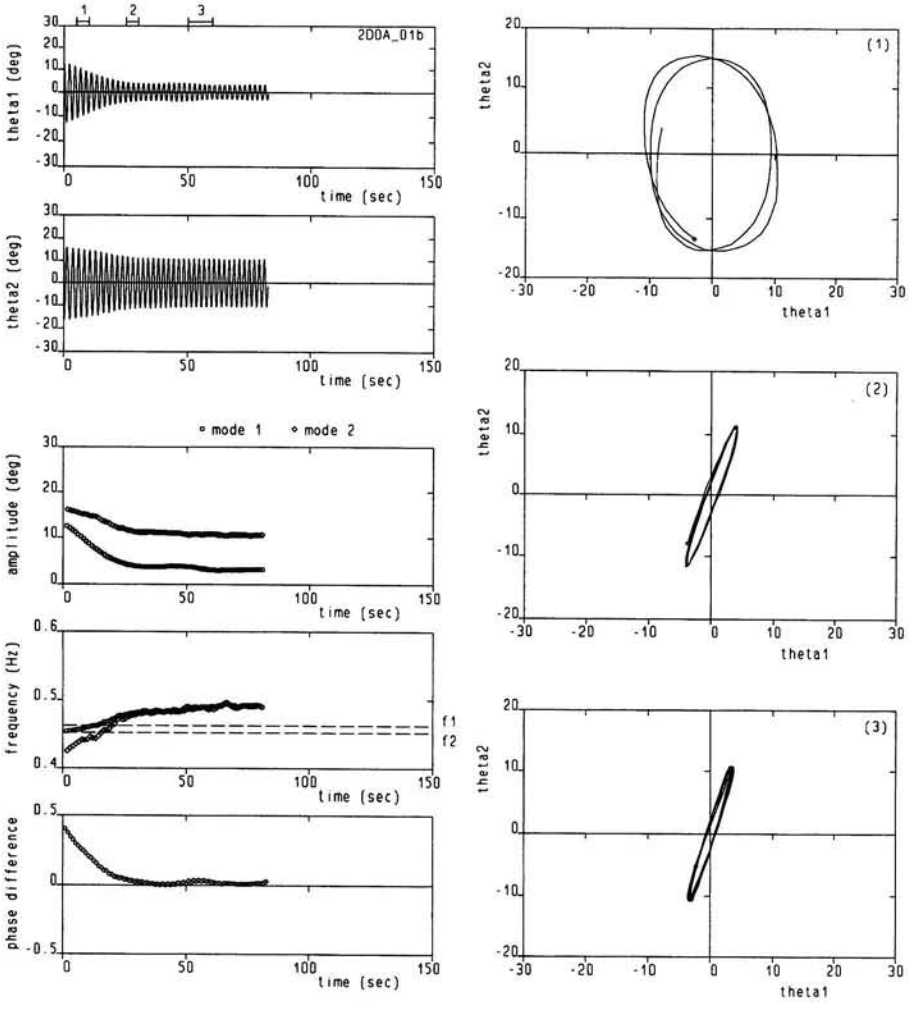
1
2
3
2D0A_01b
theta1 (deg)
theta2 (deg)
time (sec)
mode 1
mode 2
amplitude (deg)
frequency (Hz)
f1
f2
phase difference
theta2
theta1
(1)
(2)
(3)

Figure A1b.

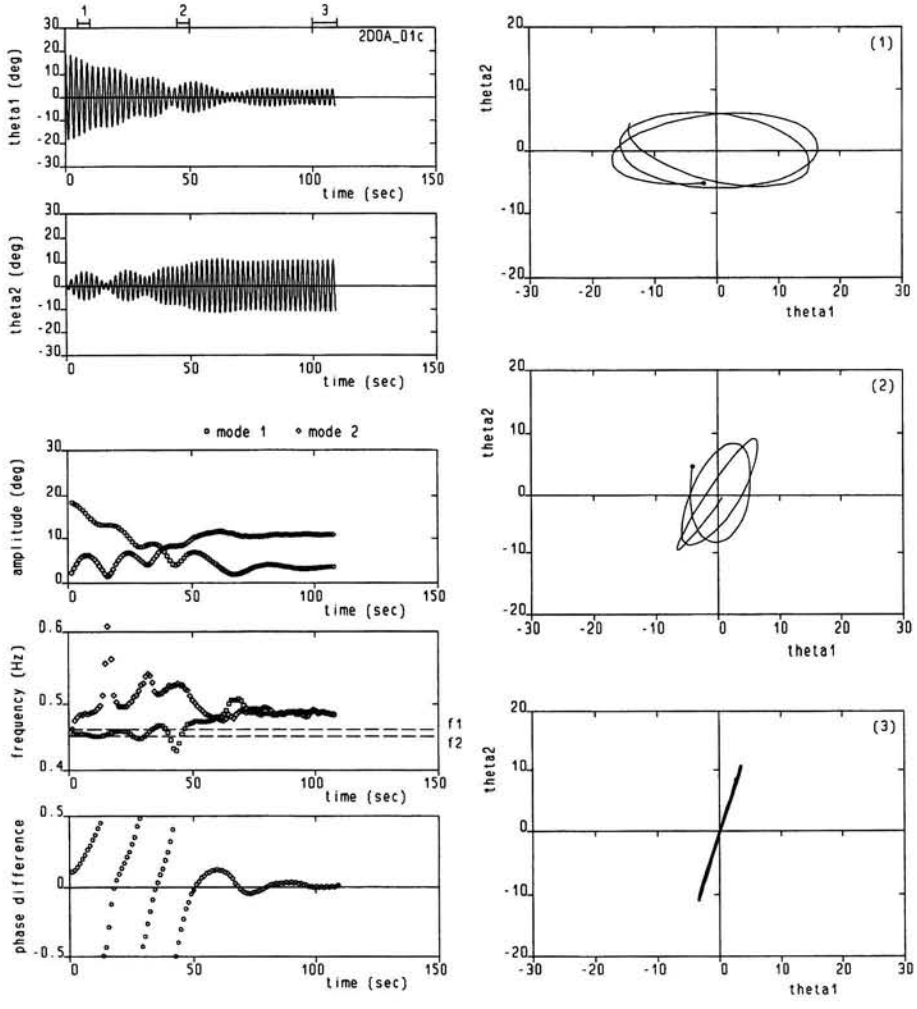
1
2
3
2D0A_01c
theta1 (deg)
time (sec)
theta2 (deg)
time (sec)
mode 1
mode 2
amplitude (deg)
time (sec)
frequency (Hz)
f1
f2
time (sec)
phase difference
time (sec)
(1)
theta2
theta1
(2)
theta2
theta1
(3)
theta2
theta1

Figure A1c.

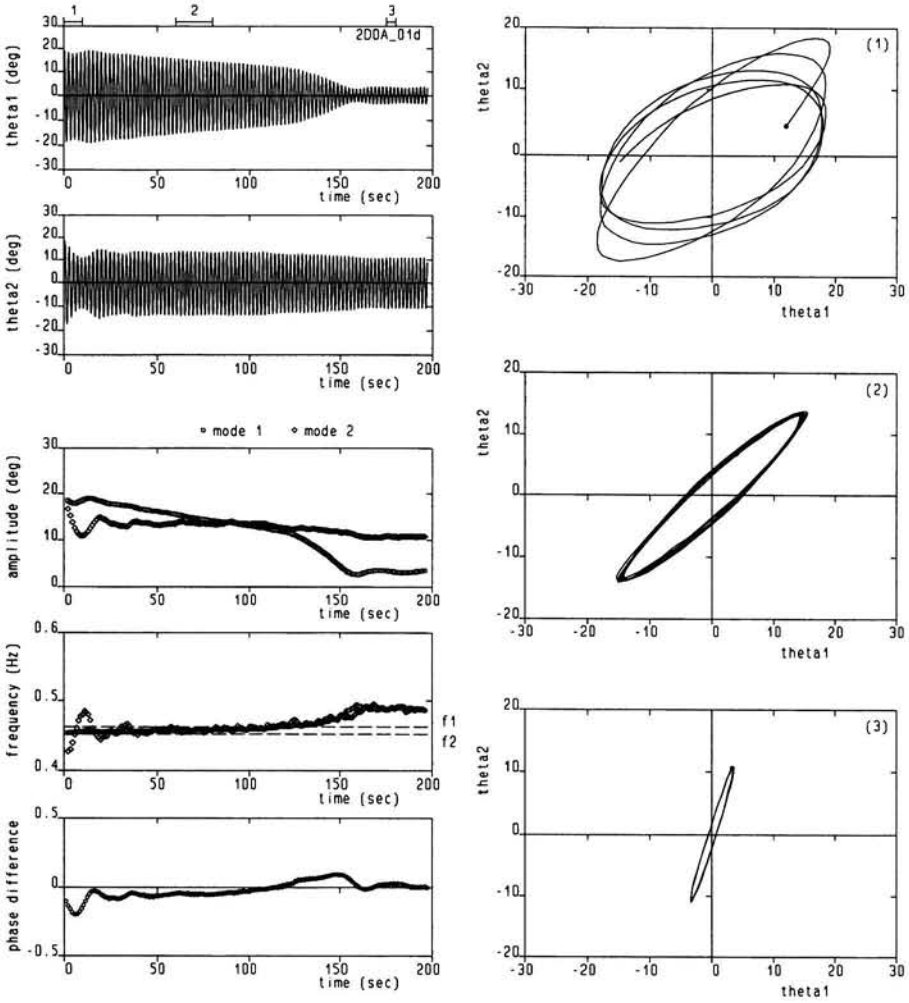
1
2
3
2D0A_01d
theta1 (deg)
theta2 (deg)
time (sec)
mode 1
mode 2
amplitude (deg)
frequency (Hz)
f1
f2
phase difference
(1)
(2)
(3)
theta1
theta2

Figure A1d.

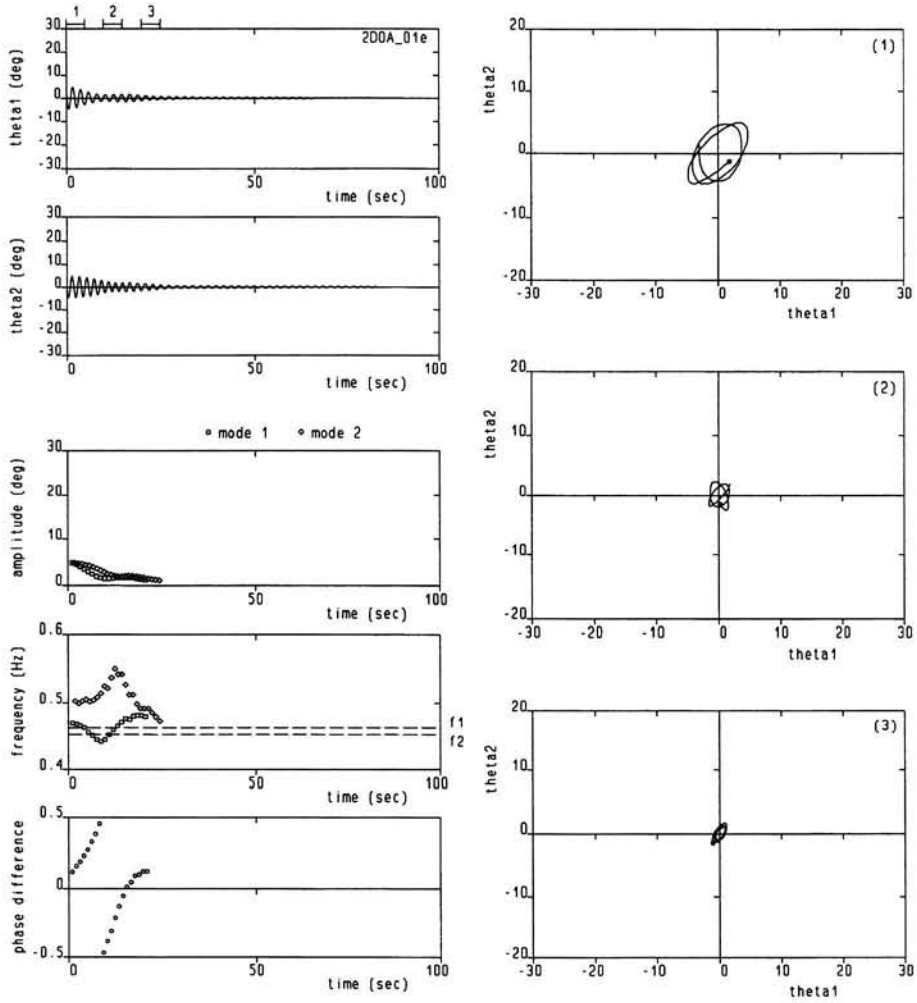
1
2
3
2D0A_01e
theta1 (deg)
time (sec)
theta2 (deg)
time (sec)
mode 1
mode 2
amplitude (deg)
time (sec)
frequency (Hz)
f1
f2
time (sec)
phase difference
time (sec)
(1)
theta2
theta1
(2)
theta2
theta1
(3)
theta2
theta1

Figure A1e.

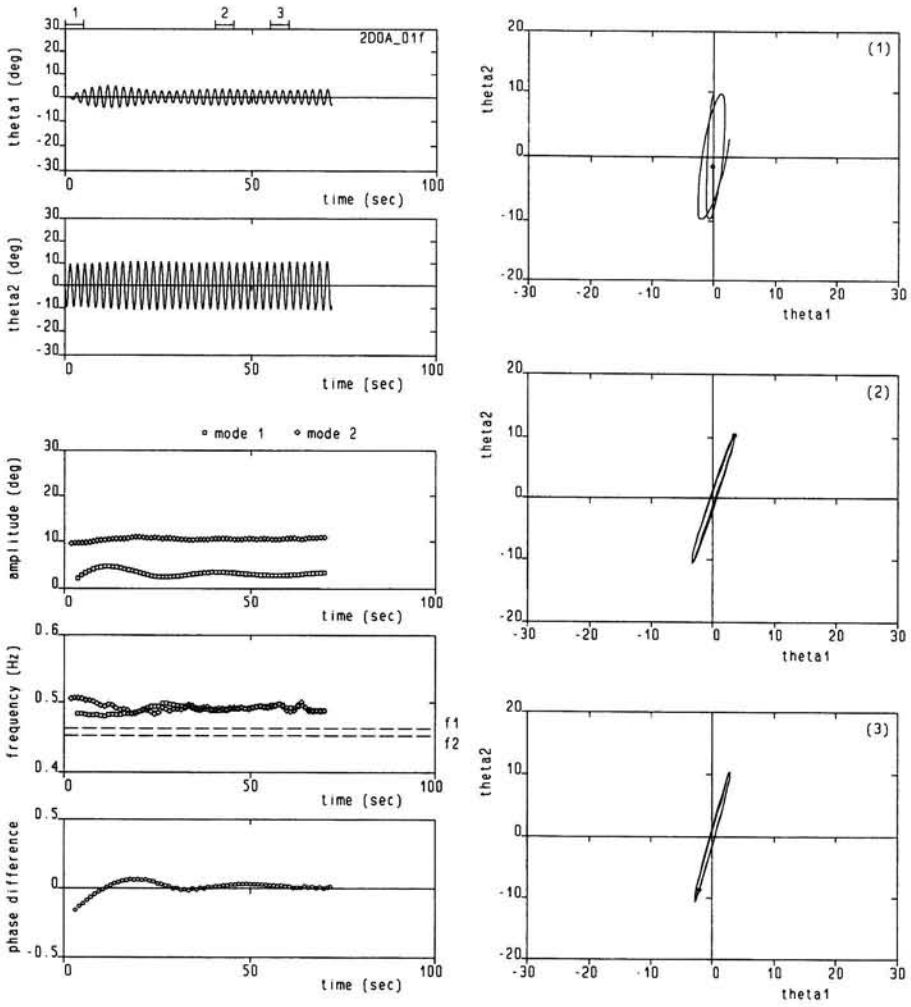
1
2
3
2DOA_01f
theta1 (deg)
time (sec)
theta2 (deg)
time (sec)
mode 1
mode 2
amplitude (deg)
time (sec)
frequency (Hz)
f1
f2
time (sec)
phase difference
time (sec)
(1)
theta2
theta1
(2)
theta2
theta1
(3)
theta2
theta1

Figure A1f.

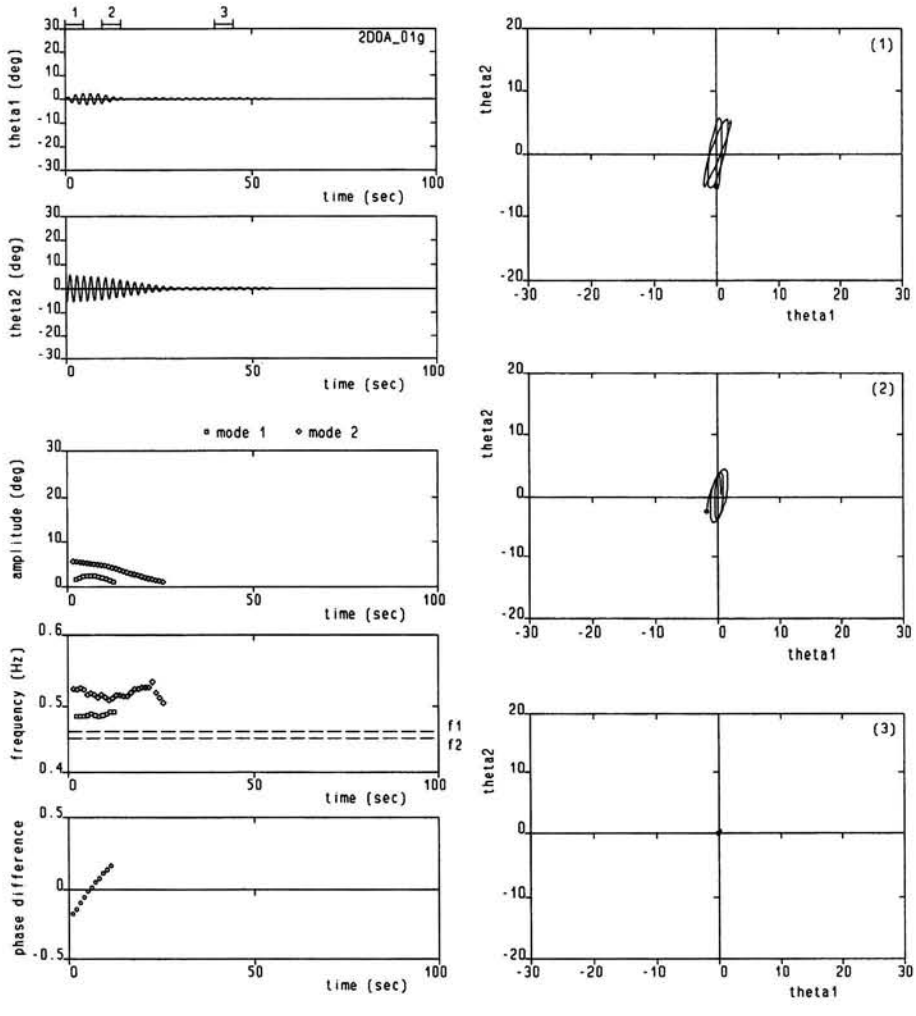
1
2
3
2DOA_01g
theta1 (deg)
time (sec)
theta2 (deg)
mode 1
mode 2
amplitude (deg)
frequency (Hz)
f1
f2
phase difference
theta2
theta1
(1)
(2)
(3)

Figure A1g.

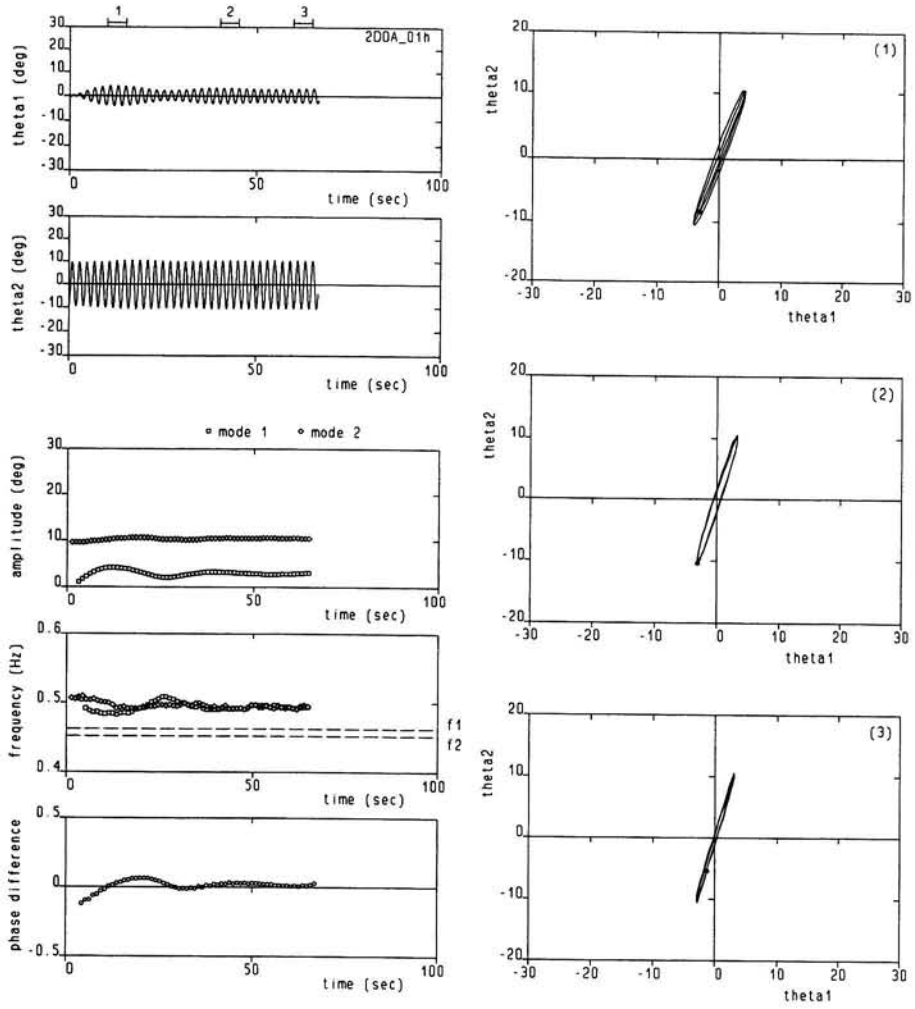
1
2
3
2D0A_01h
theta1 (deg)
time (sec)
theta2 (deg)
time (sec)
mode 1
mode 2
amplitude (deg)
time (sec)
frequency (Hz)
f1
f2
time (sec)
phase difference
time (sec)
(1)
theta2
theta1
(2)
theta2
theta1
(3)
theta2
theta1

Figure A1h.

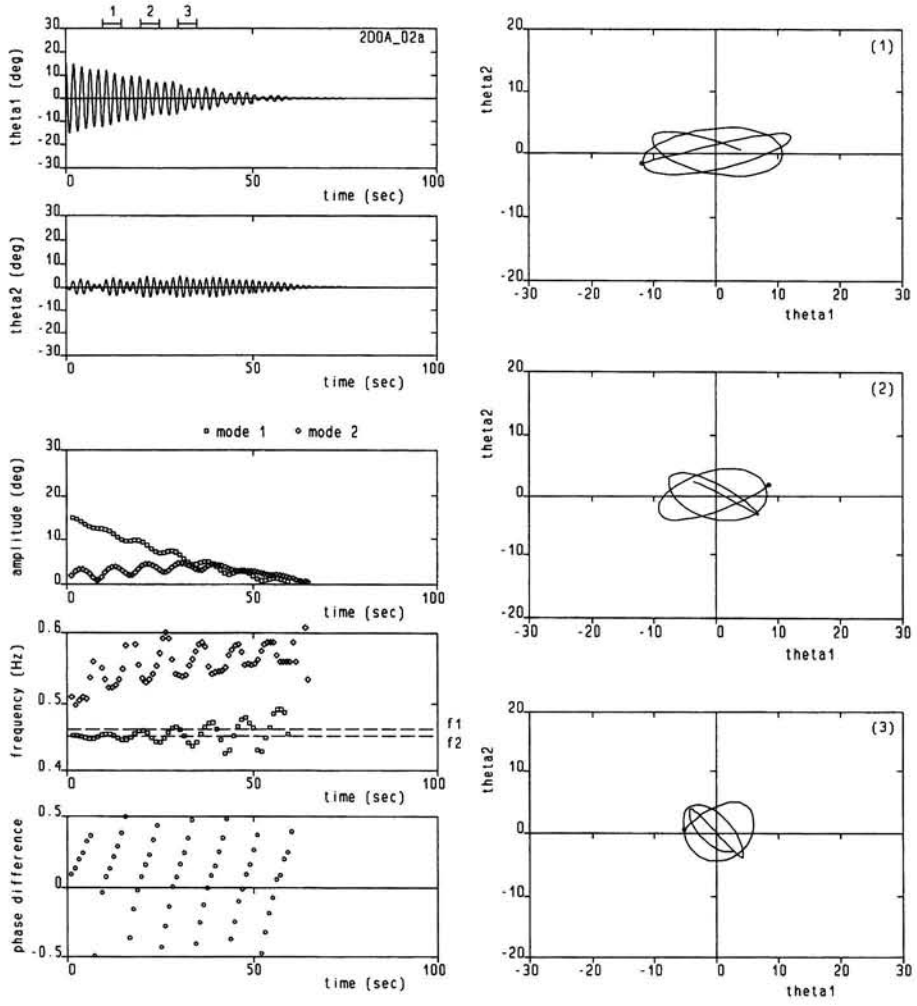
1
2
3
200A_02a
theta1 (deg)
time (sec)
theta2 (deg)
time (sec)
mode 1
mode 2
amplitude (deg)
time (sec)
frequency (Hz)
f1
f2
time (sec)
phase difference
time (sec)
theta2
theta1
(1)
(2)
(3)

Figure A2a.

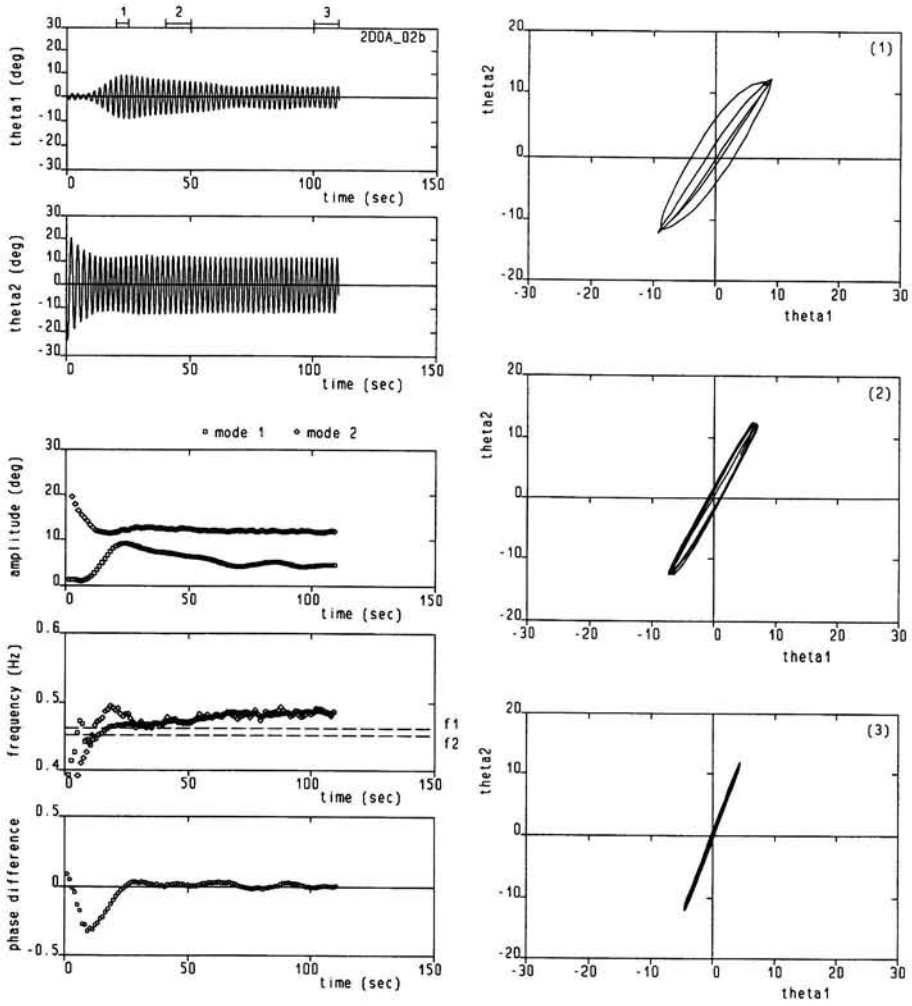
1
2
3
2D0A_02b
theta1 (deg)
time (sec)
theta2 (deg)
time (sec)
mode 1
mode 2
amplitude (deg)
time (sec)
frequency (Hz)
f1
f2
time (sec)
phase difference
time (sec)
(1)
theta2
theta1
(2)
theta2
theta1
(3)
theta2
theta1

Figure A2b.

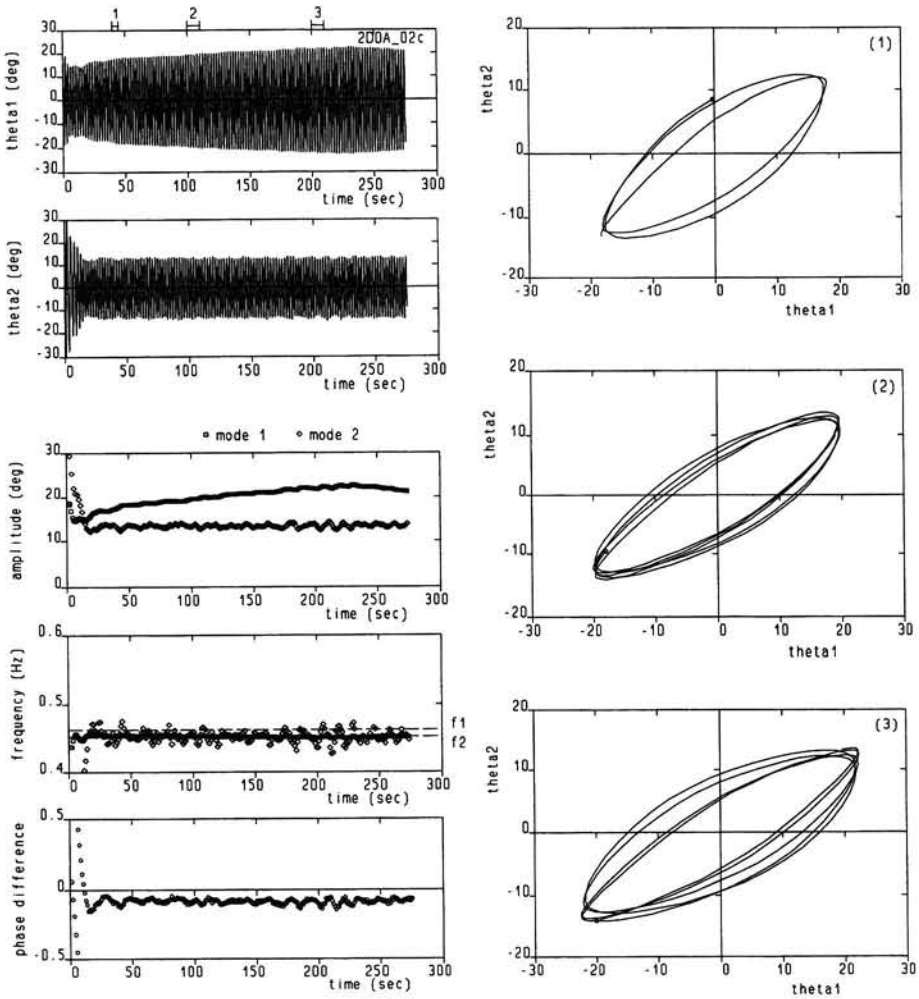
200A_02c
theta1 (deg)
theta2 (deg)
time (sec)
mode 1
mode 2
amplitude (deg)
frequency (Hz)
f1
f2
phase difference
theta2
theta1
(1)
(2)
(3)

Figure A2c.

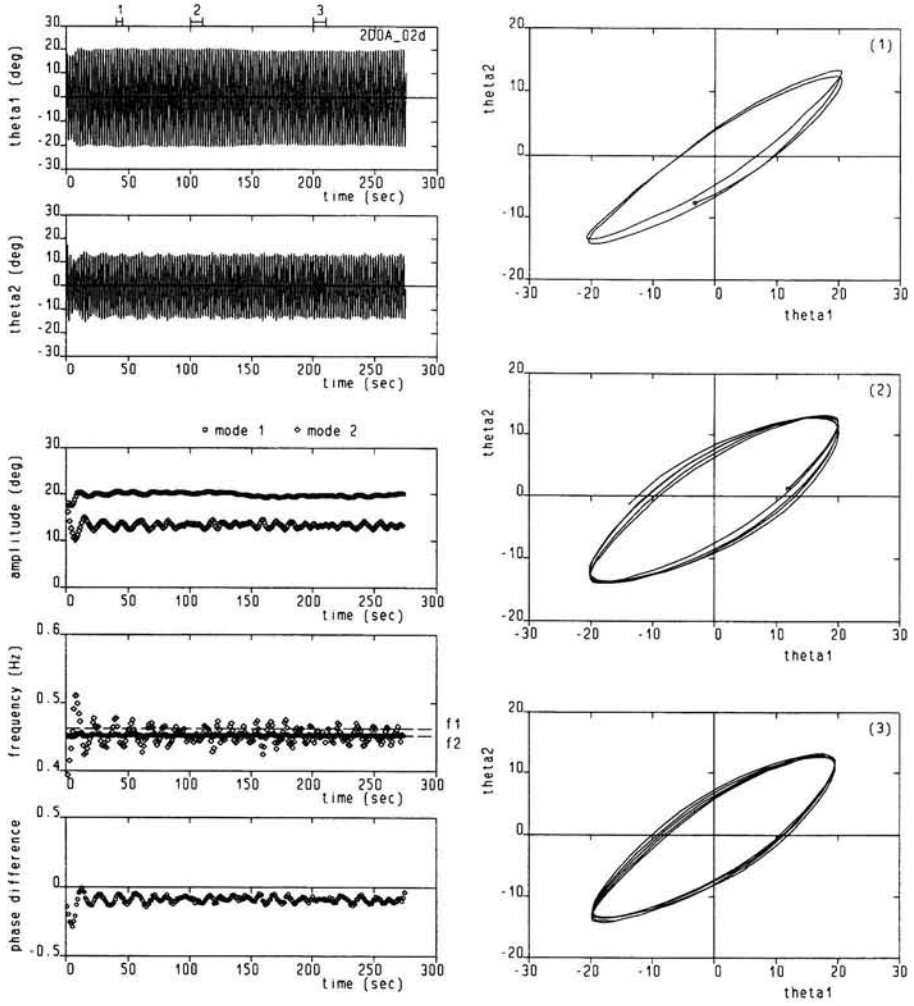
1
2
3
2D0A_02d
theta1 (deg)
theta2 (deg)
time (sec)
mode 1
mode 2
amplitude (deg)
frequency (Hz)
f1
f2
phase difference
theta2
theta1
(1)
(2)
(3)

Figure A2d.

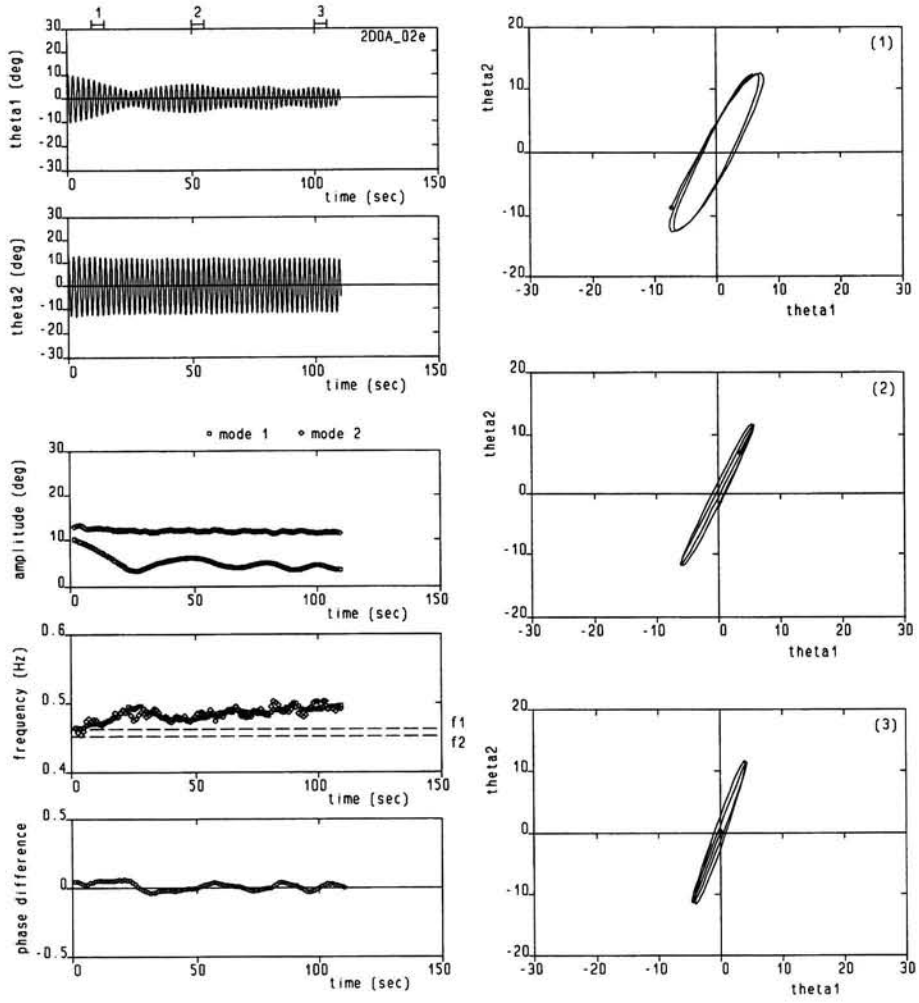
1
2
3
2D0A_02e
theta1 (deg)
theta2 (deg)
time (sec)
mode 1
mode 2
amplitude (deg)
frequency (Hz)
f1
f2
phase difference
(1)
(2)
(3)
theta2
theta1

Figure A2e.

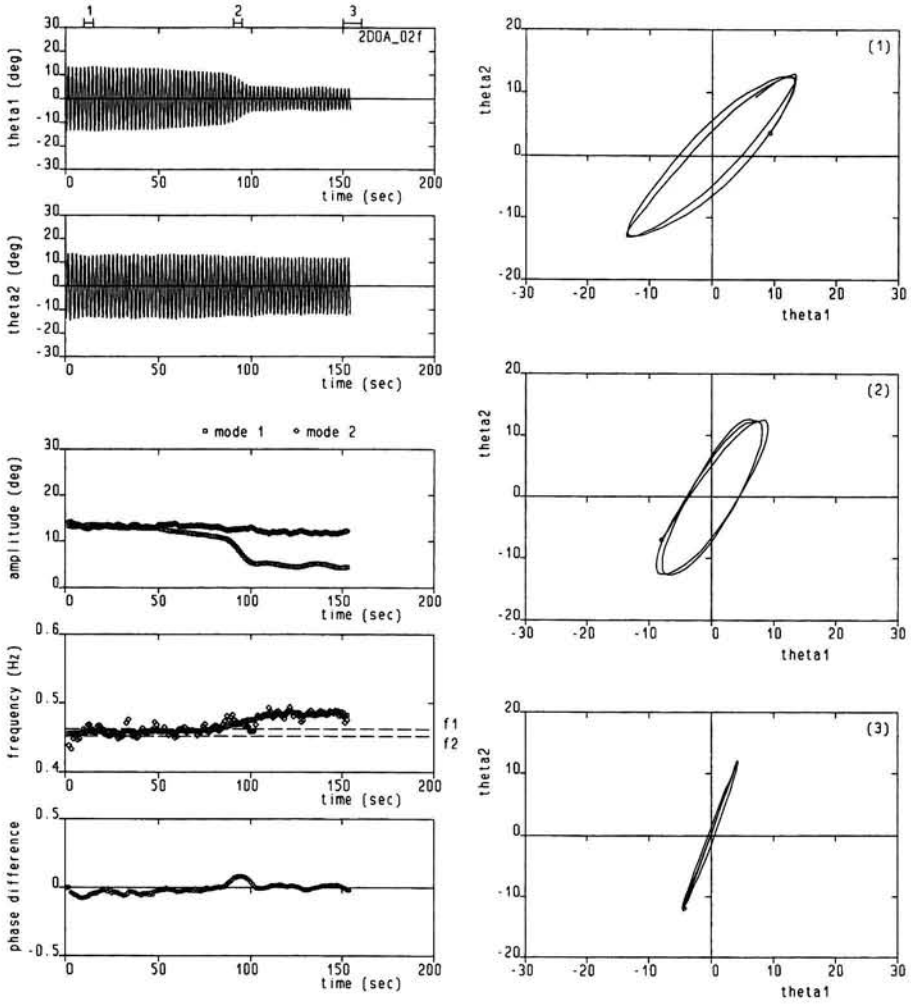
1
2
3
2D0A_02f
theta1 (deg)
theta2 (deg)
time (sec)
mode 1
mode 2
amplitude (deg)
frequency (Hz)
f1
f2
phase difference
theta2
theta1
(1)
(2)
(3)

Figure A2f.

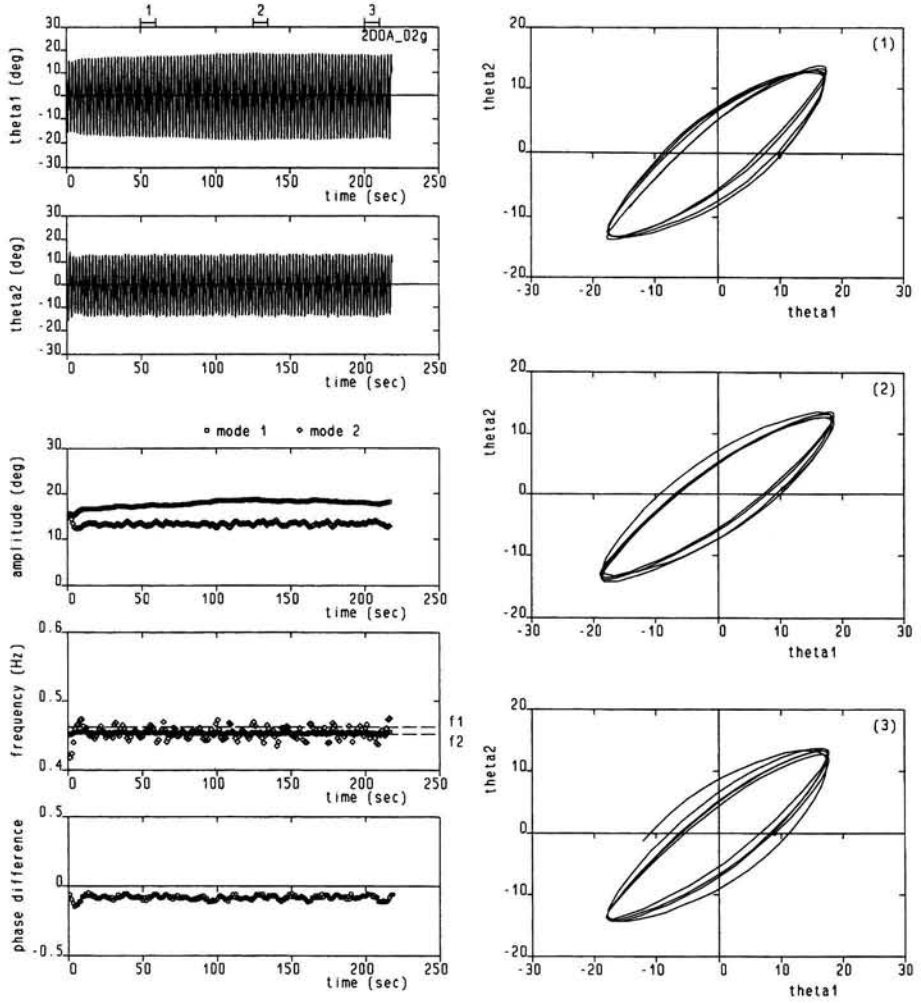
1
2
3
200A_02g
theta1 (deg)
theta2 (deg)
time (sec)
mode 1
mode 2
amplitude (deg)
frequency (Hz)
f1
f2
phase difference
(1)
(2)
(3)
theta2
theta1

Figure A2g.

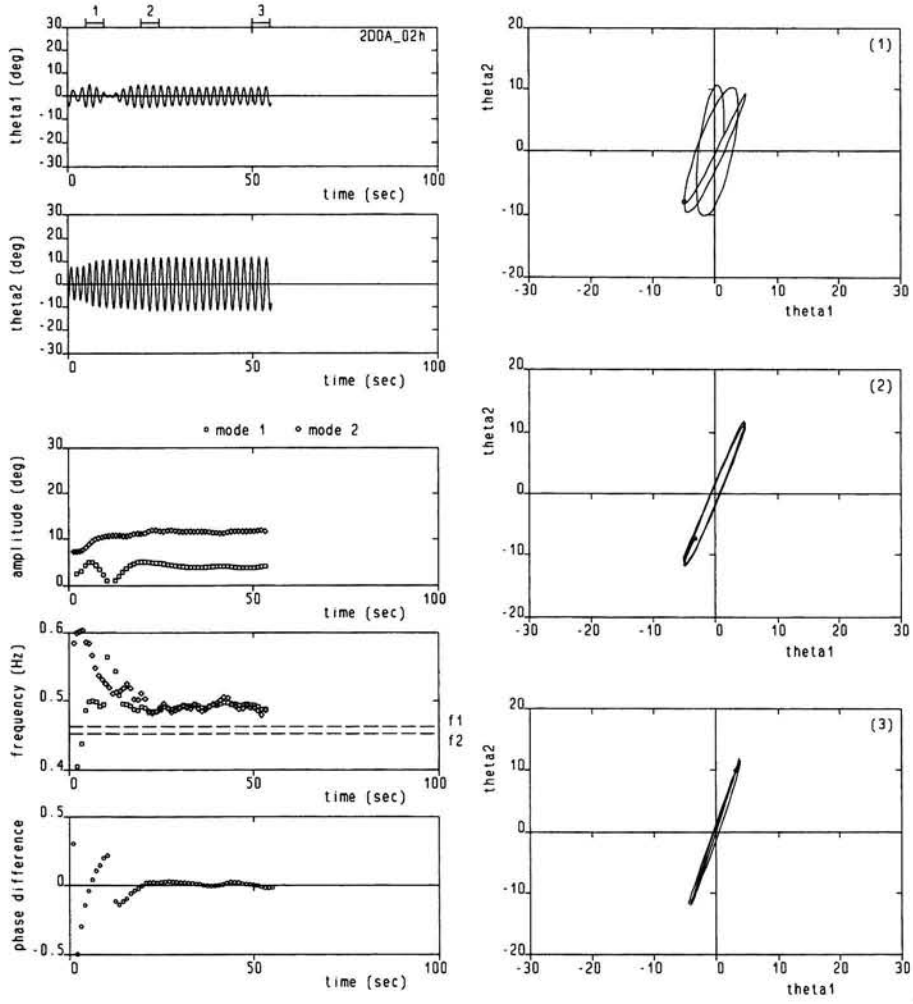
1
2
3
2D0A_02h
theta1 (deg)
time (sec)
theta2 (deg)
time (sec)
mode 1
mode 2
amplitude (deg)
time (sec)
frequency (Hz)
f1
f2
time (sec)
phase difference
time (sec)
(1)
theta2
theta1
(2)
theta2
theta1
(3)
theta2
theta1

Figure A2h.

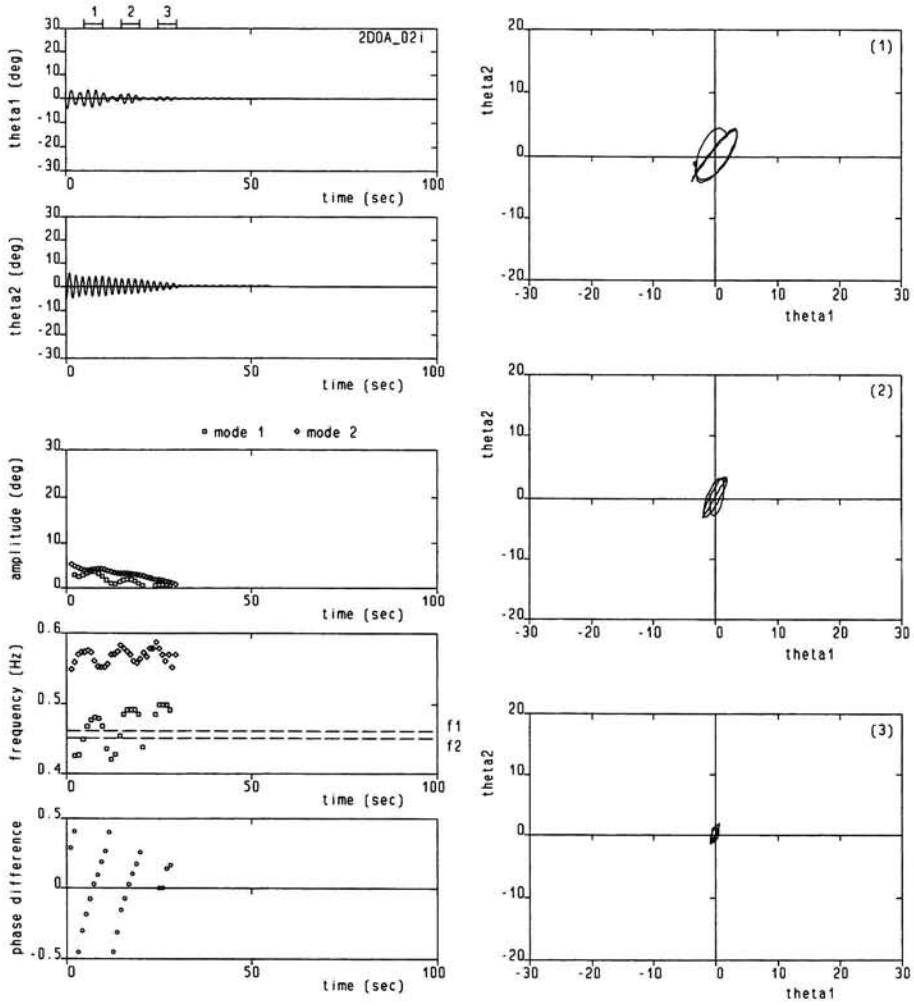
1
2
3
2DOA_02i
theta1 (deg)
theta2 (deg)
time (sec)
mode 1
mode 2
amplitude (deg)
frequency (Hz)
f1
f2
phase difference
theta2
theta1
(1)
(2)
(3)

Figure A2i.

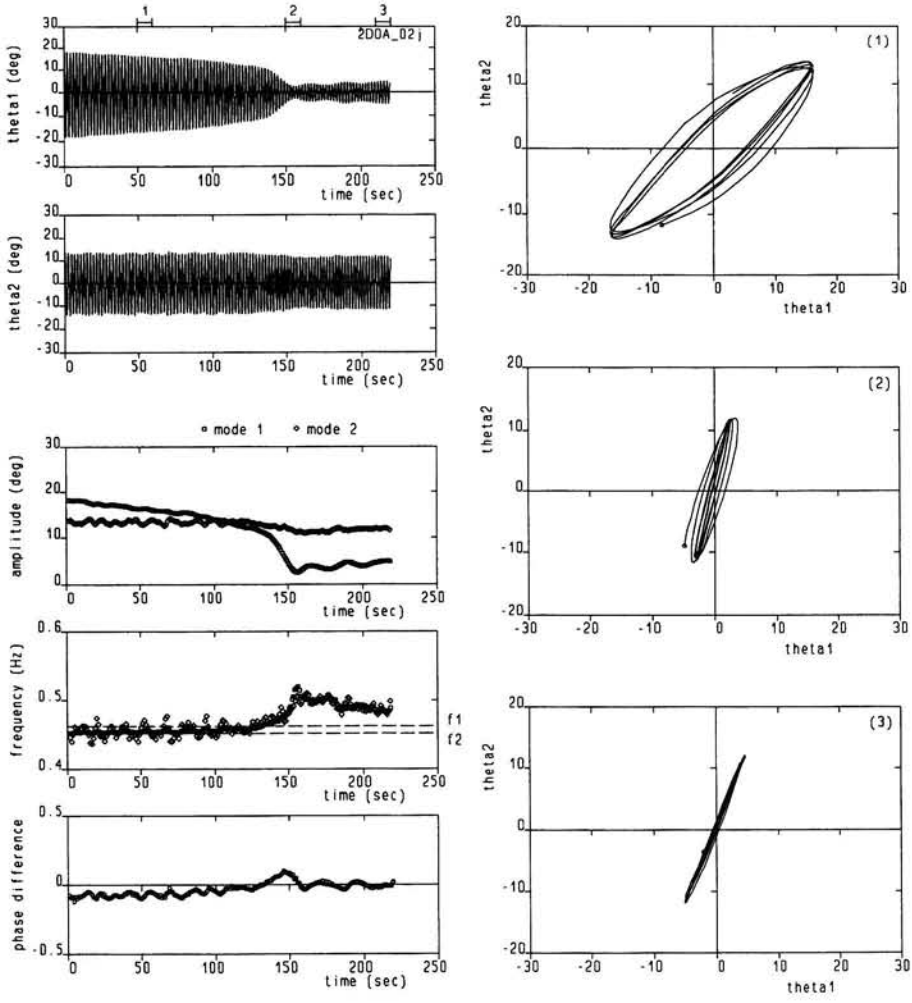
1
2
3
2DOA_02j
theta1 (deg)
theta2 (deg)
time (sec)
mode 1
mode 2
amplitude (deg)
frequency (Hz)
f1
f2
phase difference
(1)
(2)
(3)
theta2
theta1

Figure A2j.

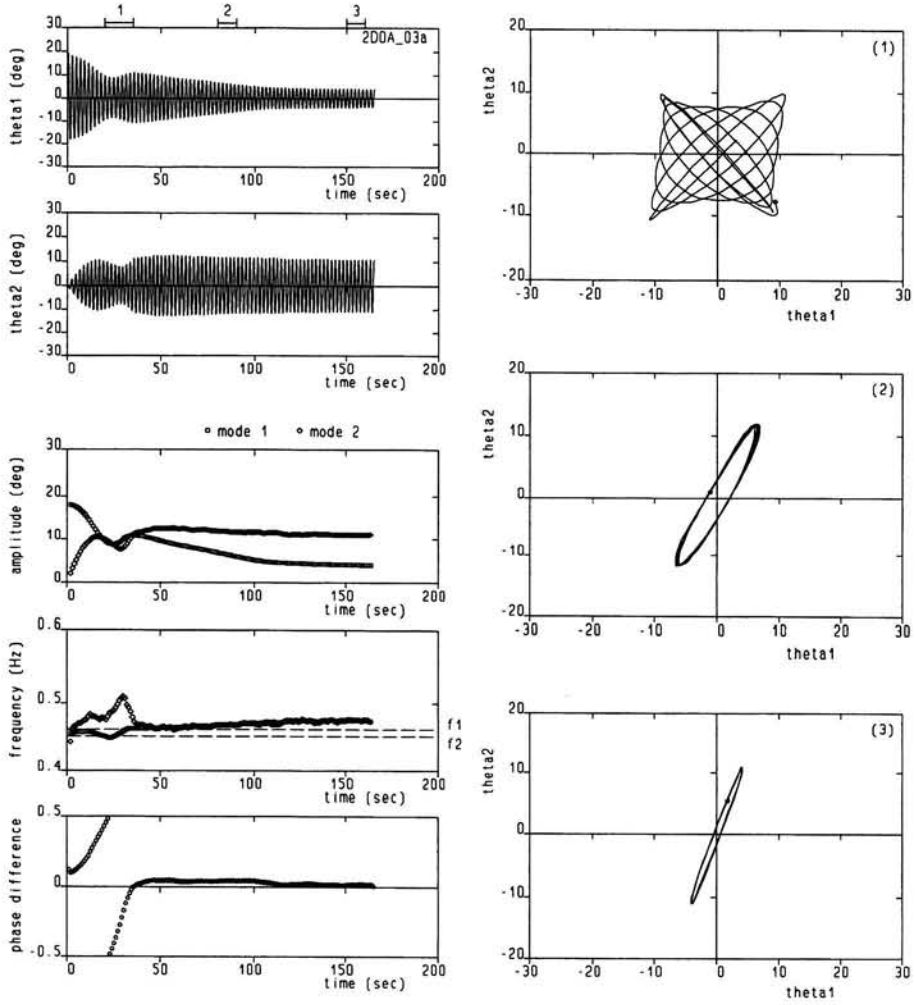
1
2
3
200A_03a
theta1 (deg)
theta2 (deg)
time (sec)
mode 1
mode 2
amplitude (deg)
frequency (Hz)
f1
f2
phase difference
(1)
(2)
(3)
theta2
theta1

Figure A3a.

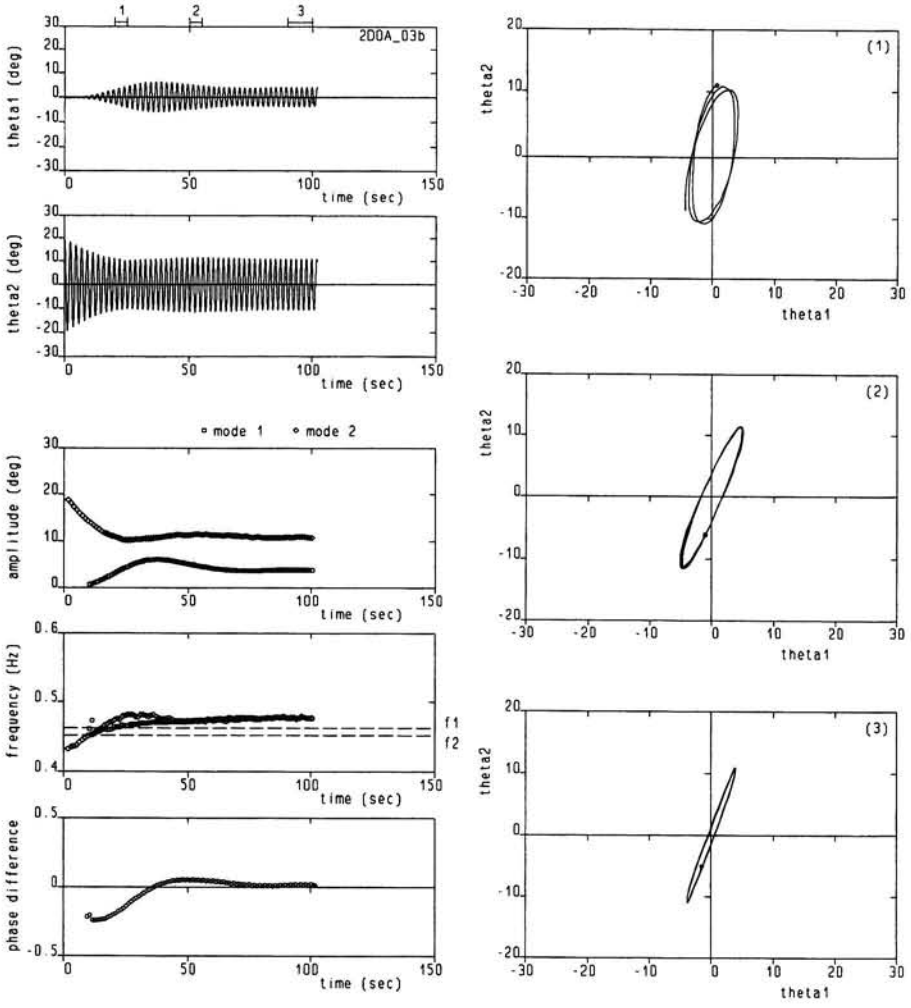
1
2
3
2D0A_03b
theta1 (deg)
theta2 (deg)
time (sec)
mode 1
mode 2
amplitude (deg)
frequency (Hz)
f1
f2
phase difference
(1)
(2)
(3)
theta2
theta1

Figure A3b.

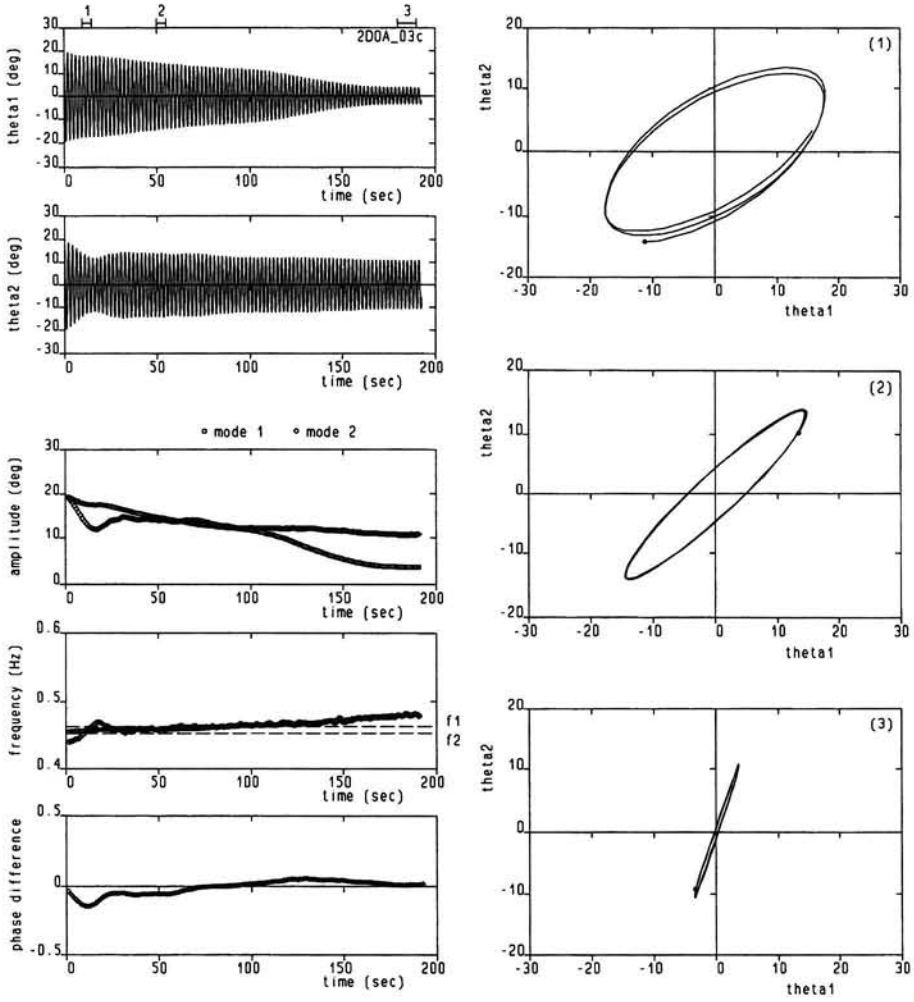
1
2
3
2DOA_03c
theta1 (deg)
theta2 (deg)
time (sec)
mode 1
mode 2
amplitude (deg)
frequency (Hz)
f1
f2
phase difference
theta2
theta1
(1)
(2)
(3)

Figure A3c.

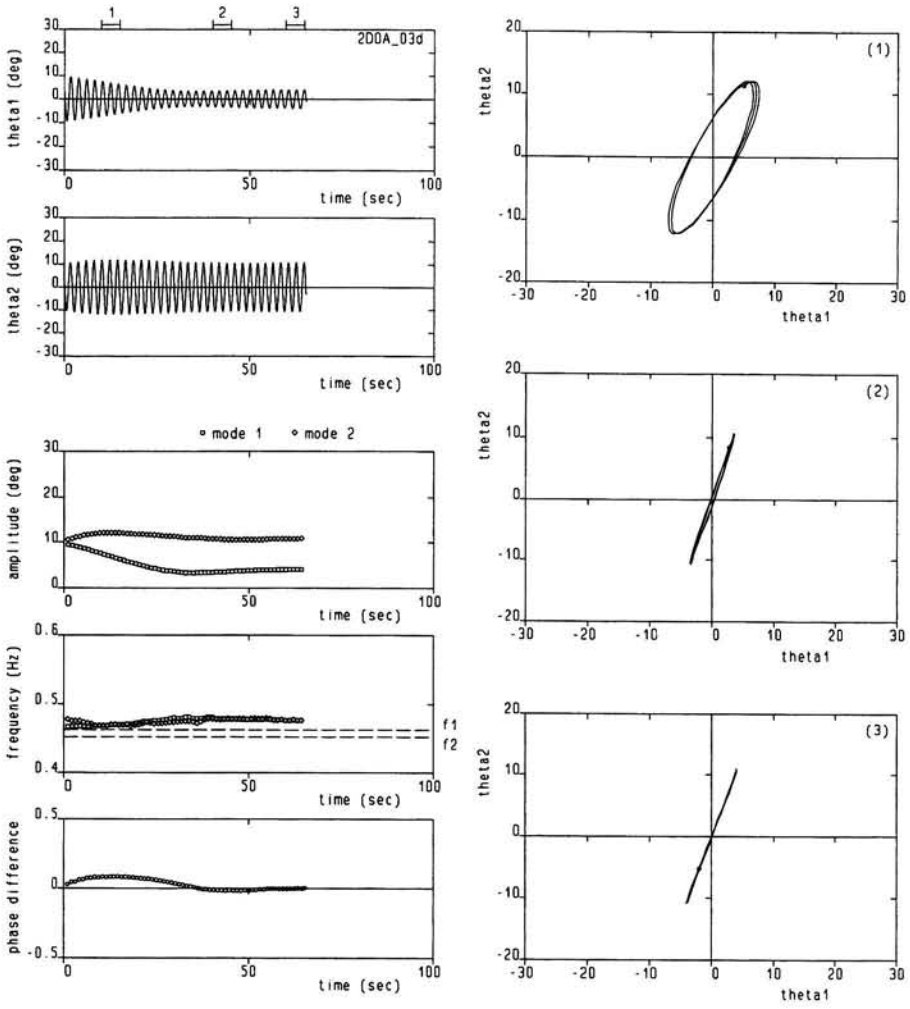
1
2
3
2D0A_03d
theta1 (deg)
time (sec)
theta2 (deg)
time (sec)
mode 1
mode 2
amplitude (deg)
time (sec)
frequency (Hz)
f1
f2
time (sec)
phase difference
time (sec)
(1)
theta2
theta1
(2)
theta2
theta1
(3)
theta2
theta1

Figure A3d.

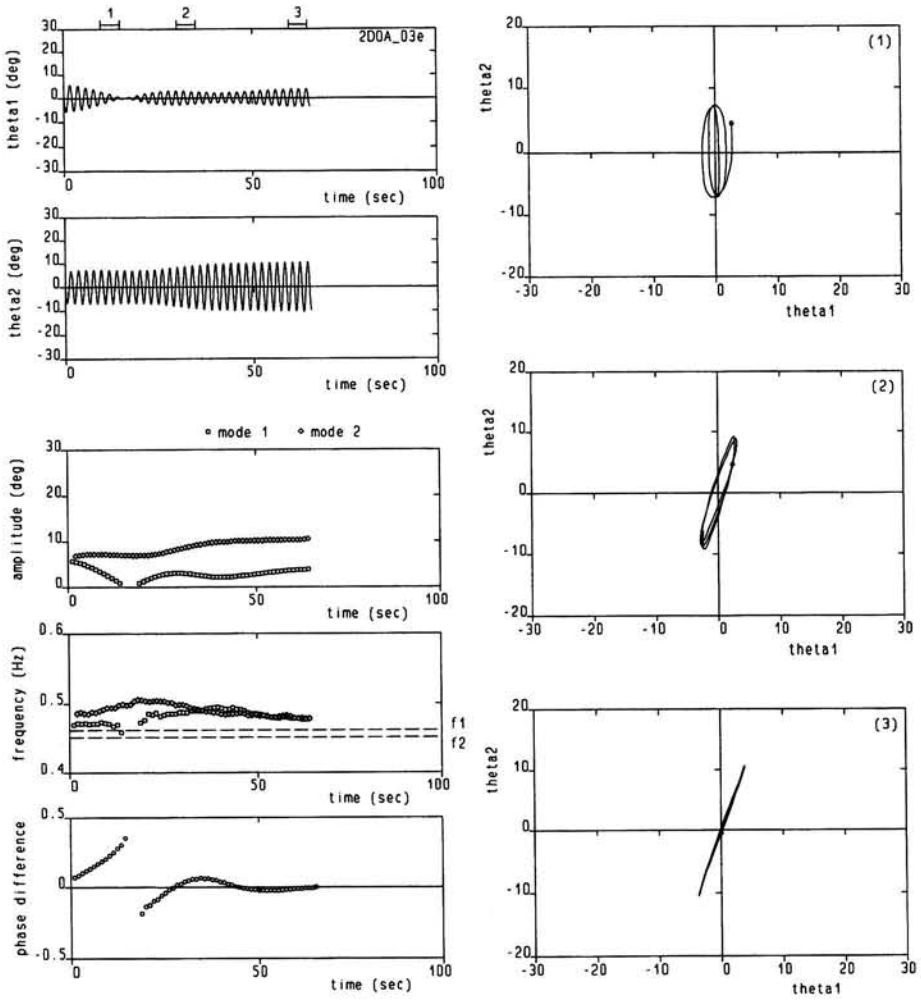
2DOA_03e
theta1 (deg)
theta2 (deg)
time (sec)
mode 1
mode 2
amplitude (deg)
frequency (Hz)
f1
f2
phase difference
theta2
theta1
(1)
(2)
(3)

Figure A3e.

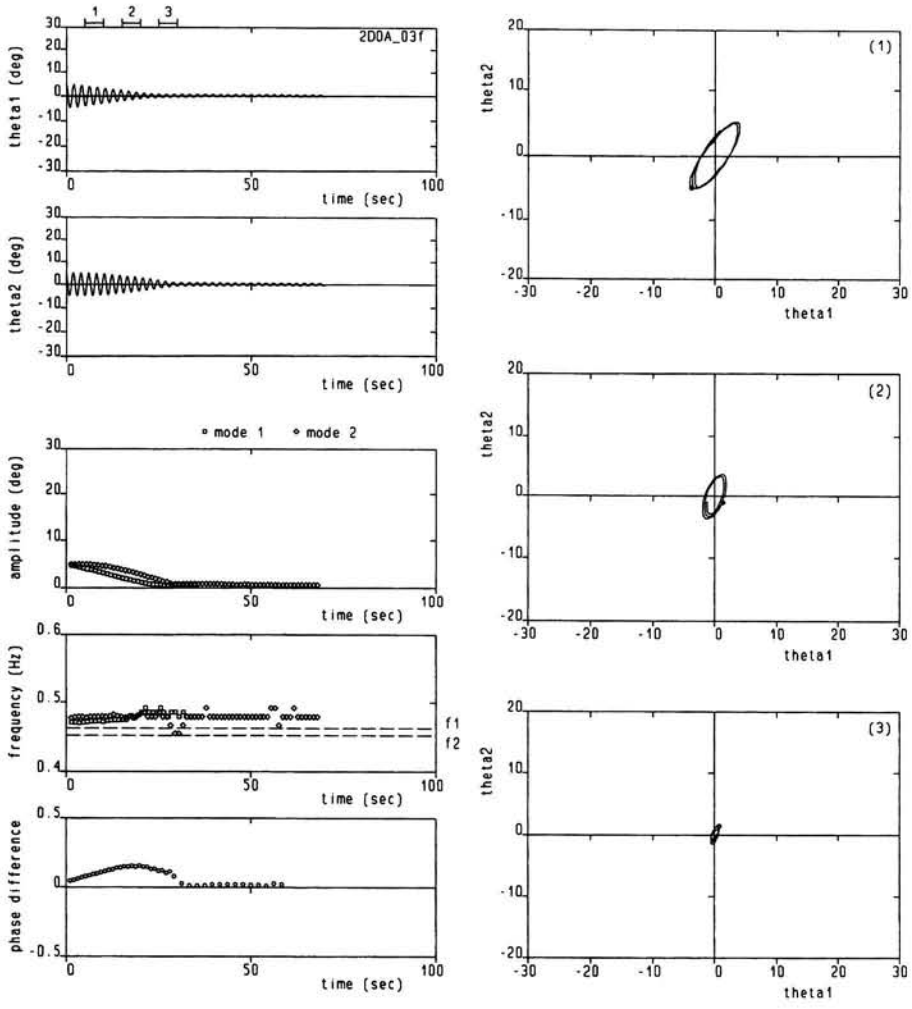
1
2
3
2D0A_03f
theta1 (deg)
theta2 (deg)
time (sec)
mode 1
mode 2
amplitude (deg)
frequency (Hz)
f1
f2
phase difference
(1)
(2)
(3)
theta2
theta1

Figure A3f.

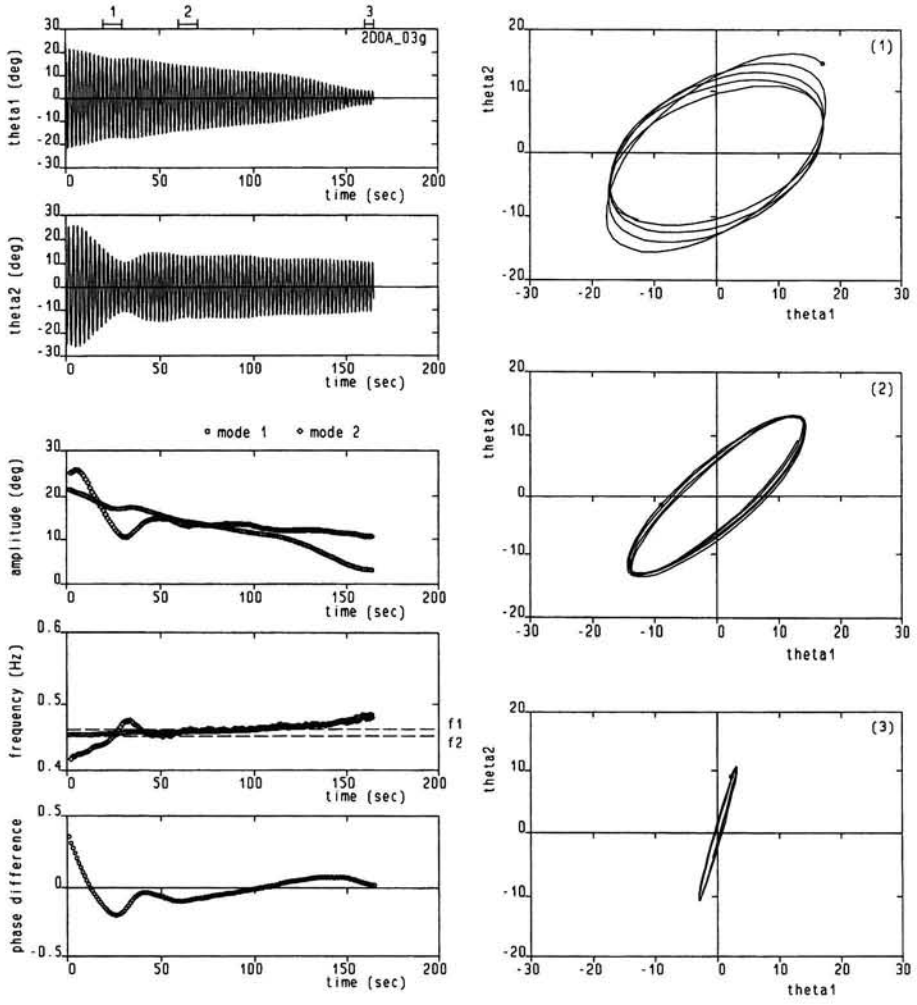
1
2
3
2D0A_03g
theta1 (deg)
theta2 (deg)
time (sec)
mode 1
mode 2
amplitude (deg)
frequency (Hz)
f1
f2
phase difference
(1)
(2)
(3)
theta2
theta1

Figure A3g.

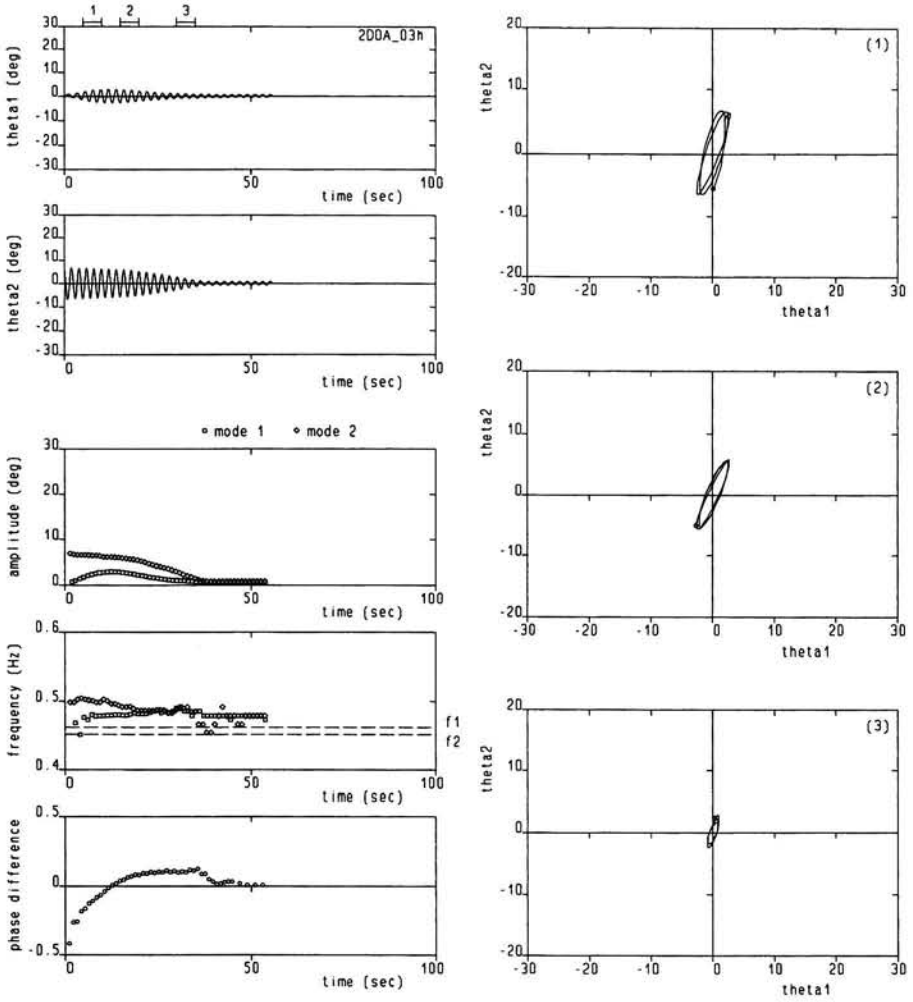
1
2
3
200A_03h
theta1 (deg)
time (sec)
theta2 (deg)
time (sec)
mode 1
mode 2
amplitude (deg)
time (sec)
frequency (Hz)
f1
f2
time (sec)
phase difference
time (sec)
theta2
(1)
theta1
theta2
(2)
theta1
theta2
(3)
theta1

Figure A3h.

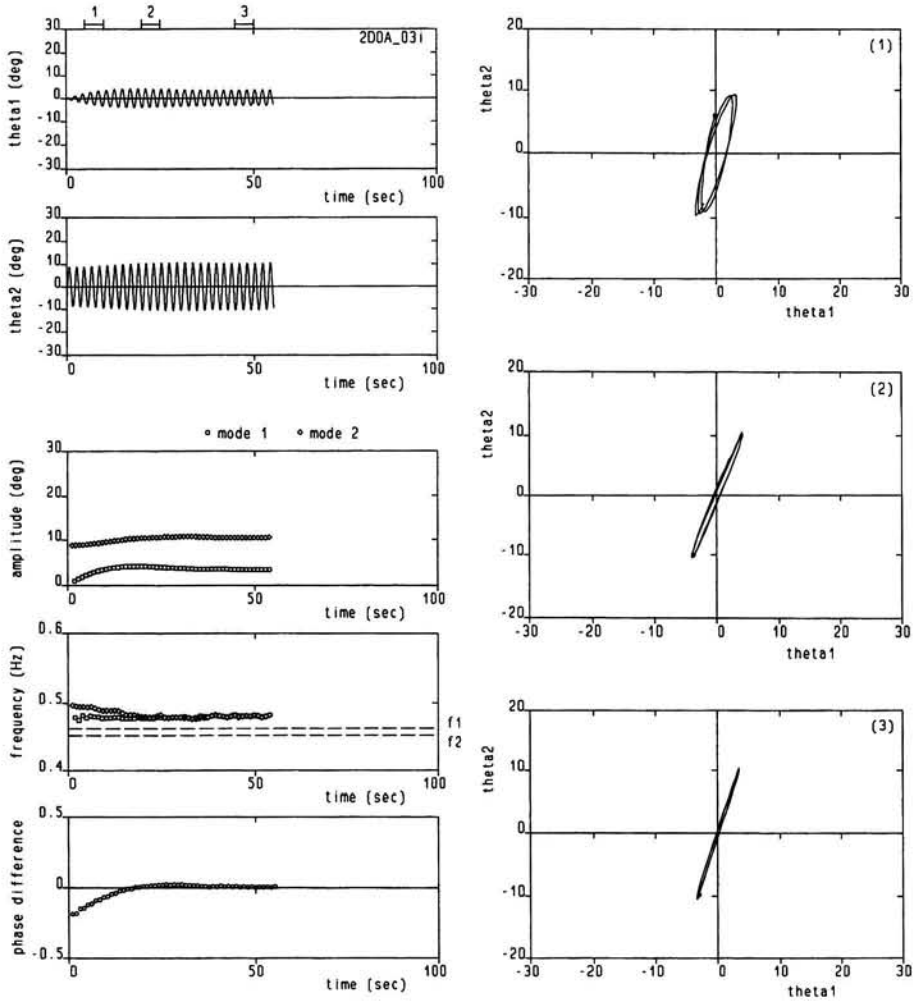
1
2
3
2D0A_031
theta1 (deg)
theta2 (deg)
time (sec)
mode 1
mode 2
amplitude (deg)
frequency (Hz)
f1
f2
phase difference
theta2
theta1
(1)
(2)
(3)

Figure A3i.

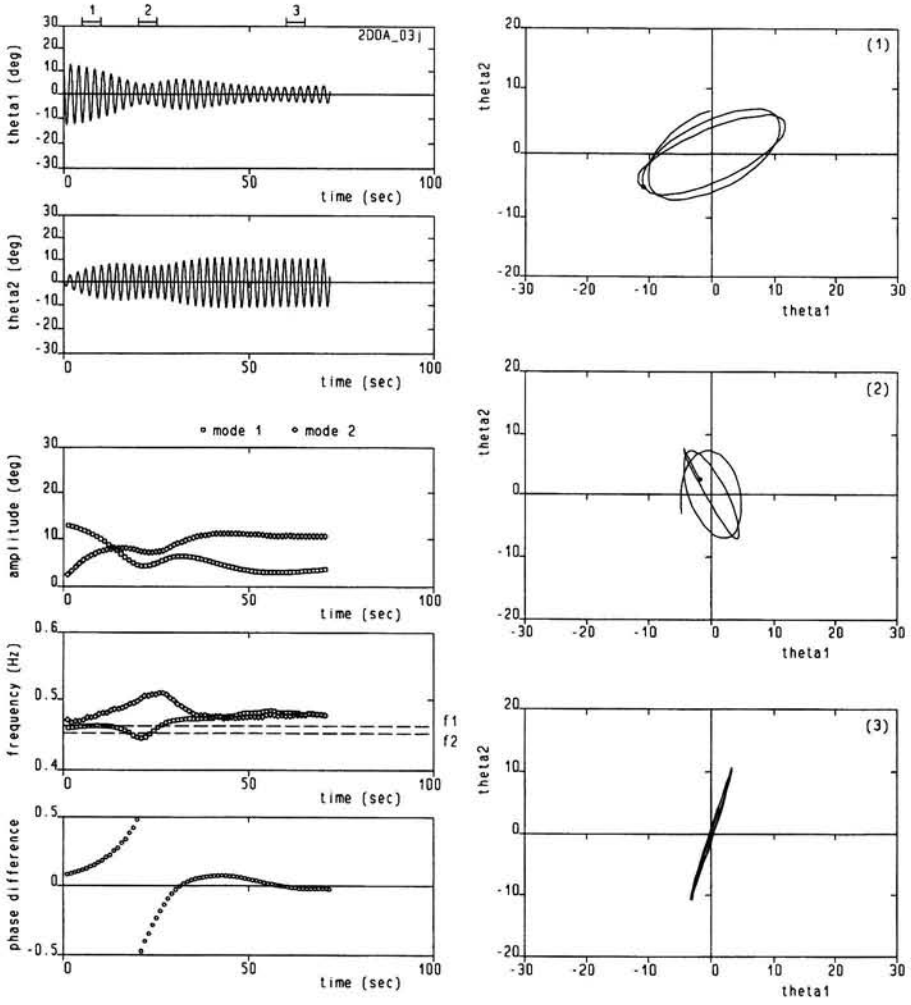
1
2
3
2DOA_03j
theta1 (deg)
time (sec)
theta2 (deg)
time (sec)
mode 1
mode 2
amplitude (deg)
time (sec)
frequency (Hz)
f1
f2
time (sec)
phase difference
time (sec)
(1)
theta2
theta1
(2)
theta2
theta1
(3)
theta2
theta1

Figure A3j.

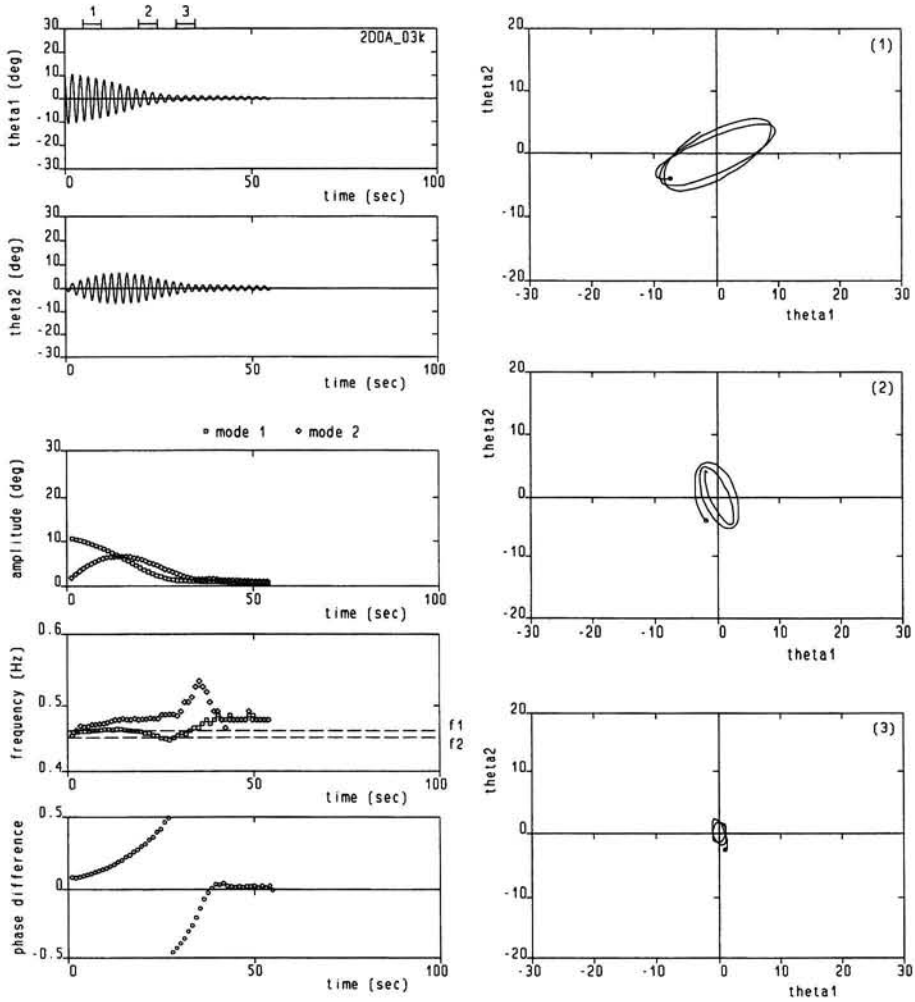
1
2
3
2DOA_03k
theta1 (deg)
theta2 (deg)
time (sec)
mode 1
mode 2
amplitude (deg)
frequency (Hz)
f1
f2
phase difference
theta2
theta1
(1)
(2)
(3)

Figure A3k.

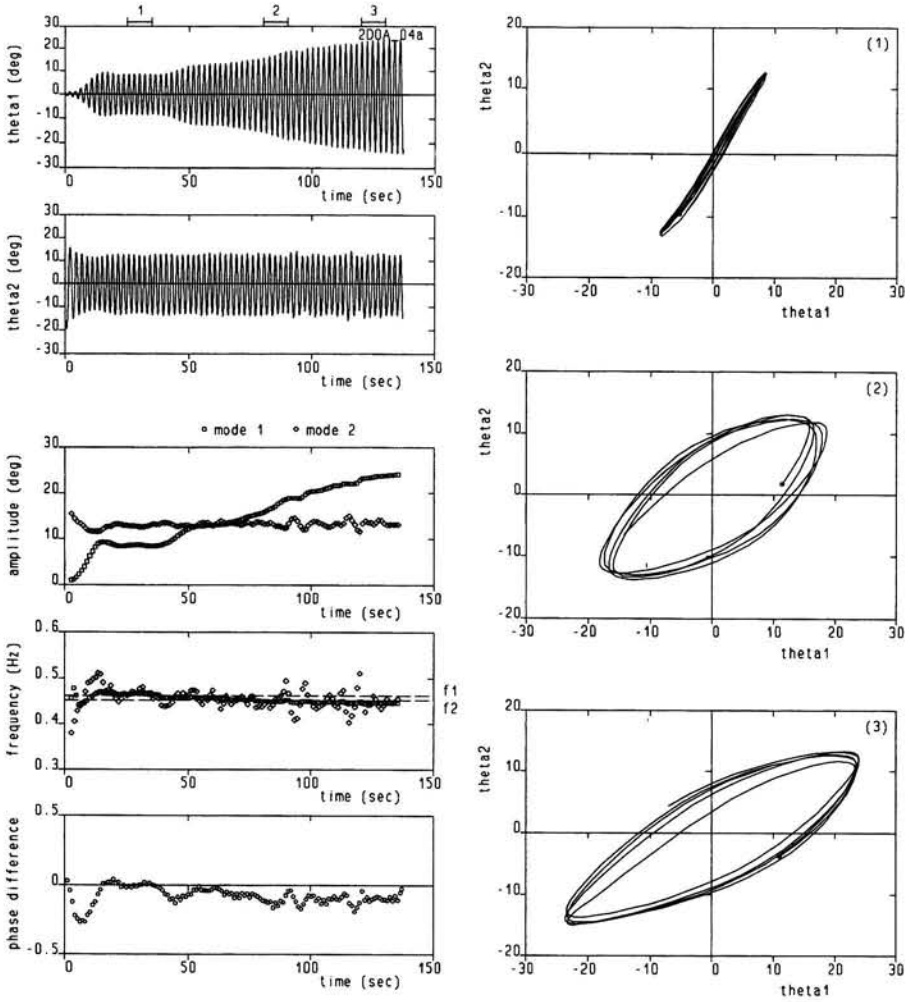
1
2
3
2D0A_04a
theta1 (deg)
theta2 (deg)
time (sec)
mode 1
mode 2
amplitude (deg)
frequency (Hz)
f1
f2
phase difference
(1)
(2)
(3)
theta2
theta1

Figure A4a.

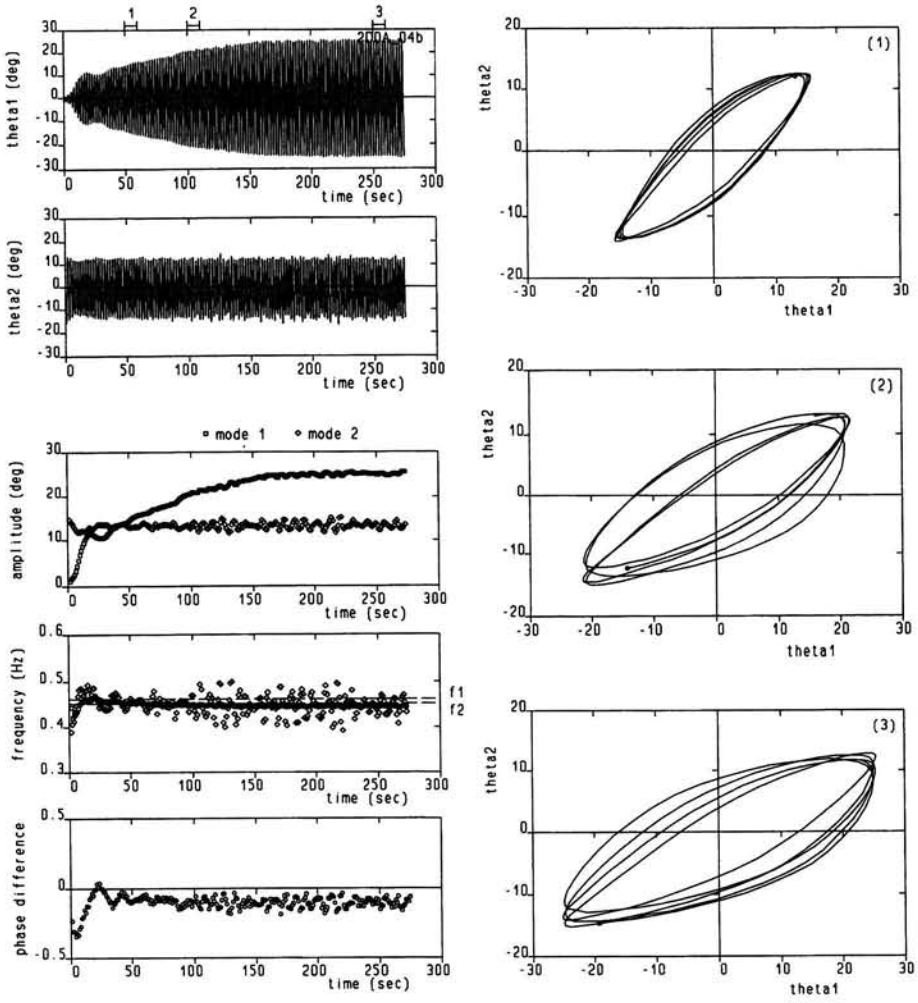
1
2
3
200A_04b
theta1 (deg)
theta2 (deg)
time (sec)
mode 1
mode 2
amplitude (deg)
frequency (Hz)
f1
f2
phase difference
theta2
theta1
(1)
(2)
(3)

Figure A4b.

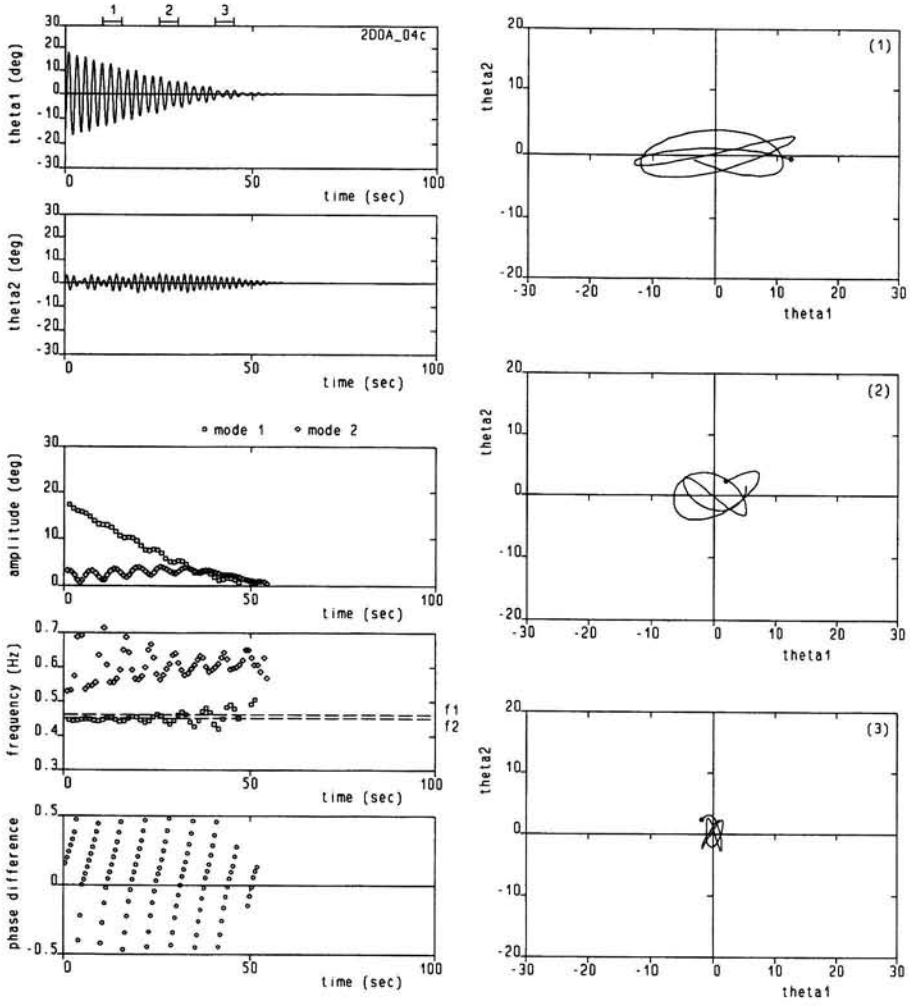
1
2
3
2DOA_04c
theta1 (deg)
time (sec)
theta2 (deg)
time (sec)
mode 1
mode 2
amplitude (deg)
time (sec)
frequency (Hz)
f1
f2
time (sec)
phase difference
time (sec)
(1)
theta2
theta1
(2)
theta2
theta1
(3)
theta2
theta1

Figure A4c.

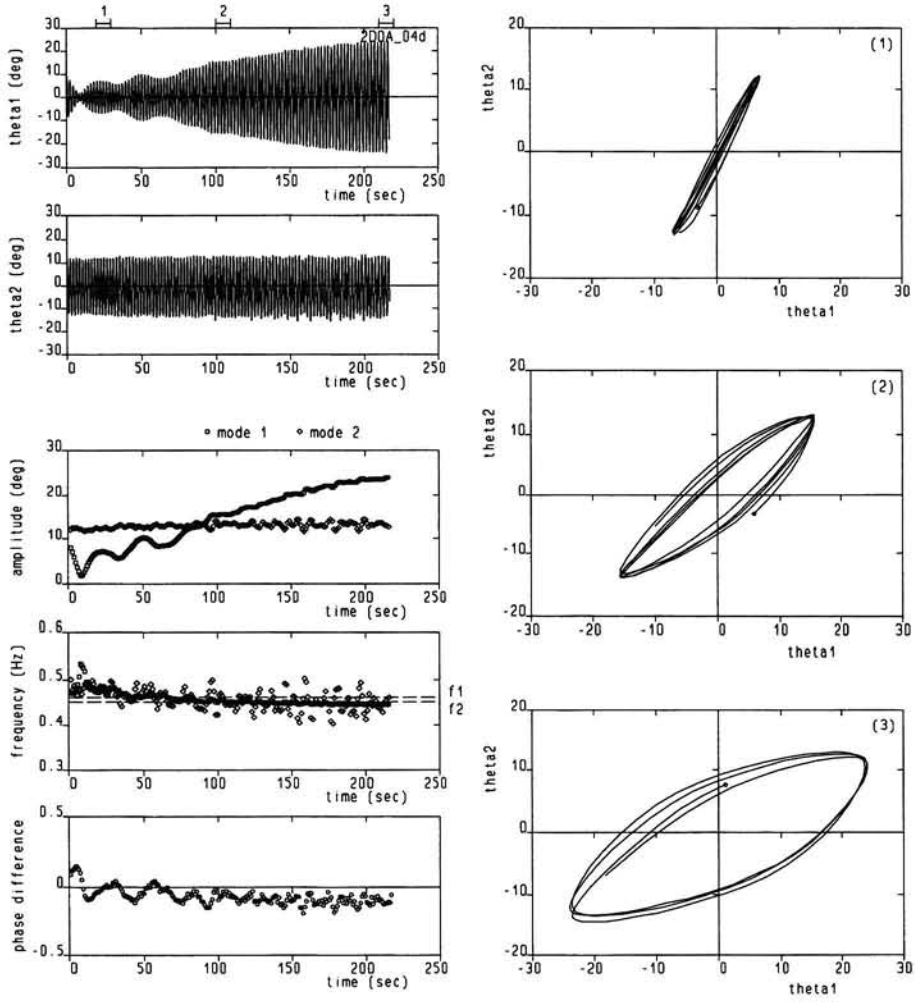
1
2
3
200A_04d
theta1 (deg)
theta2 (deg)
time (sec)
mode 1
mode 2
amplitude (deg)
frequency (Hz)
f1
f2
phase difference
(1)
(2)
(3)
theta2
theta1

Figure A4d.

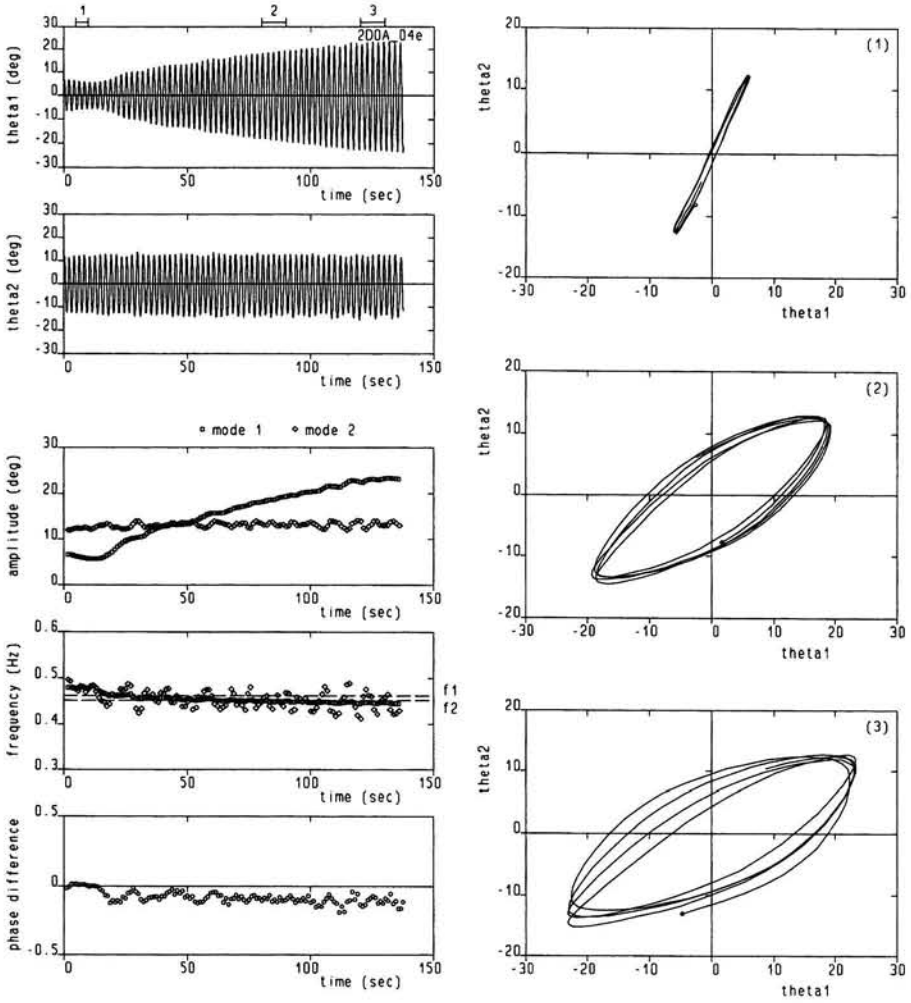
1
2
3
2D0A_04e
theta1 (deg)
time (sec)
theta2 (deg)
time (sec)
mode 1
mode 2
amplitude (deg)
time (sec)
frequency (Hz)
f1
f2
time (sec)
phase difference
time (sec)
(1)
theta2
theta1
(2)
theta2
theta1
(3)
theta2
theta1

Figure A4e.

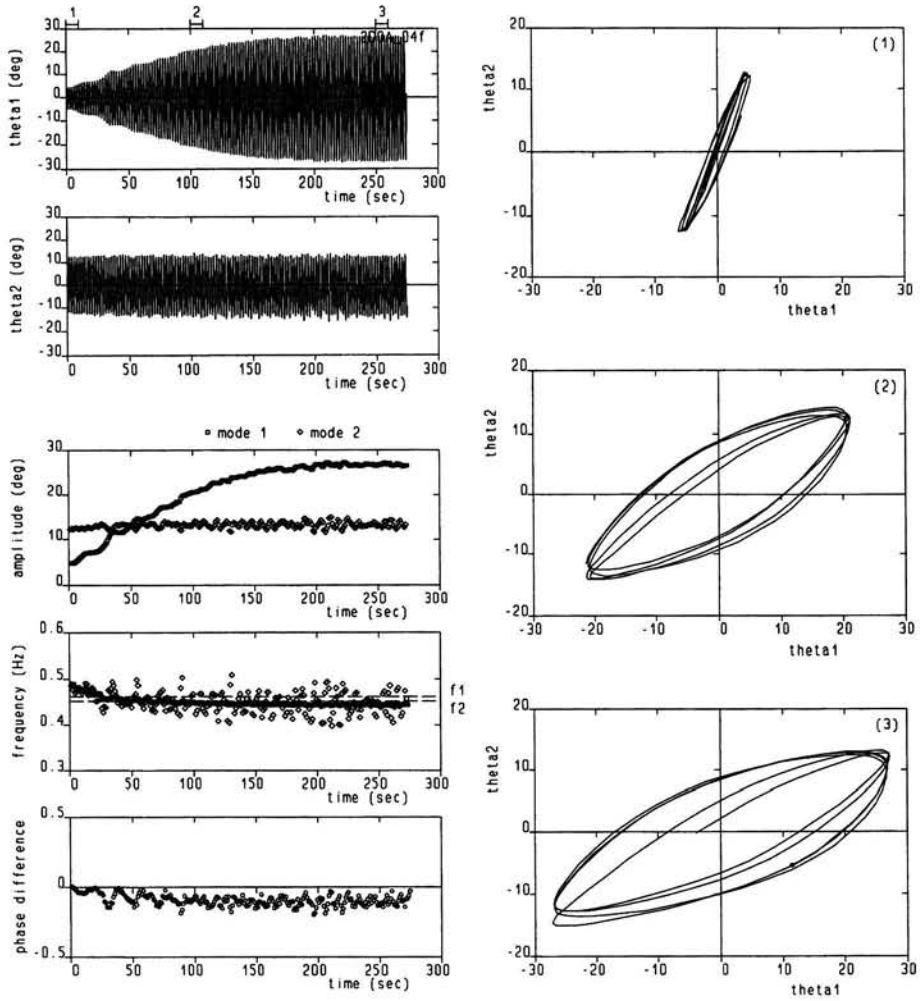
1
2
3
theta1 (deg)
theta2 (deg)
time (sec)
mode 1
mode 2
amplitude (deg)
frequency (Hz)
f1
f2
phase difference
theta2
theta1
(1)
(2)
(3)

Figure A4f.

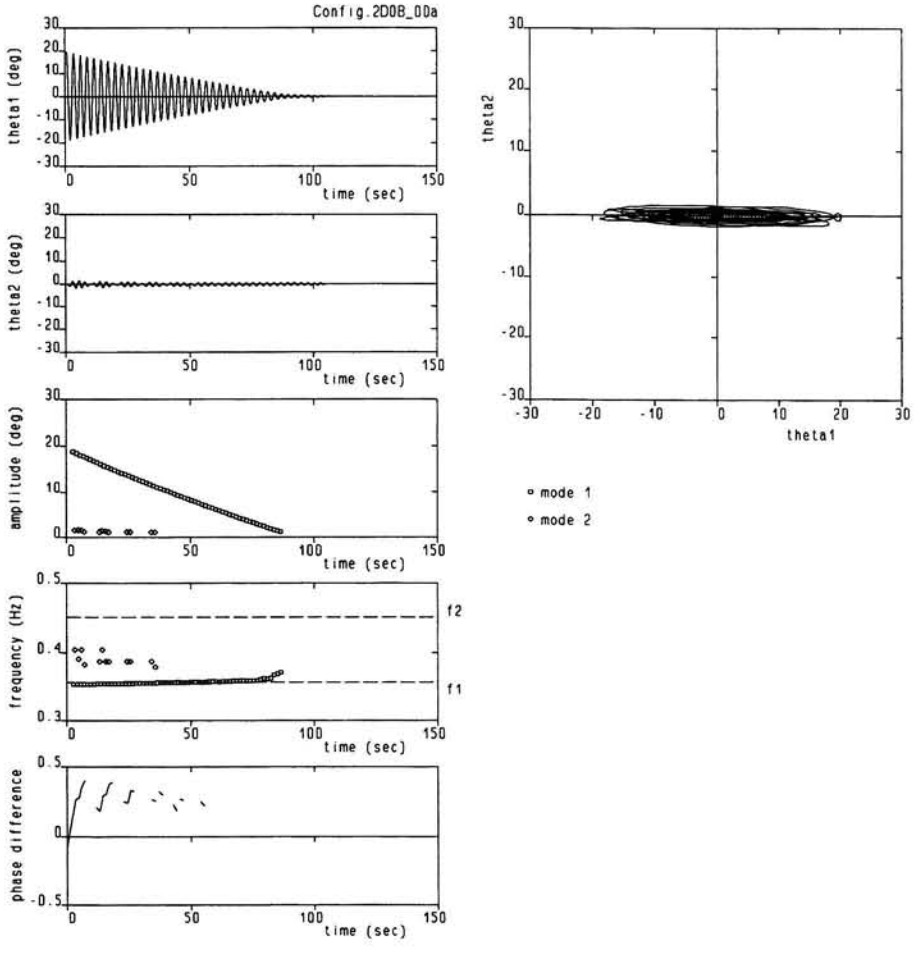
Config.2D0B_00a
theta1 (deg)
theta2 (deg)
amplitude (deg)
frequency (Hz)
phase difference
time (sec)
f2
f1
theta2
theta1
mode 1
mode 2

Figure B0a.

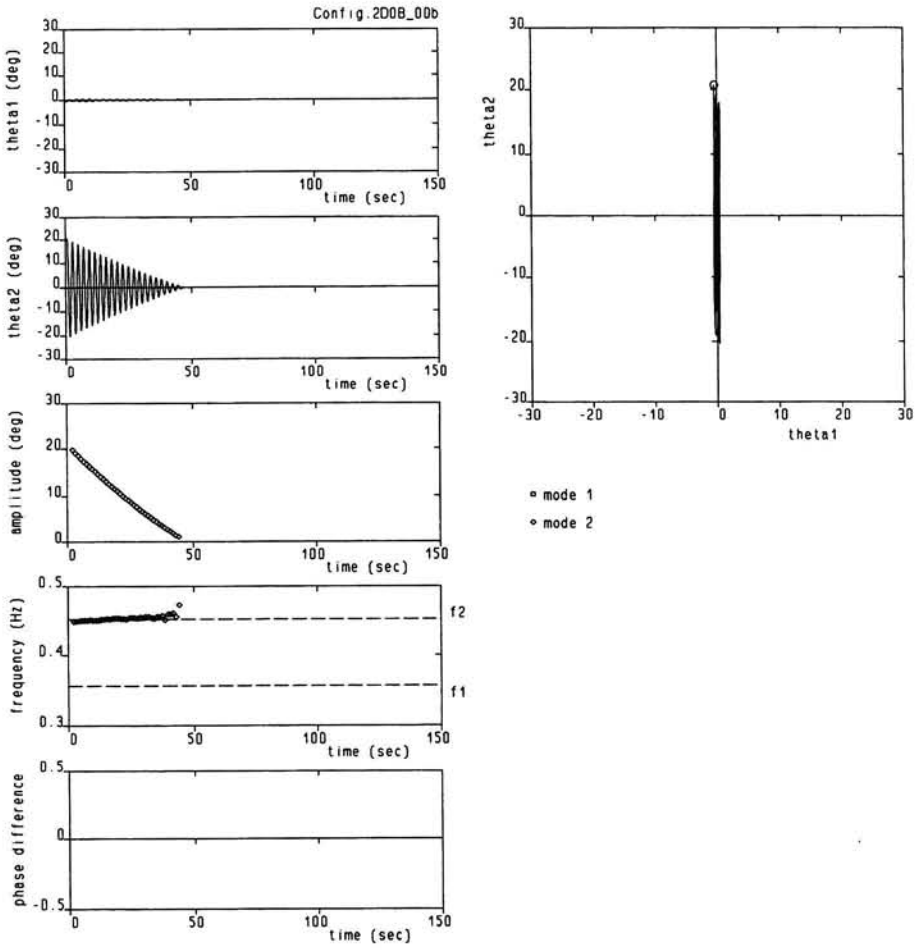
Config.2D0B_00b
theta1 (deg)
theta2 (deg)
amplitude (deg)
frequency (Hz)
phase difference
time (sec)
f2
f1
theta2
theta1
mode 1
mode 2

Figure B0b.

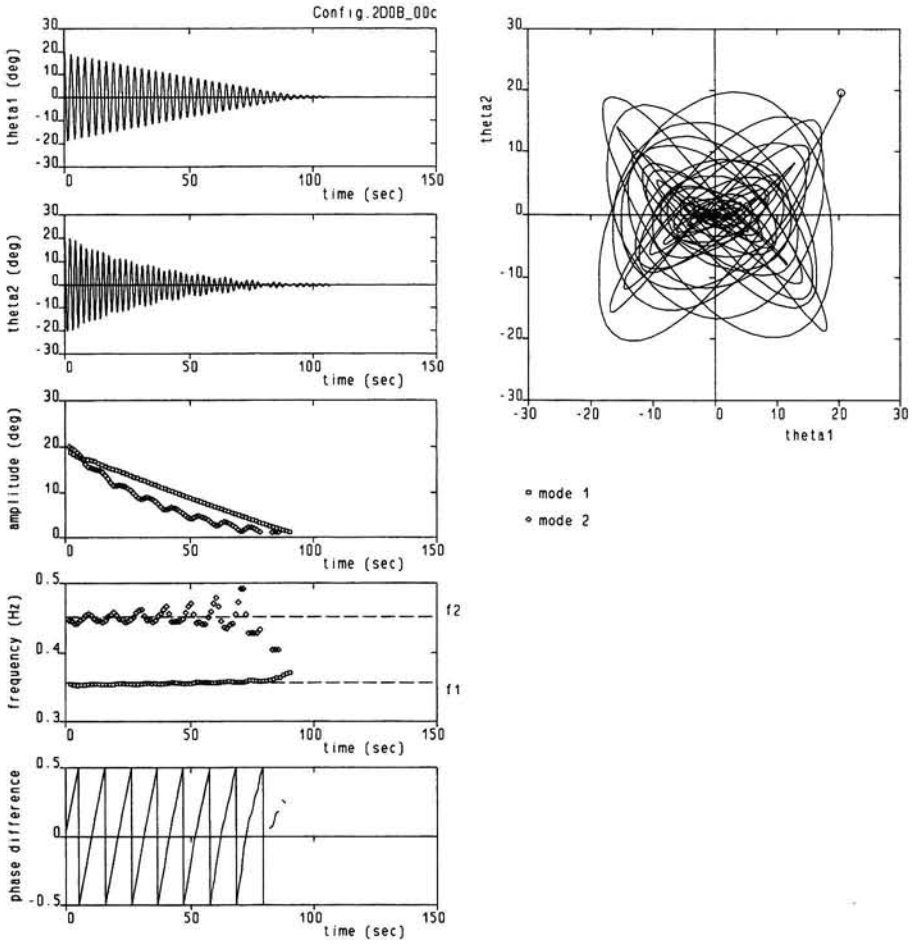
Config.2D0B_00c
theta1 (deg)
theta2 (deg)
amplitude (deg)
frequency (Hz)
phase difference
time (sec)
f2
f1
theta2
theta1
mode 1
mode 2

Figure B0c.

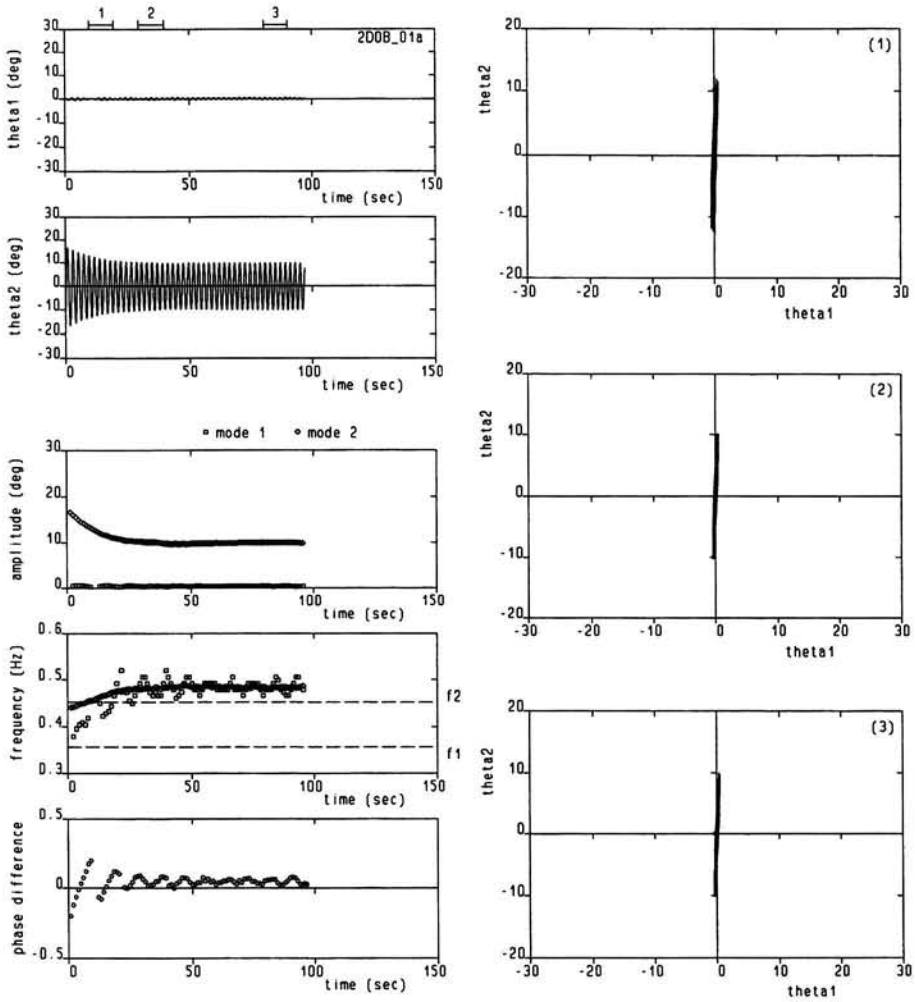
1
2
3
2DOB_01a
theta1 (deg)
theta2 (deg)
time (sec)
mode 1
mode 2
amplitude (deg)
frequency (Hz)
f2
f1
phase difference
theta2
theta1
(1)
(2)
(3)

Figure B1a.

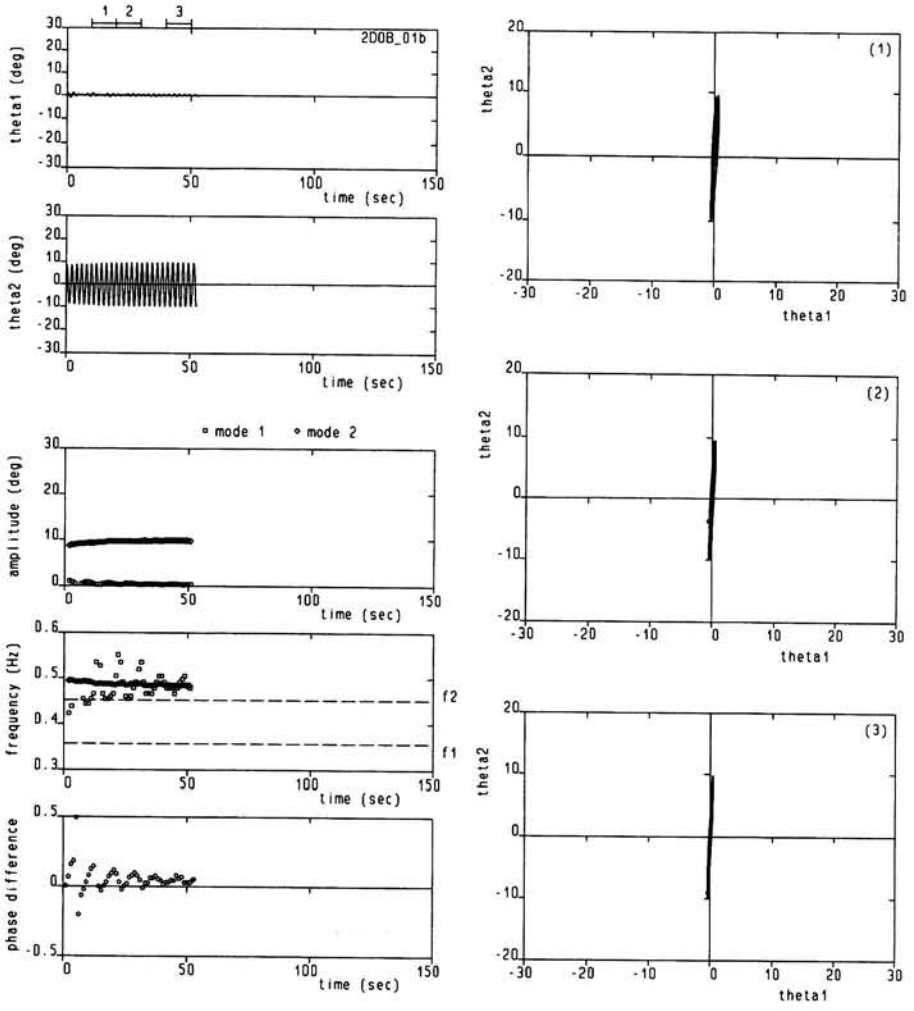
1 2 3
2D0B_01b
theta1 (deg)
time (sec)
theta2 (deg)
mode 1
mode 2
amplitude (deg)
frequency (Hz)
f2
f1
phase difference
(1)
(2)
(3)
theta2
theta1

Figure B1b.

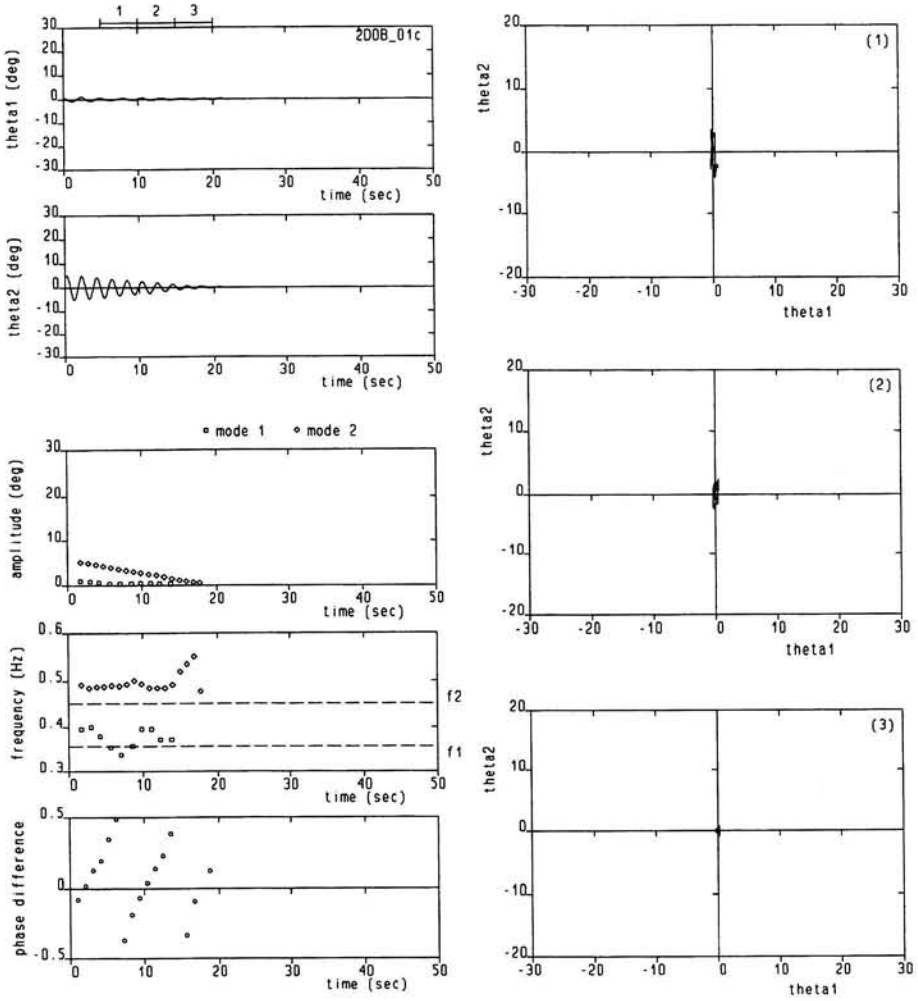
1 2 3
2008_01c
theta1 (deg)
theta2 (deg)
time (sec)
mode 1
mode 2
amplitude (deg)
frequency (Hz)
f2
f1
phase difference
(1)
(2)
(3)
theta2
theta1

Figure B1c.

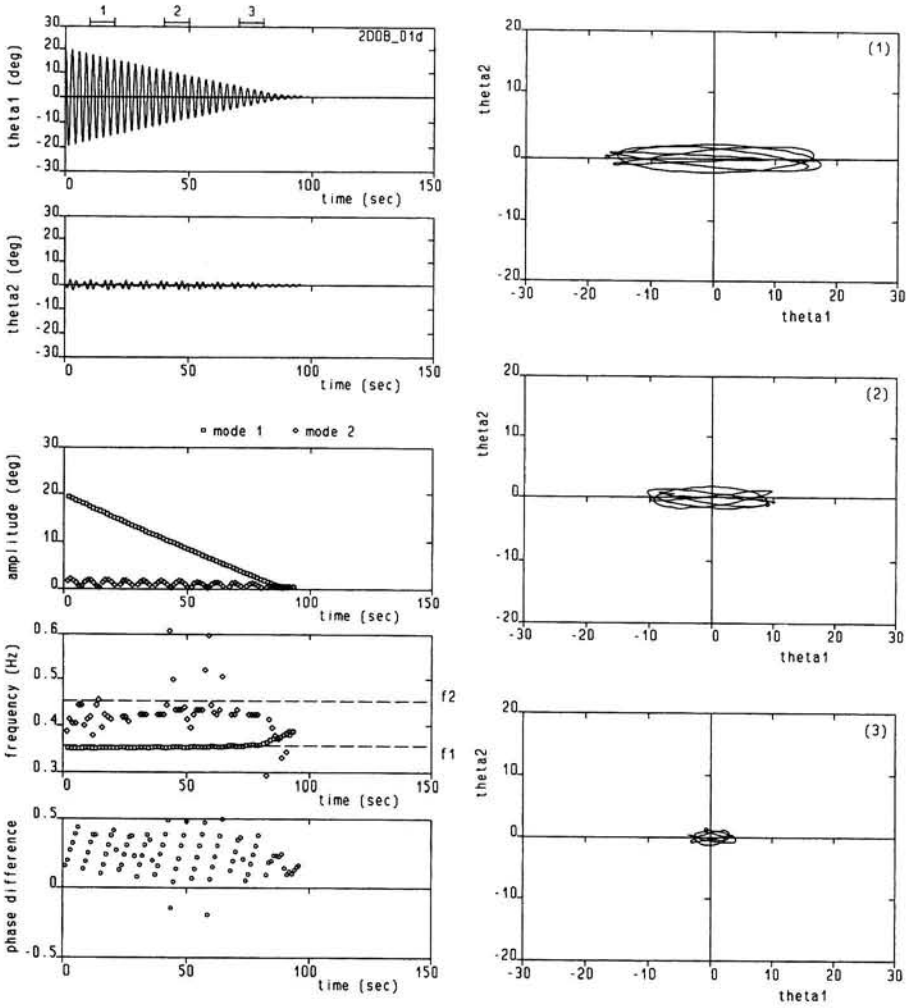
1
2
3
2DOB_01d
theta1 (deg)
time (sec)
theta2 (deg)
mode 1
mode 2
amplitude (deg)
frequency (Hz)
f2
f1
phase difference
theta2
theta1
(1)
(2)
(3)

Figure B1d.

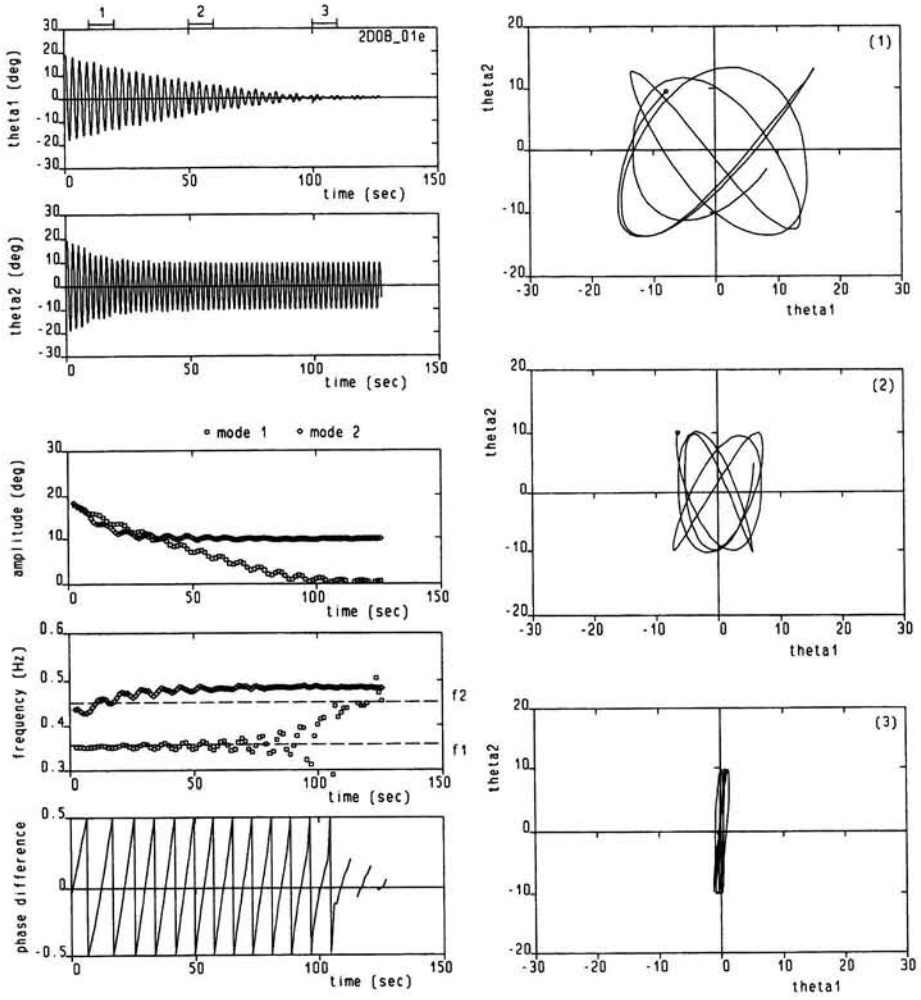
1
2
3
2D0B_01e
theta1 (deg)
time (sec)
theta2 (deg)
time (sec)
mode 1
mode 2
amplitude (deg)
time (sec)
frequency (Hz)
f2
f1
time (sec)
phase difference
time (sec)
(1)
theta2
theta1
(2)
theta2
theta1
(3)
theta2
theta1

Figure B1e.

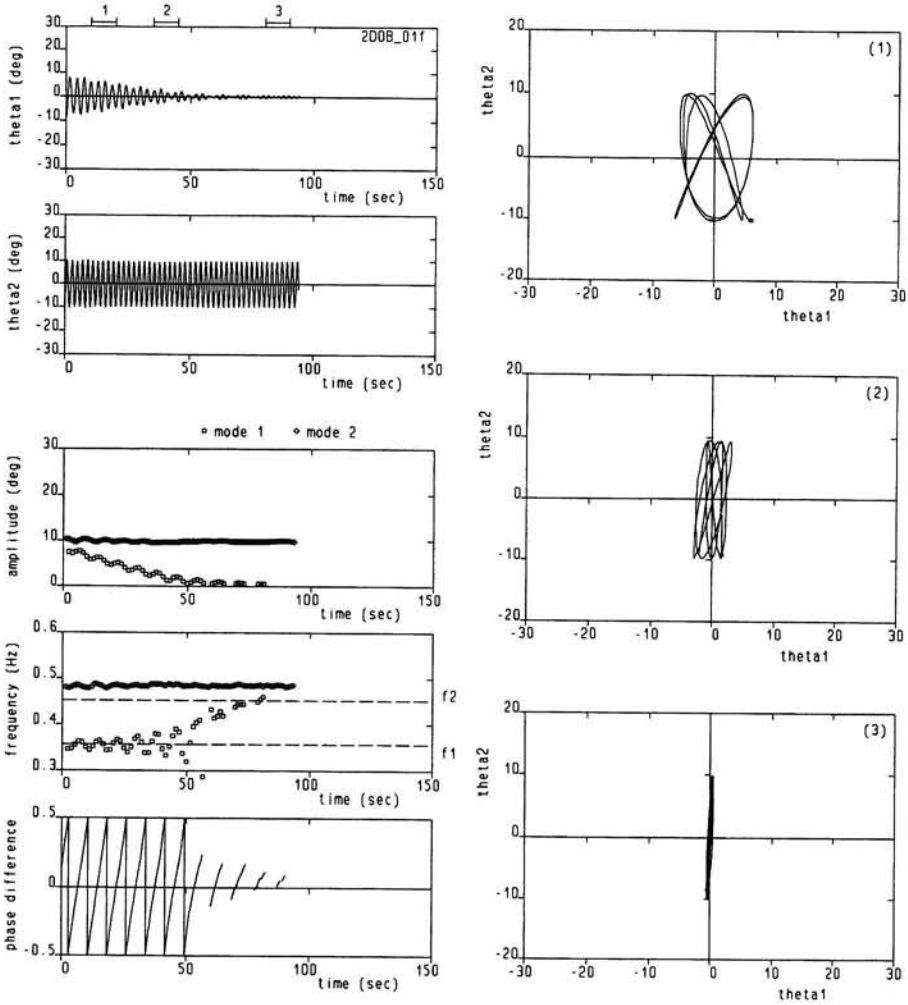
1
2
3
2008_01f
theta1 (deg)
theta2 (deg)
time (sec)
mode 1
mode 2
amplitude (deg)
frequency (Hz)
f2
f1
phase difference
theta2
theta1
(1)
(2)
(3)

Figure B1f.

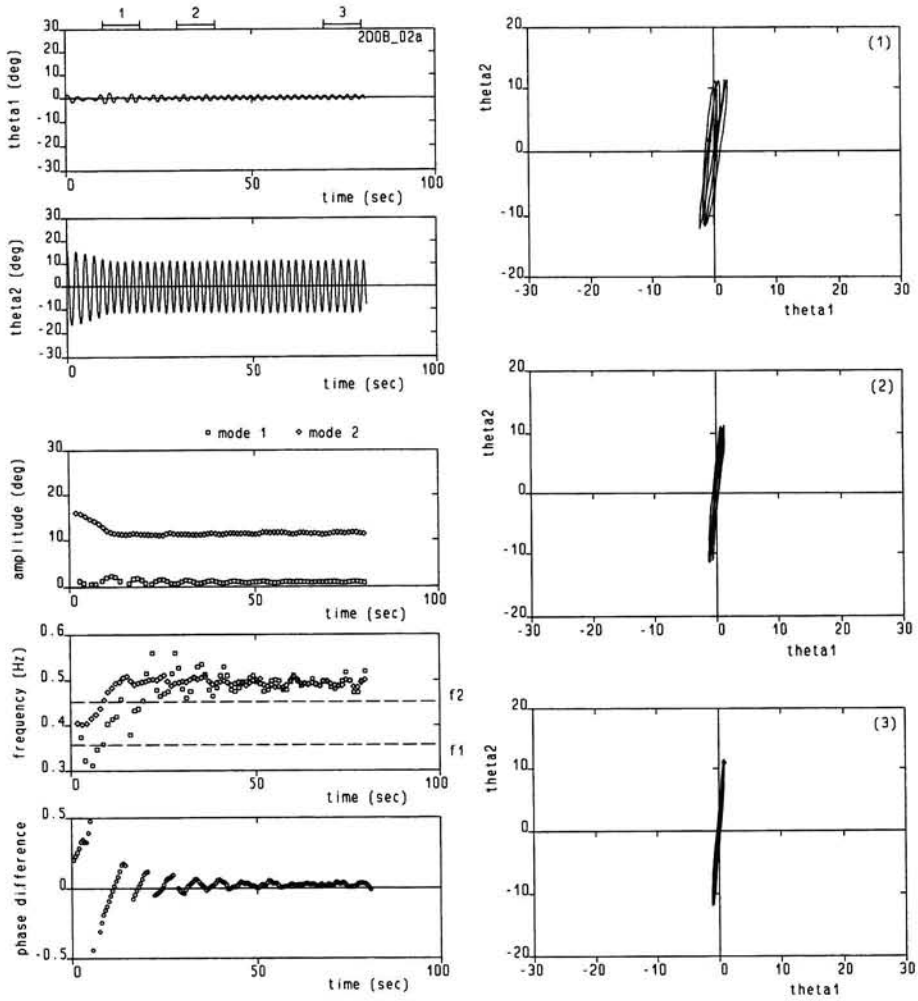
1
2
3
2008_02a
theta1 (deg)
time (sec)
theta2 (deg)
time (sec)
mode 1
mode 2
amplitude (deg)
time (sec)
frequency (Hz)
f2
f1
time (sec)
phase difference
time (sec)
theta2
(1)
theta1
theta2
(2)
theta1
theta2
(3)
theta1

Figure B2a.

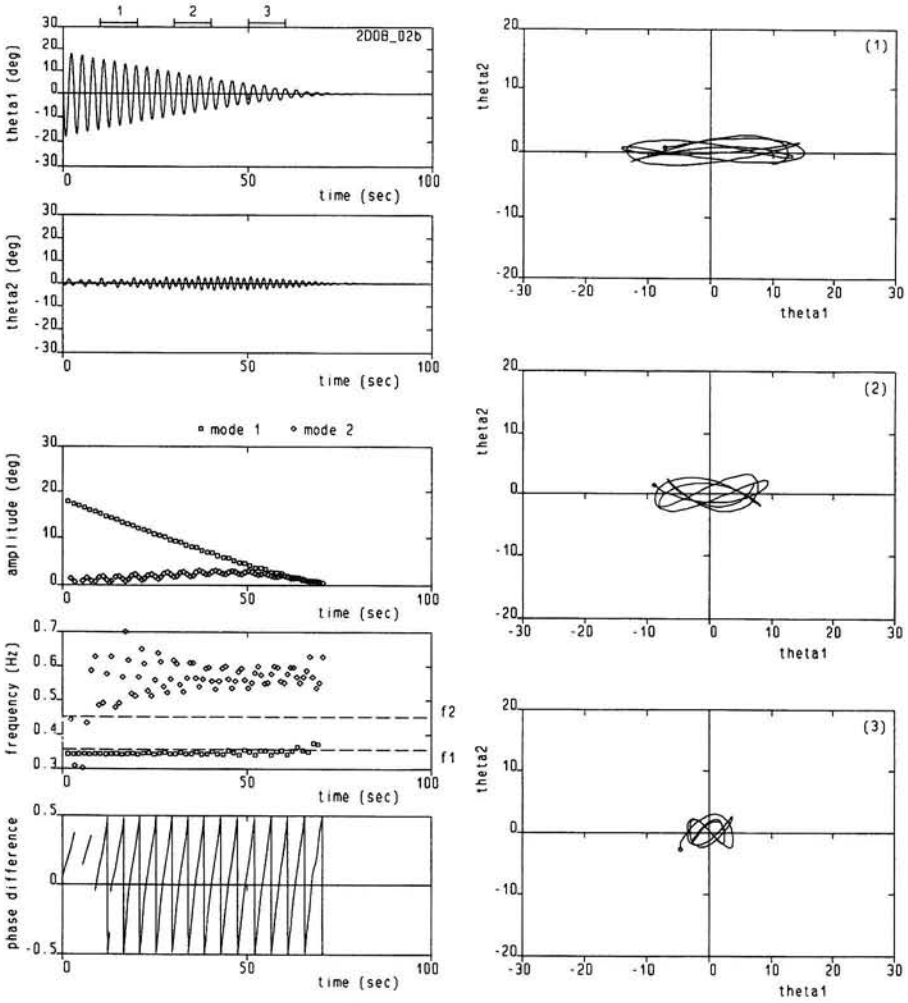
1
2
3
2D0B_02b
theta1 (deg)
time (sec)
theta2 (deg)
time (sec)
mode 1
mode 2
amplitude (deg)
time (sec)
frequency (Hz)
f2
f1
time (sec)
phase difference
time (sec)
(1)
theta2
theta1
(2)
theta2
theta1
(3)
theta2
theta1

Figure B2b.

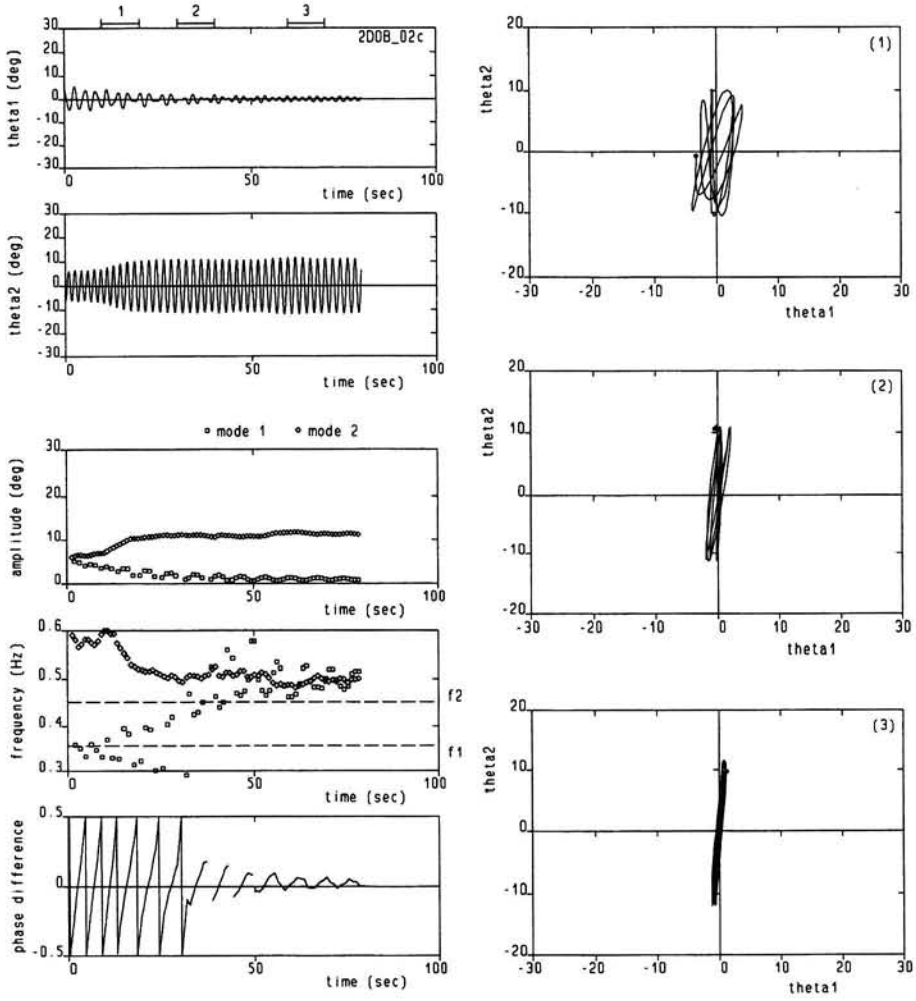
1
2
3
2D0B_02c
theta1 (deg)
time (sec)
theta2 (deg)
mode 1
mode 2
amplitude (deg)
frequency (Hz)
f2
f1
phase difference
theta2
theta1
(1)
(2)
(3)

Figure B2c.

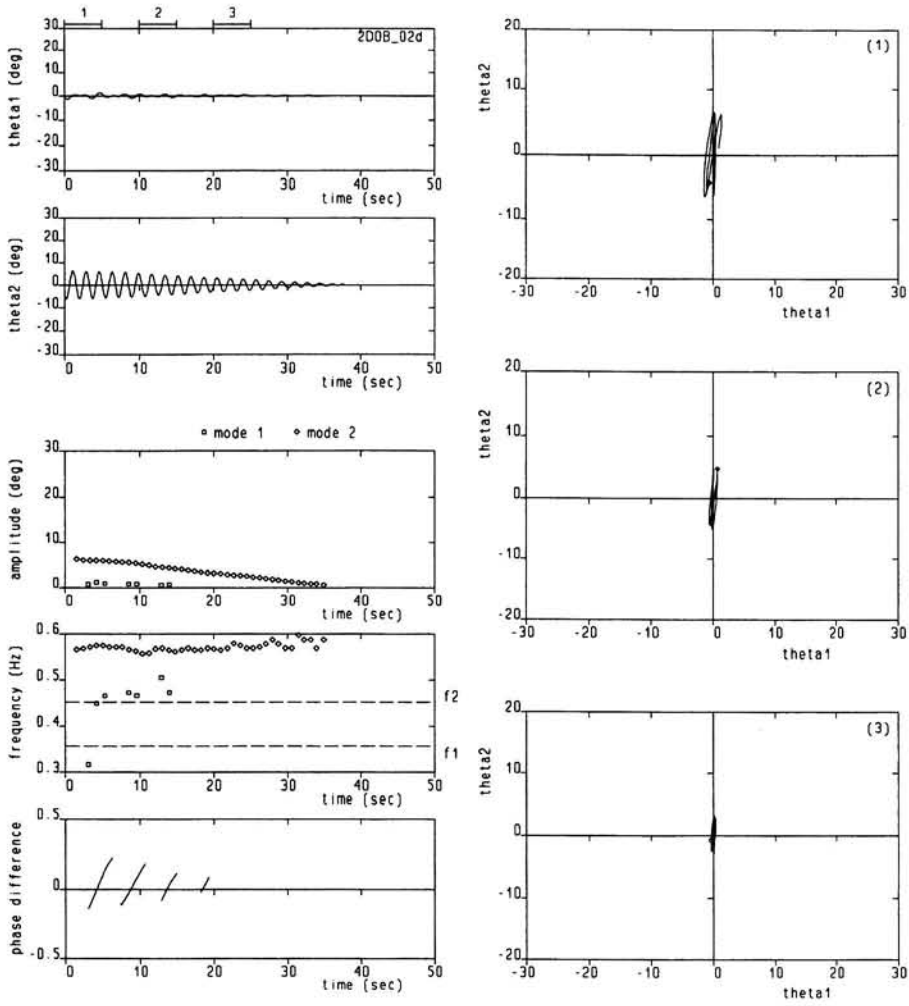
1
2
3
2008_02d
theta1 (deg)
time (sec)
theta2 (deg)
time (sec)
mode 1
mode 2
amplitude (deg)
time (sec)
frequency (Hz)
f2
f1
time (sec)
phase difference
time (sec)
theta2
(1)
theta1
theta2
(2)
theta1
theta2
(3)
theta1

Figure B2d.

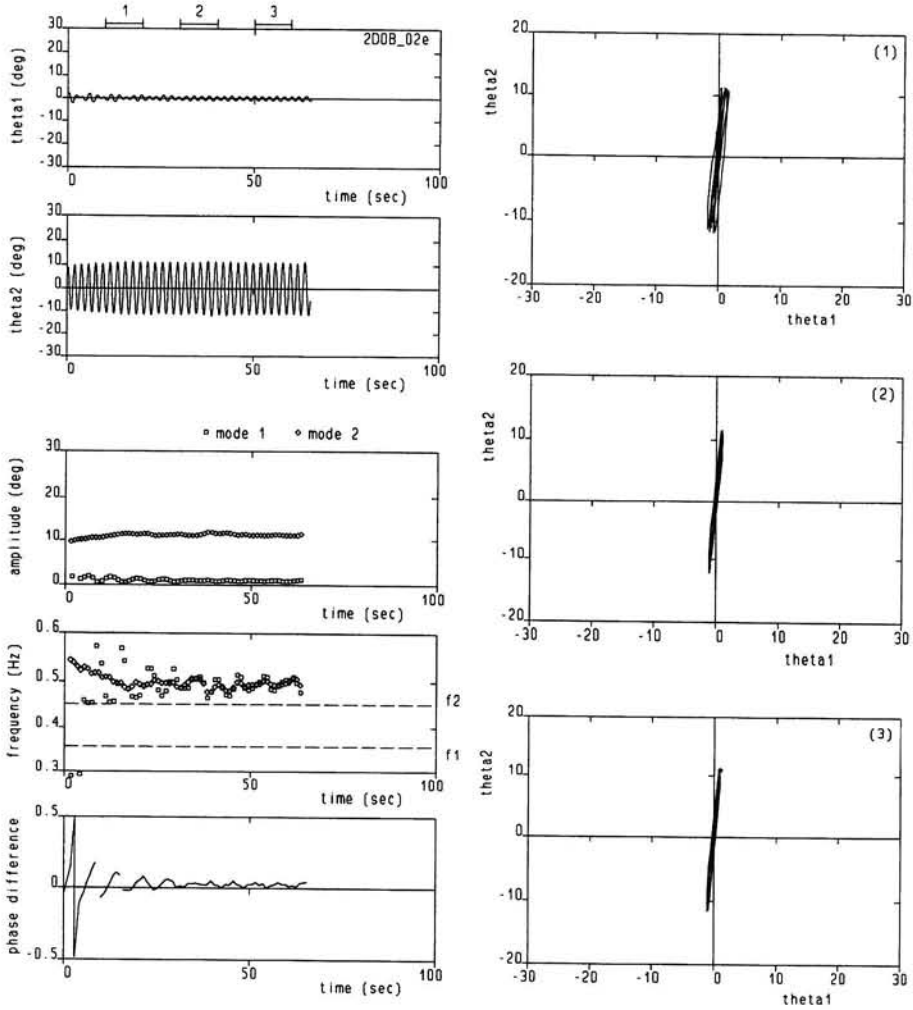
1
2
3
2008_02e
theta1 (deg)
time (sec)
theta2 (deg)
time (sec)
mode 1
mode 2
amplitude (deg)
time (sec)
frequency (Hz)
f2
f1
time (sec)
phase difference
time (sec)
theta2
(1)
theta1
theta2
(2)
theta1
theta2
(3)
theta1

Figure B2e.

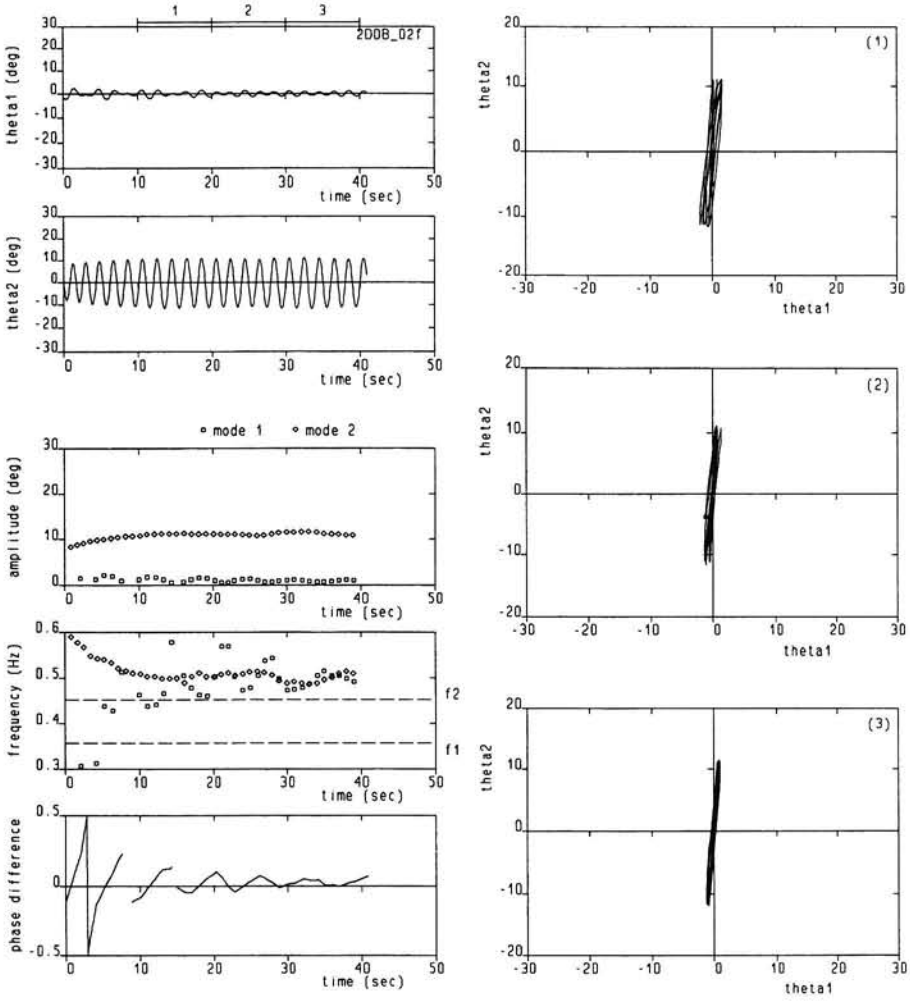
1
2
3
2D0B_02f
theta1 (deg)
theta2 (deg)
time (sec)
mode 1
mode 2
amplitude (deg)
frequency (Hz)
f2
f1
phase difference
theta2
theta1
(1)
(2)
(3)

Figure B2f.

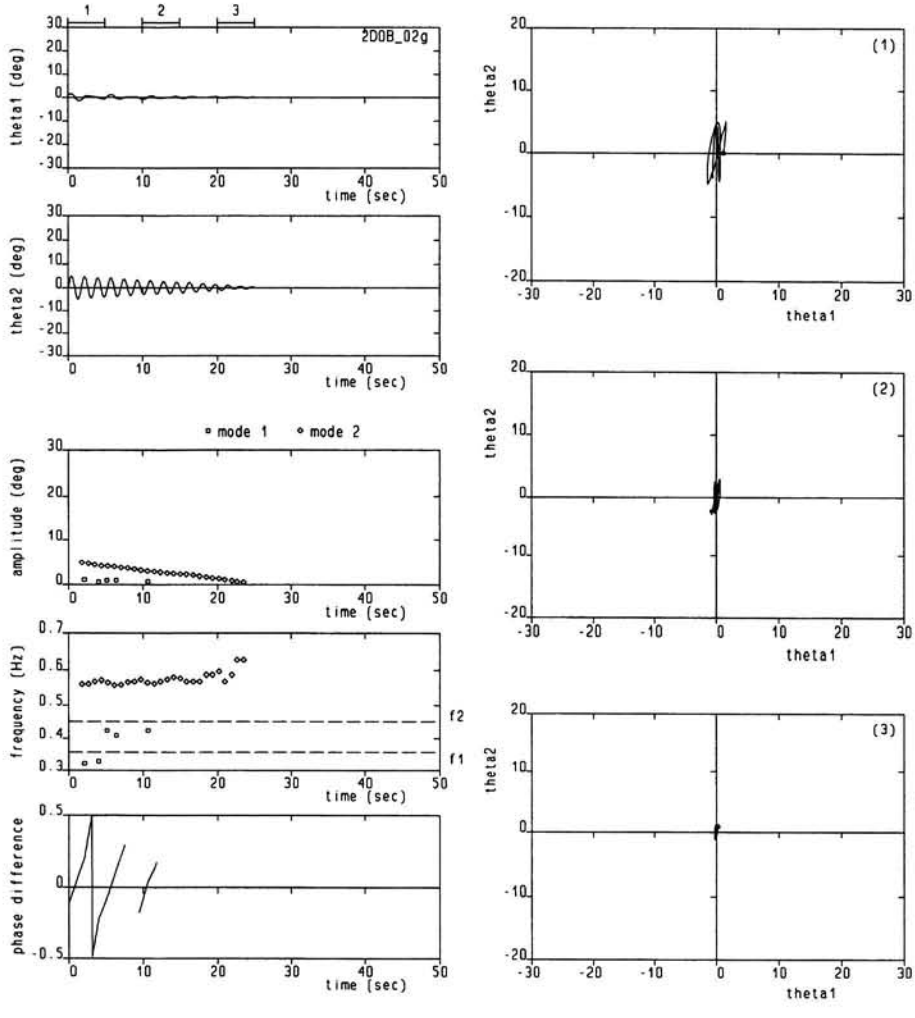
1
2
3
2D0B_02g
theta1 (deg)
theta2 (deg)
time (sec)
mode 1
mode 2
amplitude (deg)
frequency (Hz)
f2
f1
phase difference
theta2
theta1
(1)
(2)
(3)

Figure B2g.

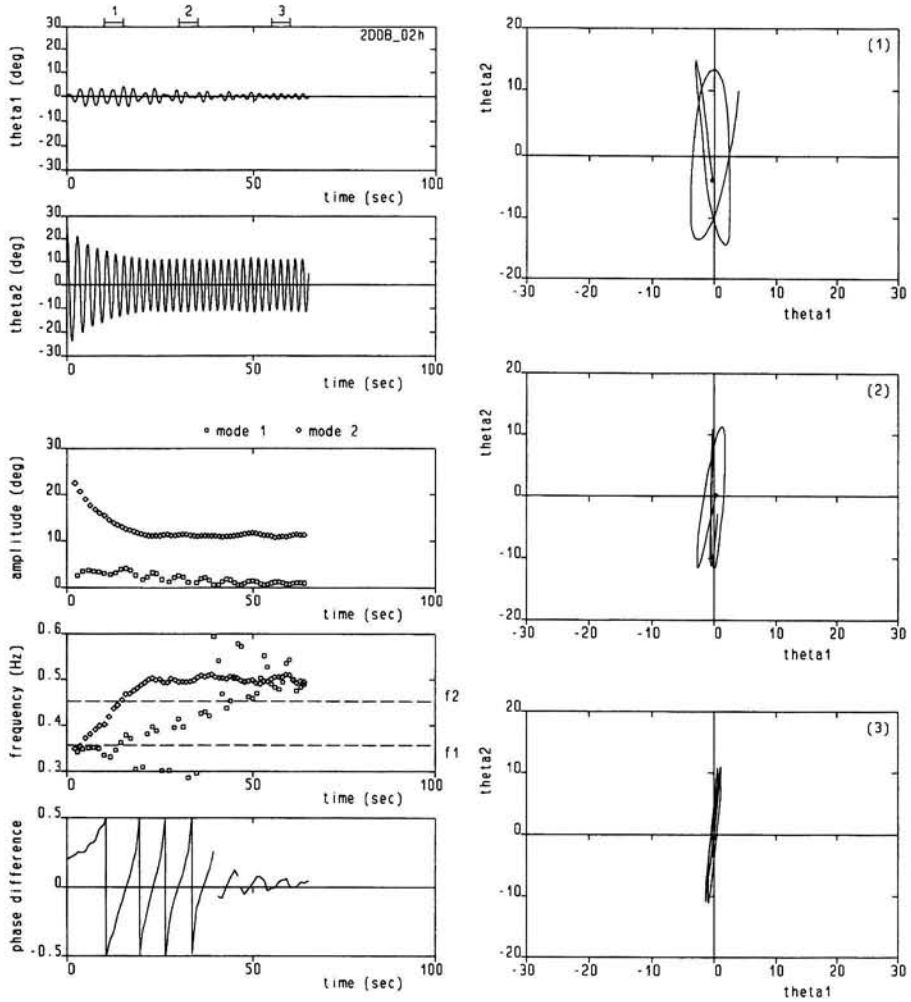
1
2
3
2D0B_02h
theta1 (deg)
time (sec)
theta2 (deg)
mode 1
mode 2
amplitude (deg)
frequency (Hz)
f2
f1
phase difference
theta2
theta1
(1)
(2)
(3)

Figure B2h.

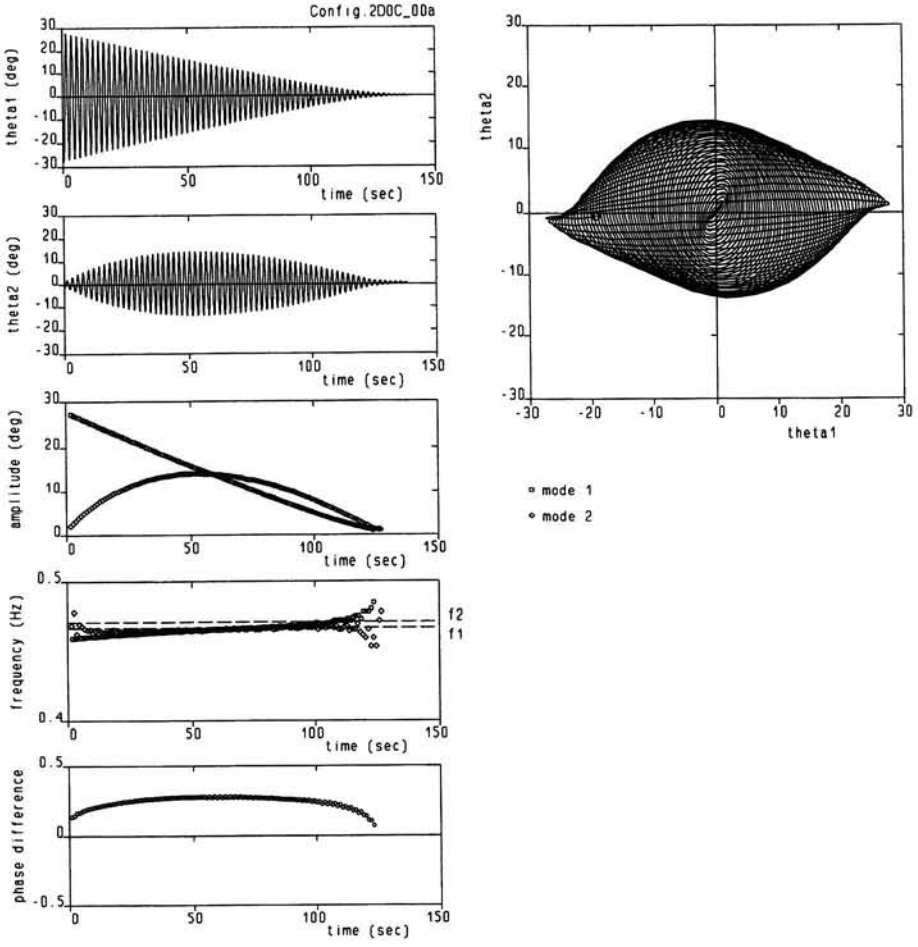
Config.2D0C_00a
theta1 (deg)
theta2 (deg)
amplitude (deg)
frequency (Hz)
phase difference
time (sec)
f2
f1
theta2
theta1
mode 1
mode 2

Figure C0a.

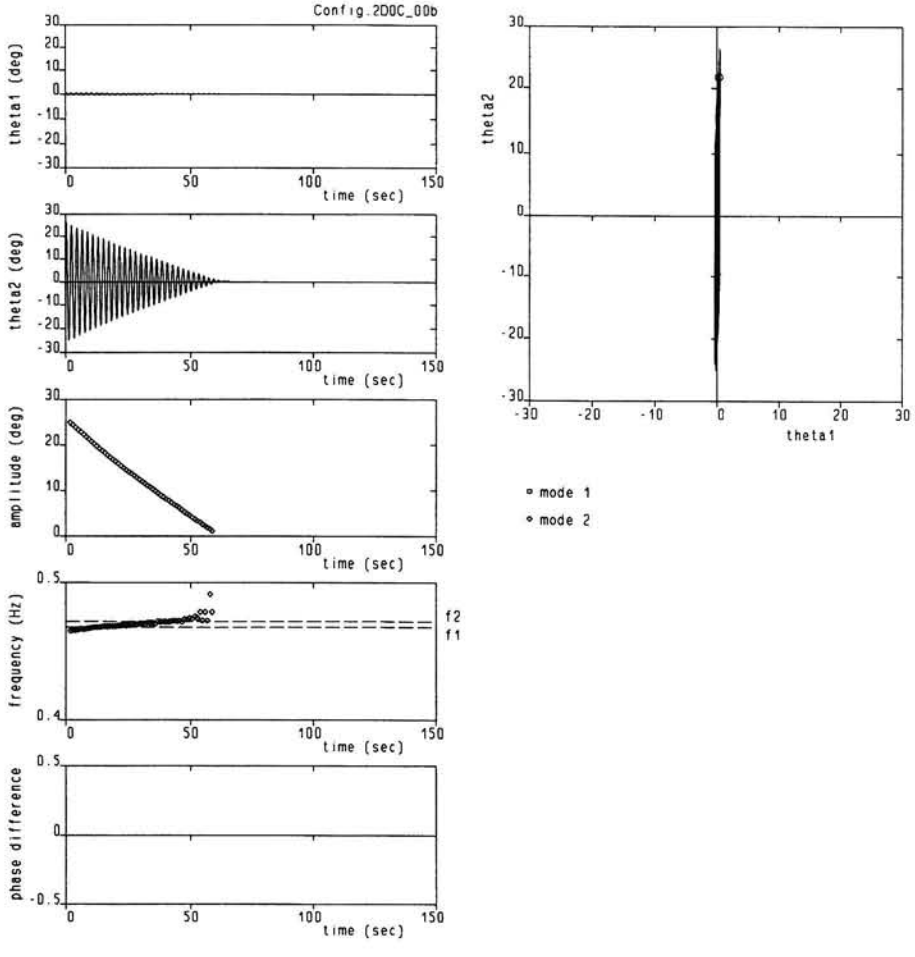
Config.2D0C_00b
theta1 (deg)
theta2 (deg)
amplitude (deg)
frequency (Hz)
phase difference
time (sec)
f2
f1
theta2
theta1
mode 1
mode 2

Figure C0b.

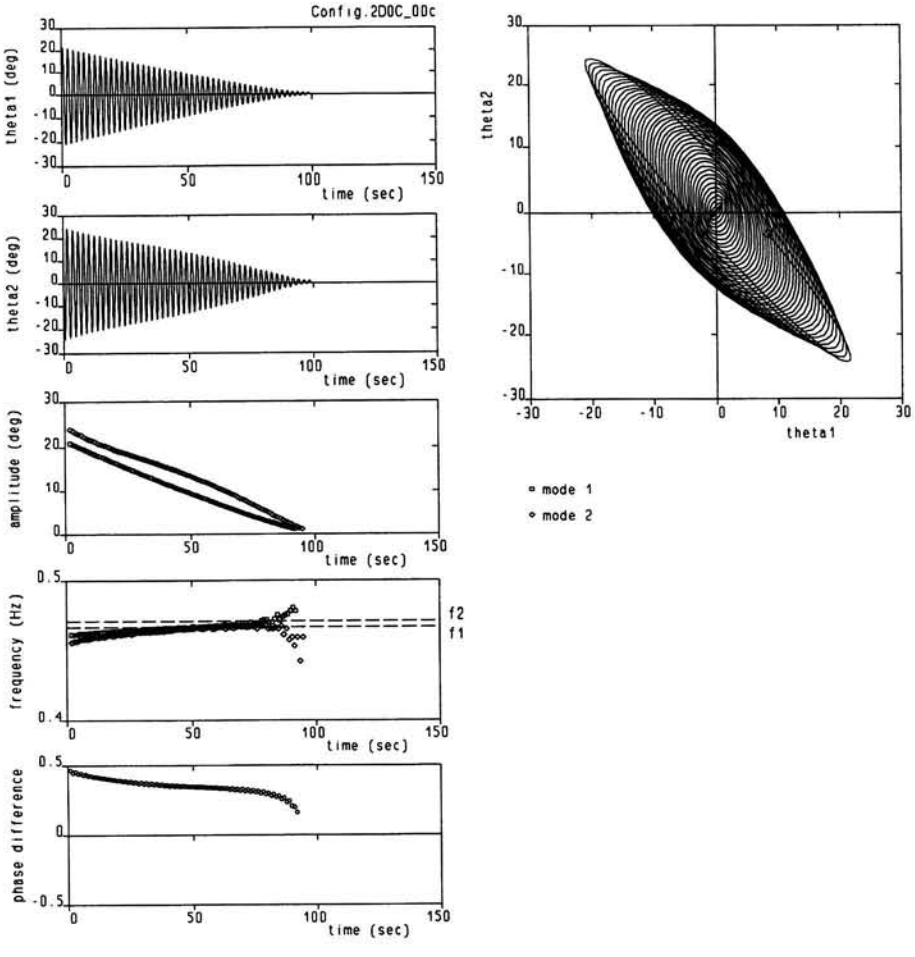
Config.2D0C_00c
theta1 (deg)
theta2 (deg)
amplitude (deg)
frequency (Hz)
phase difference
time (sec)
f2
f1
theta2
theta1
mode 1
mode 2

Figure C0c.

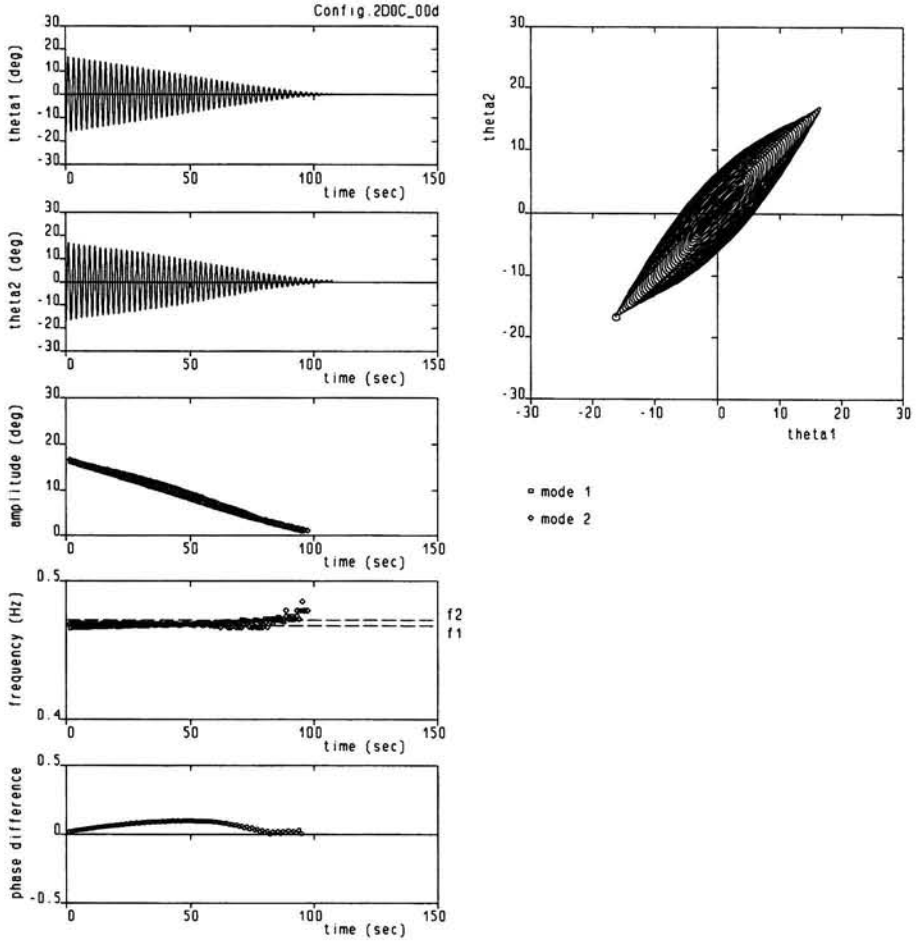
Config.2D0C_00d
theta1 (deg)
theta2 (deg)
amplitude (deg)
frequency (Hz)
phase difference
time (sec)
f2
f1
theta2
theta1
mode 1
mode 2

Figure C0d.

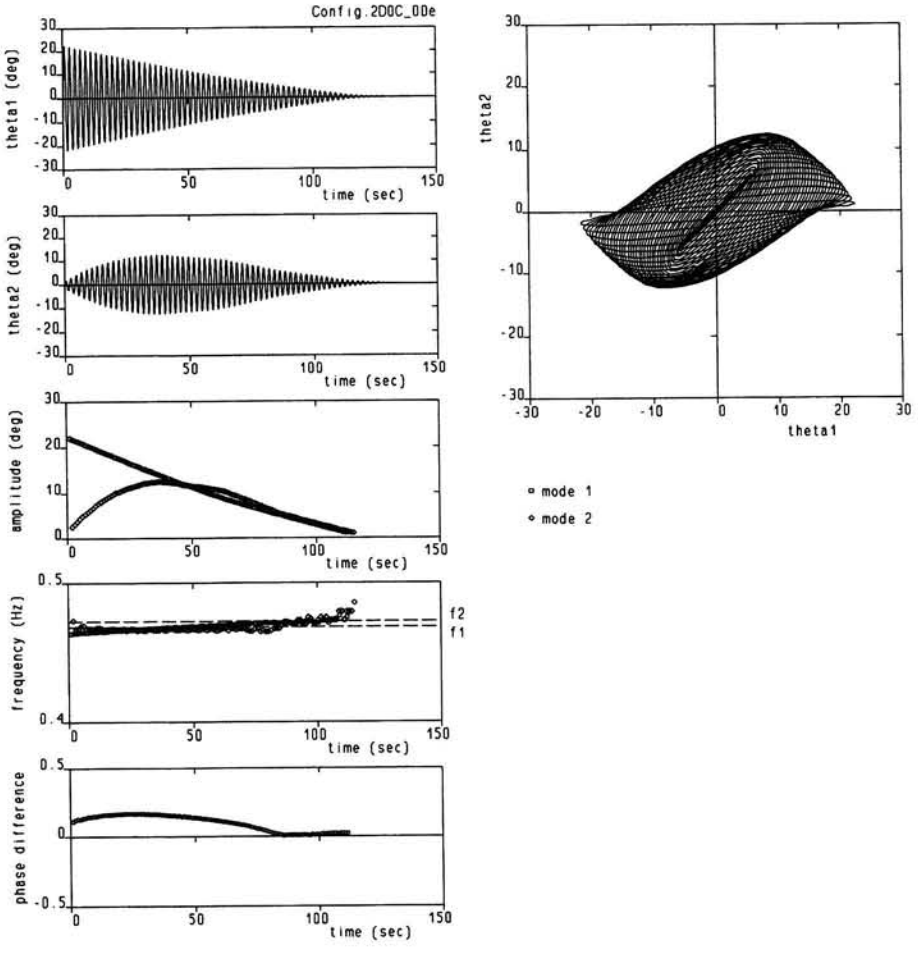
Config.2D0C_0De
theta1 (deg)
theta2 (deg)
amplitude (deg)
frequency (Hz)
phase difference
time (sec)
f2
f1
theta2
theta1
mode 1
mode 2

Figure C0e.

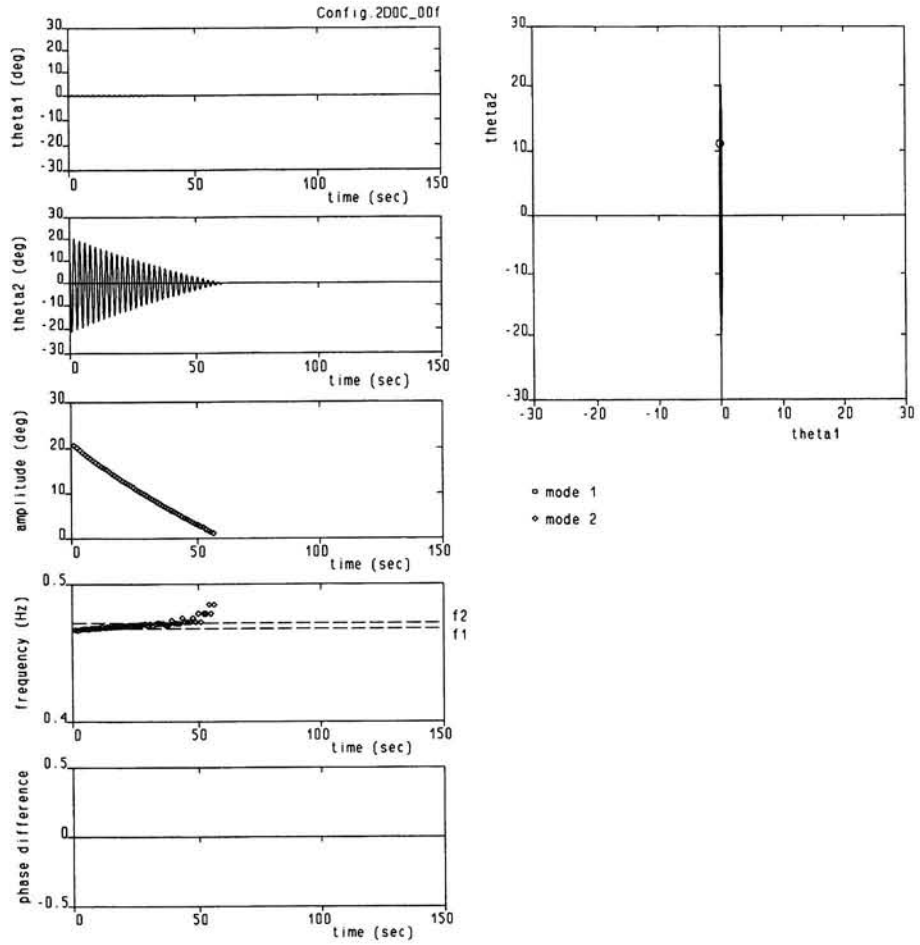
Config.2D0C_00f
theta1 (deg)
theta2 (deg)
amplitude (deg)
frequency (Hz)
phase difference
time (sec)
f2
f1
theta2
theta1
mode 1
mode 2

Figure C0f.

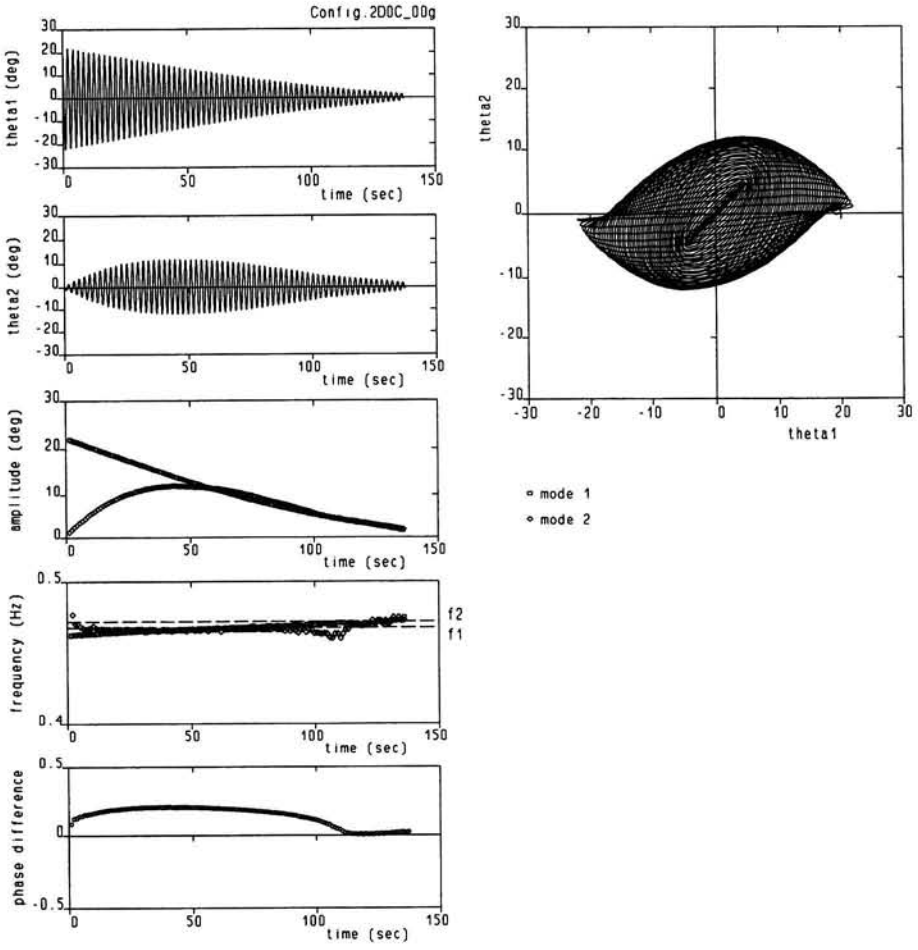
Config.2D0C_00g
theta1 (deg)
theta2 (deg)
amplitude (deg)
frequency (Hz)
phase difference
time (sec)
f2
f1
theta2
theta1
mode 1
mode 2

Figure C0g.

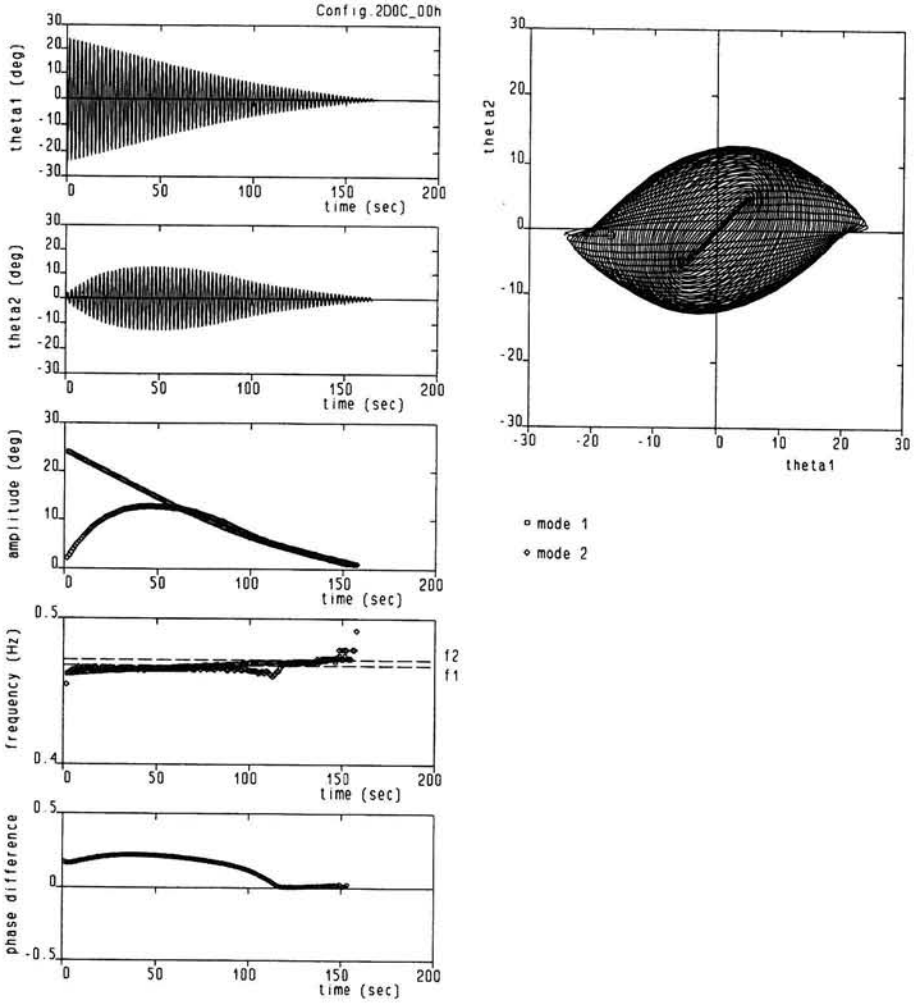
Config.2D0C_00h
theta1 (deg)
theta2 (deg)
amplitude (deg)
frequency (Hz)
phase difference
time (sec)
f2
f1
theta2
theta1
mode 1
mode 2

Figure C0h.

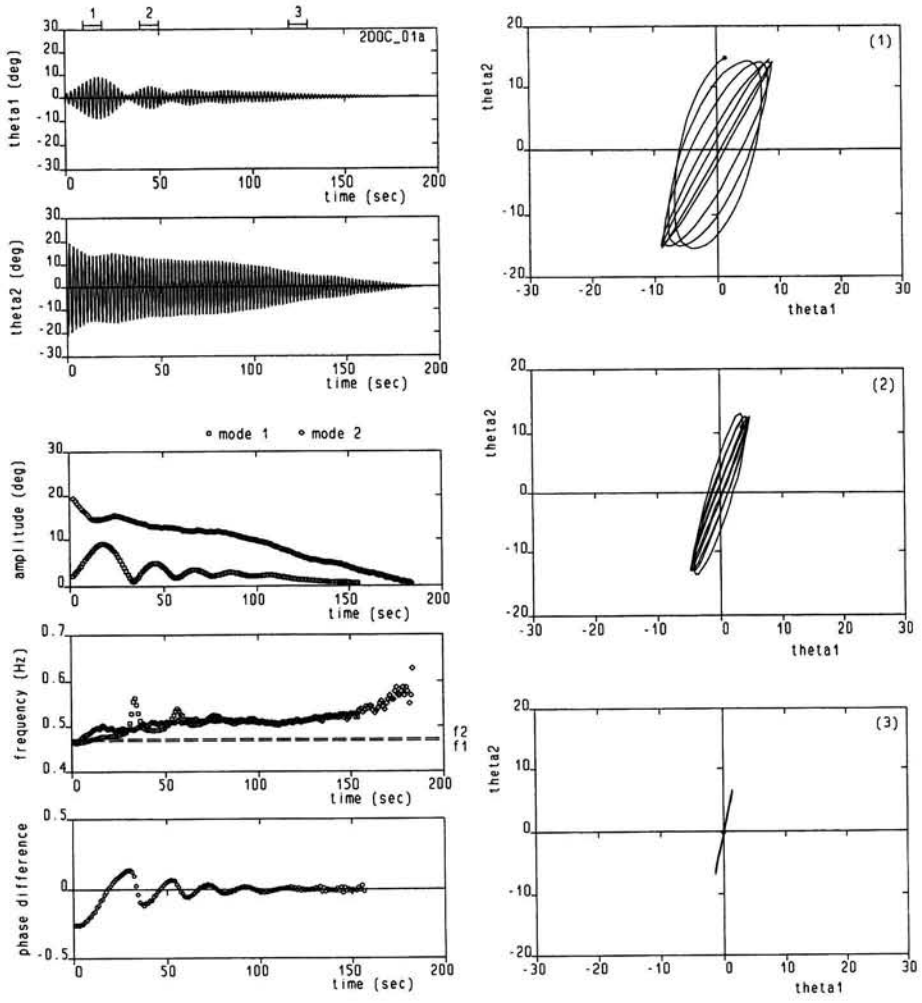
1
2
3
2D0C_01a
theta1 (deg)
theta2 (deg)
time (sec)
mode 1
mode 2
amplitude (deg)
frequency (Hz)
f2
f1
phase difference
theta2
theta1
(1)
(2)
(3)

Figure C1a.

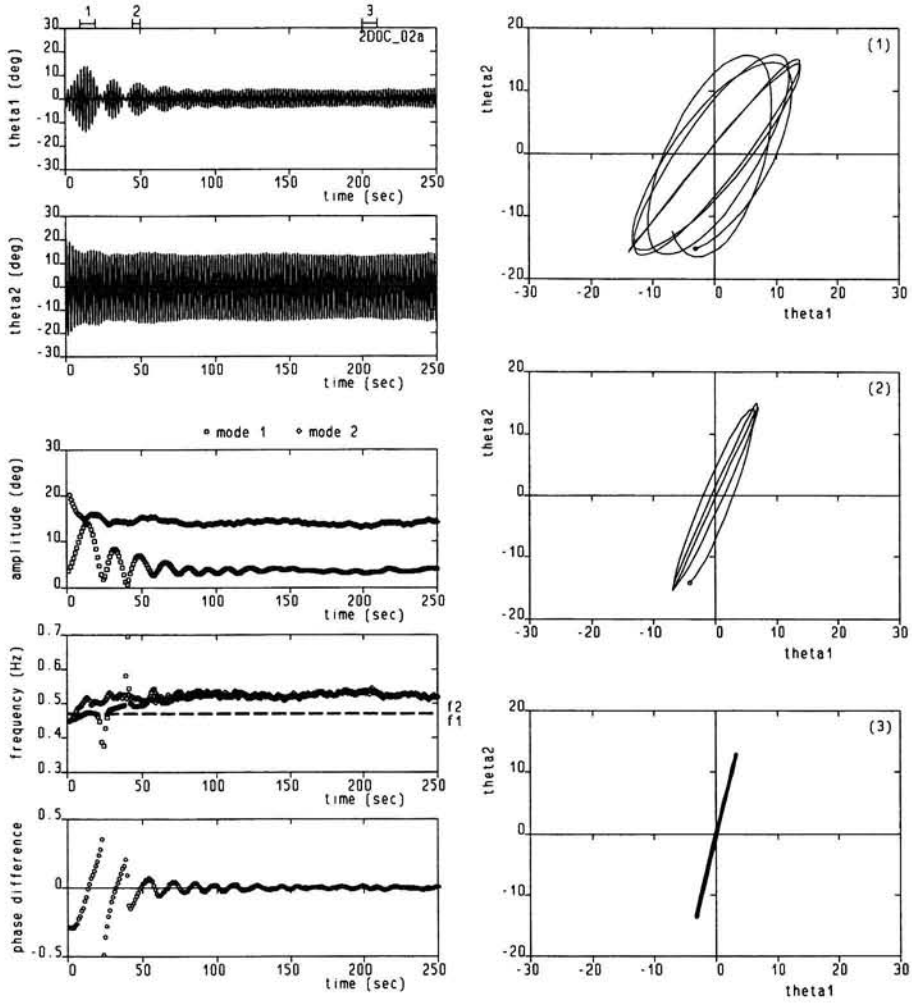
1
2
3
2D0C_02a
theta1 (deg)
theta2 (deg)
time (sec)
mode 1
mode 2
amplitude (deg)
frequency (Hz)
f2
f1
phase difference
theta2
theta1
(1)
(2)
(3)

Figure C2a.

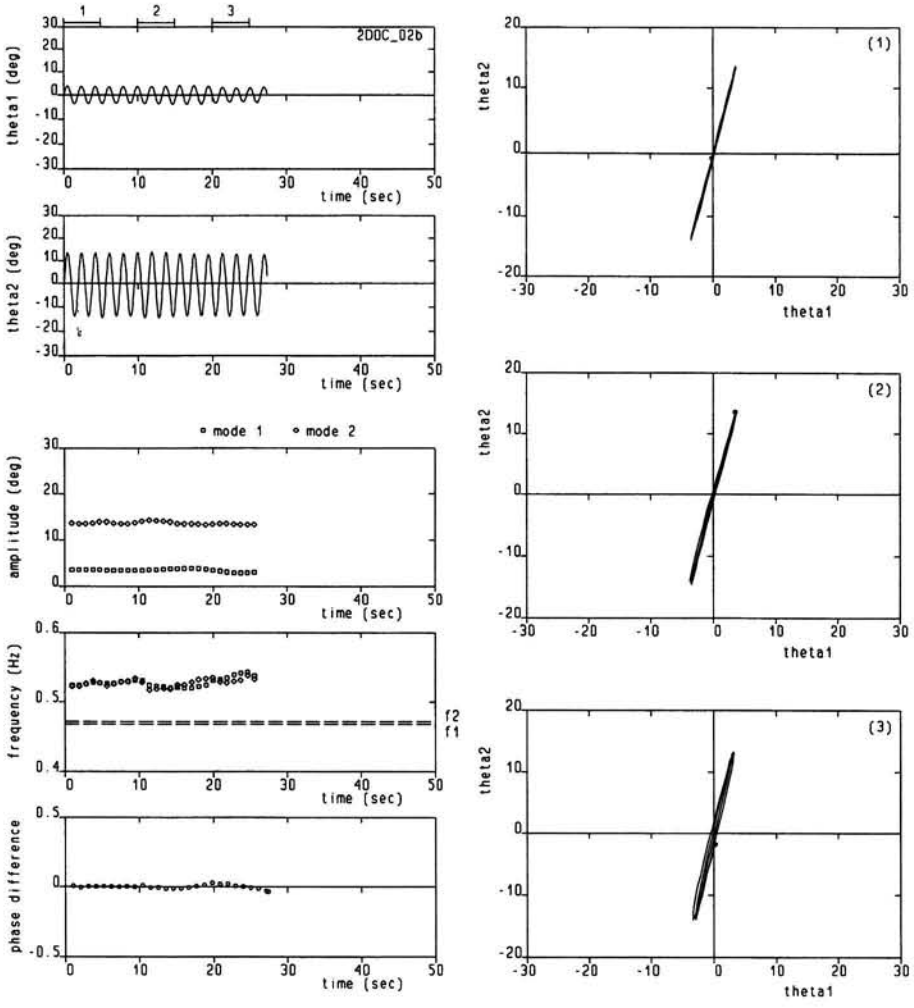
1
2
3
2DOC_02b
theta1 (deg)
time (sec)
theta2 (deg)
time (sec)
mode 1
mode 2
amplitude (deg)
time (sec)
frequency (Hz)
f2
f1
time (sec)
phase difference
time (sec)
(1)
theta2
theta1
(2)
theta2
theta1
(3)
theta2
theta1

Figure C2b.

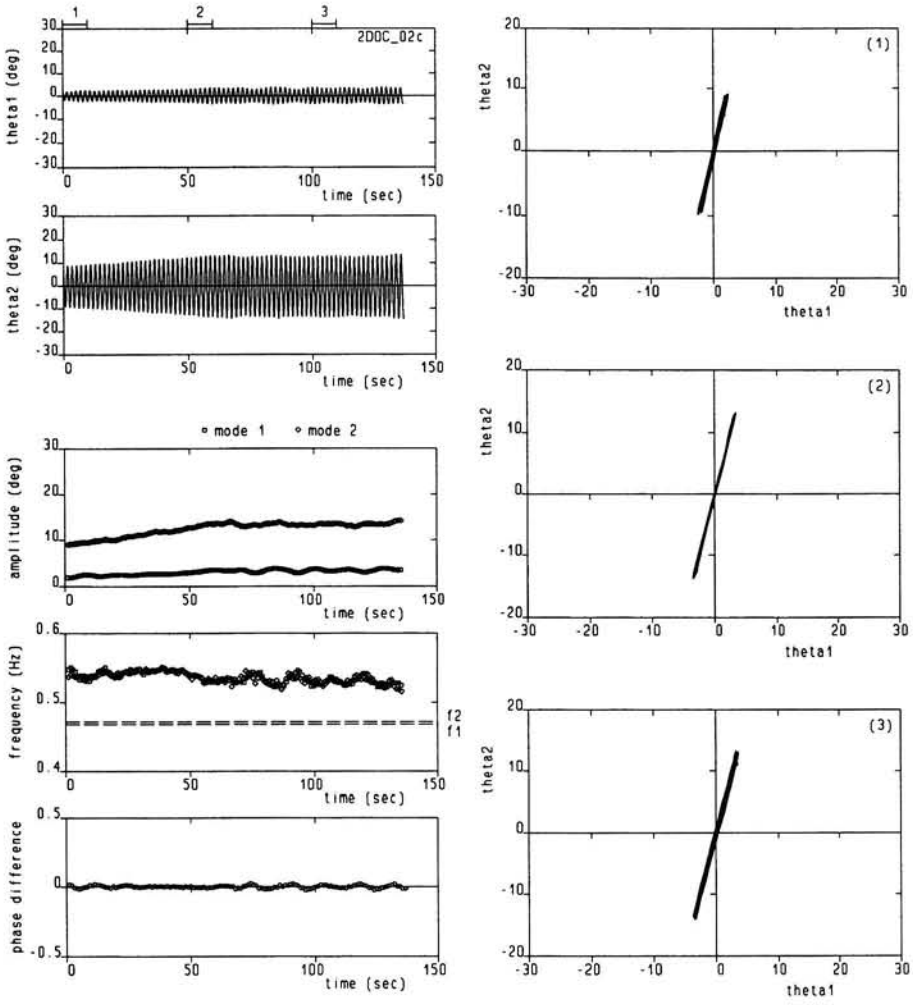
1
2
3
2D0C_02c
theta1 (deg)
time (sec)
theta2 (deg)
time (sec)
mode 1
mode 2
amplitude (deg)
time (sec)
frequency (Hz)
f2
f1
time (sec)
phase difference
time (sec)
theta2
theta1
(1)
theta2
theta1
(2)
theta2
theta1
(3)

Figure C2c.

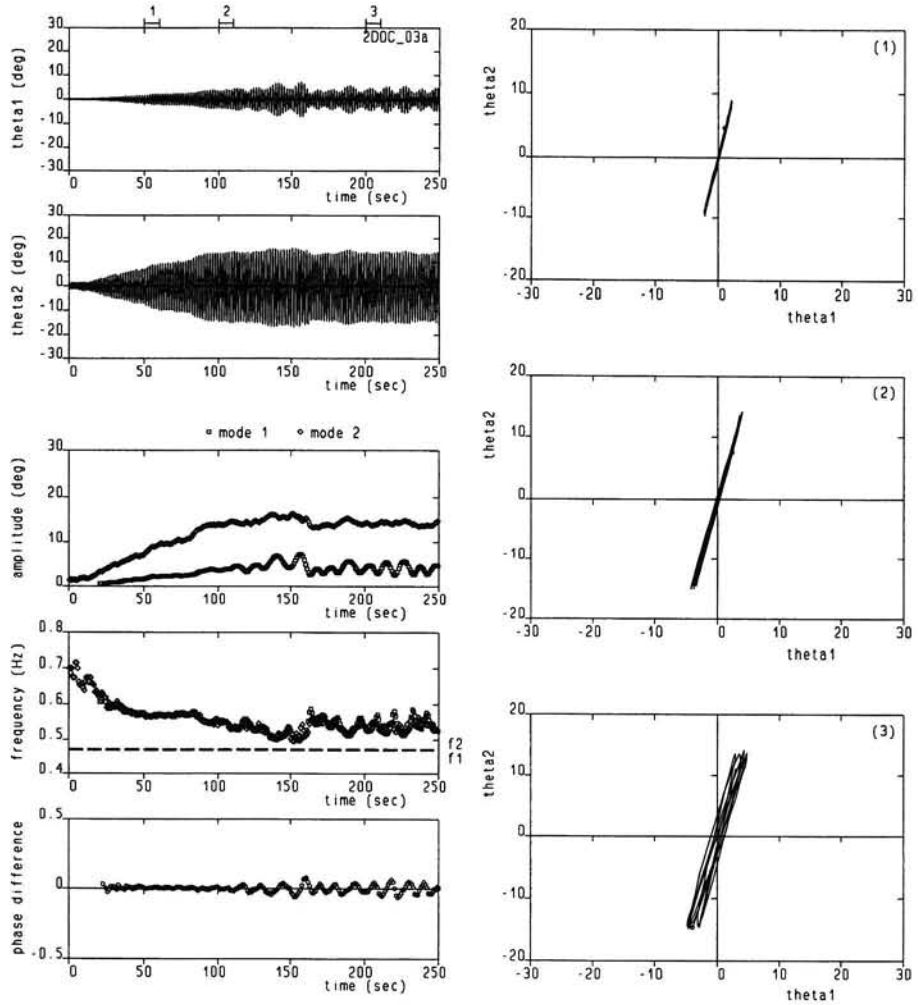
1
2
3
2DOC_03a
theta1 (deg)
theta2 (deg)
time (sec)
mode 1
mode 2
amplitude (deg)
frequency (Hz)
f2
f1
phase difference
theta2
theta1
(1)
(2)
(3)

Figure C3a.

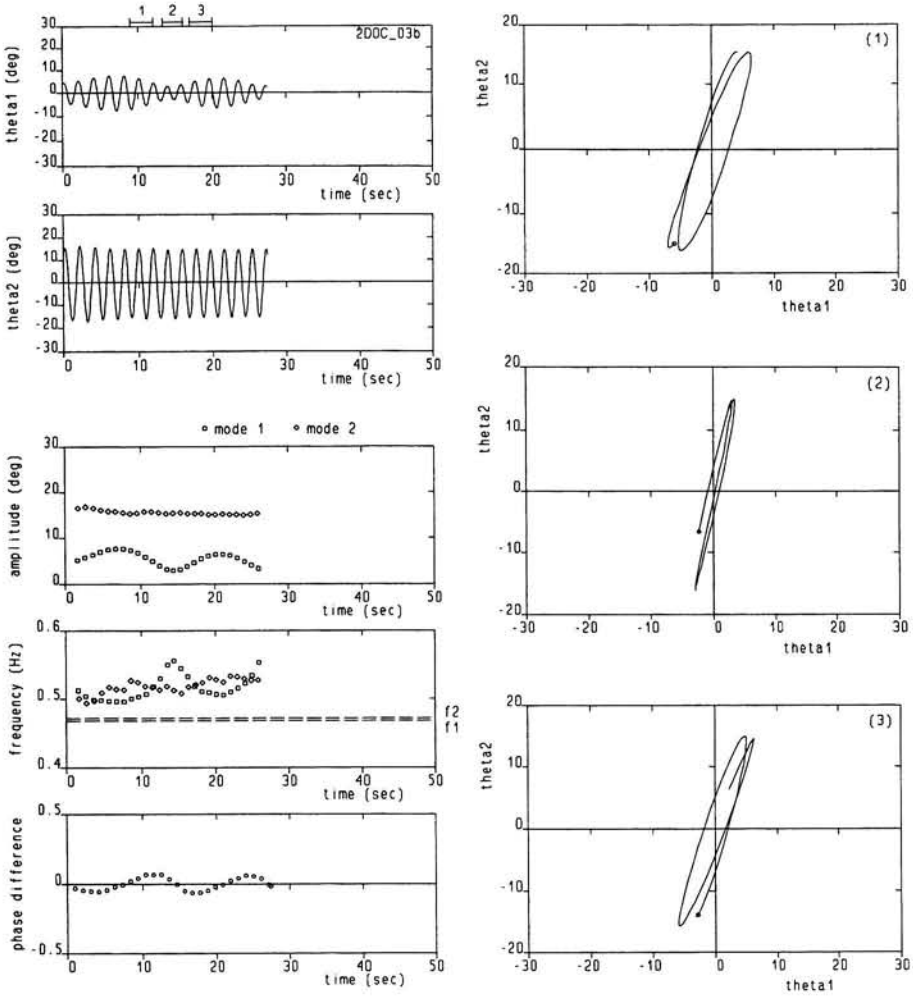
1 2 3
2DOC_03b
theta1 (deg)
theta2 (deg)
time (sec)
mode 1
mode 2
amplitude (deg)
frequency (Hz)
f2
f1
phase difference
theta2
theta1
(1)
(2)
(3)

Figure C3b.

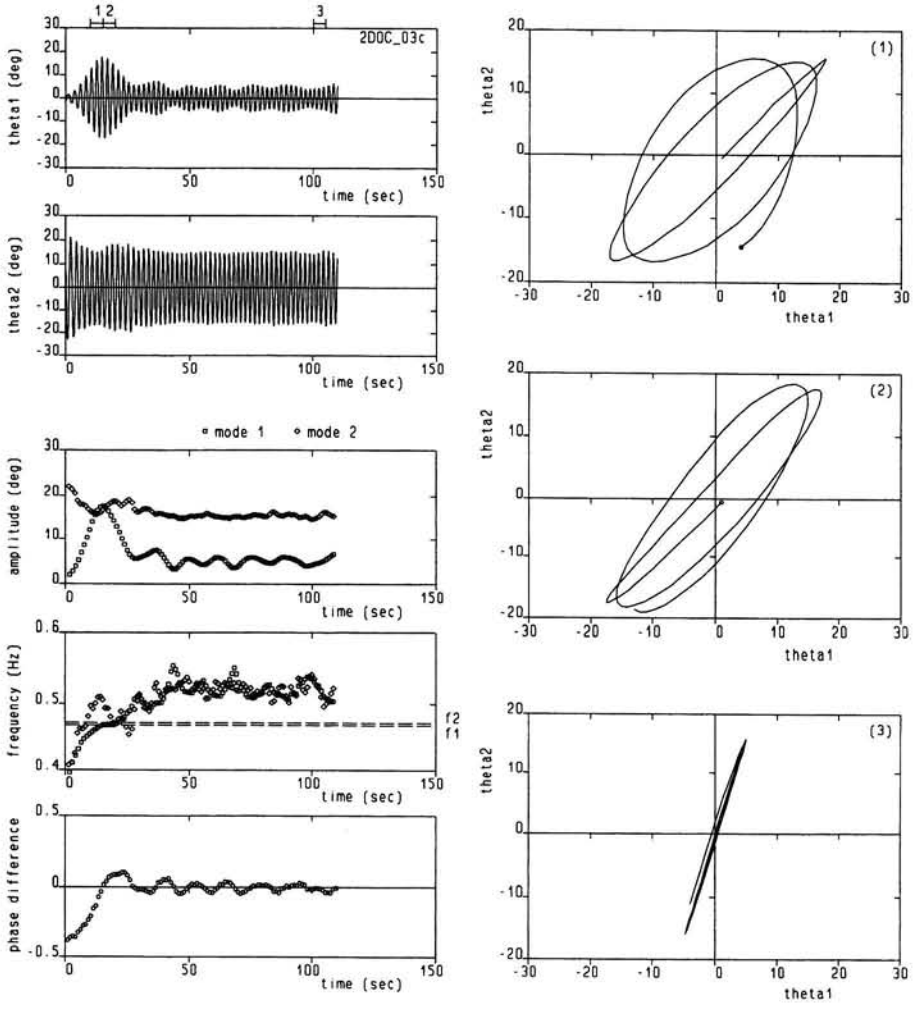
1 2
3
2D0C_03c
theta1 (deg)
theta2 (deg)
time (sec)
mode 1
mode 2
amplitude (deg)
frequency (Hz)
f2
f1
phase difference
theta2
theta1
(1)
(2)
(3)

Figure C3c.

Series 01: Aerodynamics

01. F. Motallebi, 'Prediction of Mean Flow Data for Adiabatic 2-D Compressible Turbulent Boundary Layers'
1997 / VI + 90 pages / ISBN 90-407-1564-5

02. P.E. Skåre, 'Flow Measurements for an Afterbody in a Vertical Wind Tunnel'
1997 / XIV + 98 pages / ISBN 90-407-1565-3

03. B.W. van Oudheusden, 'Investigation of Large-Amplitude 1-DOF Rotational Galloping'
1998 / IV + 100 pages / ISBN 90-407-1566-1

04. E.M. Houtman / W.J. Bannink / B.H. Timmerman, 'Experimental and Computational Study of a Blunt Cylinder-Flare Model in High Supersonic Flow'
1998 / VIII + 40 pages / ISBN 90-407-1567-X

05. G.J.D. Zondervan, 'A Review of Propeller Modelling Techniques Based on Euler Methods'
1998 / IV + 84 pages / ISBN 90-407-1568-8

06. M.J. Tummers / D.M. Passchier, 'Spectral Analysis of Individual Realization LDA Data'
1998 / VIII + 36 pages / ISBN 90-407-1569-6

07. P.J.J. Moeleker, 'Linear Temporal Stability Analysis'
1998 / VI + 74 pages / ISBN 90-407-1570-X

08. B.W. van Oudheusden, 'Galloping Behaviour of an Aeroelastic Oscillator with Two Degrees of Freedom'
1998 / IV + 128 pages / ISBN 90-407-1571-8

09. R. Mayer, 'Orientation on Quantitative IR-thermografy in Wall-shear Stress Measurements'
1998 / XII + 108 pages / ISBN 90-407-1572-6

10. K.J.A. Westin / R.A.W.M. Henkes, 'Prediction of Bypass Transition with Differential Reynolds Stress Models'
1998 / VI + 78 pages / ISBN 90-407-1573-4

11. J.L.M. Nijholt, 'Design of a Michelson Interferometer for Quantitative Refraction Index Profile Measurements'
1998 / 60 pages / ISBN 90-407-1574-2

12. R.A.W.M. Henkes / J.L. van Ingen, 'Overview of Stability and Transition in External Aerodynamics'
1998 / IV + 48 pages / ISBN 90-407-1575-0

13. R.A.W.M. Henkes, 'Overview of Turbulence Models for External Aerodynamics'
1998 / IV + 40 pages / ISBN 90-407-1576-9

Series 02: Flight Mechanics

01. E. Obert, 'A Method for the Determination of the Effect of Propeller Slipstream on a Static Longitudinal Stability and Control of Multi-engined Aircraft'
    1997 / IV + 276 pages / ISBN 90-407-1577-7
02. C. Bill / F. van Dalen / A. Rothwell, 'Aircraft Design and Analysis System (ADAS)'
    1997 / X + 222 pages / ISBN 90-407-1578-5
03. E. Torenbeek, 'Optimum Cruise Performance of Subsonic Transport Aircraft'
    1998 / X + 66 pages / ISBN 90-407-1579-3

Series 03: Control and Simulation

01. J.C. Gibson, 'The Definition, Understanding and Design of Aircraft Handling Qualities'
    1997 / X + 162 pages / ISBN 90-407-1580-7
02. E.A. Lomonova, 'A System Look at Electromechanical Actuation for Primary Flight Control'
    1997 / XIV + 110 pages / ISBN 90-407-1581-5
03. C.A.A.M. van der Linden, 'DASMAT-Delft University Aircraft Simulation Model and Analysis Tool. A Matlab/Simulink Environment for Flight Dynamics and Control Analysis'
    1998 / XII + 220 pages / ISBN 90-407-1582-3

Series 05: Aerospace Structures and Computional Mechanics

01. A.J. van Eekelen, 'Review and Selection of Methods for Structural Reliability Analysis'
    1997 / XIV + 50 pages / ISBN 90-407-1583-1
02. M.E. Heerschap, 'User's Manual for the Computer Program Cufus. Quick Design Procedure for a CUt-out in a FUSelage version 1.0'
    1997 / VIII + 144 pages / ISBN 90-407-1584-X
03. C. Wohlever, 'A Preliminary Evaluation of the B2000 Nonlinear Shell Element Q8N.SM'
    1998 / IV + 44 pages / ISBN 90-407-1585-8
04. L. Gunawan, 'Imperfections Measurements of a Perfect Shell with Specially Designed Equipment (UNIVIMP)
    1998 / VIII + 52 pages / ISBN 90-407-1586-6

Series 07: Aerospace Materials

01. A. Vašek / J. Schijve, 'Residual Strenght of Cracked 7075 T6 Al-alloy Sheets under High Loading Rates'
1997 / VI + 70 pages / ISBN 90-407-1587-4
02. I. Kunes, 'FEM Modelling of Elastoplastic Stress and Strain Field in Centre-cracked Plate'
1997 / IV + 32 pages / ISBN 90-407-1588-2
03. K. Verolme, 'The Initial Buckling Behavior of Flat and Curved Fiber Metal Laminate Panels'
1998 / VIII + 60 pages / ISBN 90-407-1589-0
04. P.W.C. Provó Kluit, 'A New Method of Impregnating PEI Sheets for the *In-Situ* Foaming of Sandwiches'
1998 / IV + 28 pages / ISBN 90-407-1590-4
05. A. Vlot / T. Soerjanto / I. Yeri / J.A. Schelling, 'Residual Thermal Stresses around Bonded Fibre Metal Laminate Repair Patches on an Aircraft Fuselage'
1998 / IV + 24 pages / ISBN 90-407-1591-2
06. A. Vlot, 'High Strain Rate Tests on Fibre Metal Laminates'
1998 / IV + 44 pages / ISBN 90-407-1592-0
07. S. Fawaz, 'Application of the Virtual Crack Closure Technique to Calculate Stress Intensity Factors for Through Cracks with an Oblique Elliptical Crack Front'
1998 / VIII + 56 pages / ISBN 90-407-1593-9
08. J. Schijve, 'Fatigue Specimens for Sheet and Plate Material'
1998 / VI + 18 pages / ISBN 90-407-1594-7

Series 08: Astrodynamics and Satellite Systems

01. E. Mooij, 'The Motion of a Vehicle in a Planetary Atmosphere'
1997 / XVI + 156 pages / ISBN 90-407-1595-5
02. G.A. Bartels, 'GPS-Antenna Phase Center Measurements Performed in an Anechoic Chamber'
1997 / X + 70 pages / ISBN 90-407-1596-3
03. E. Mooij, 'Linear Quadratic Regulator Design for an Unpowered, Winged Re-entry Vehicle'
1998 / X + 154 pages / ISBN 90-407-1597-1

3021860

The non-linear dynamic behaviour is considered of a mechanical oscillator with two degrees of freedom under the effect of aerodynamic forces. Free oscillation tests are used to determine the mechanical and damping properties of the construction. Dynamic tests were performed for different oscillator configurations and at different wind speeds. Especially the occurence of self-sustained oscillations were investigated. In contrast to the 1-DOF system studied earlier, the resulting dynamic behaviour is strongly complicated by the interaction of the two oscillation modes, in particular when the mode frequencies are of the same order. When attempting to construct an analytical model of the behaviour, the strong mode interaction suggests that the aerodynamic stiffness effects and a phase relation must be included to describe the observed behaviour.

ISBN 90-407-1571-8

DELFT AEROSPACE
ENGINEERING & TECHNOLOGY